博士論文

# Modern Monte Carlo approaches to classical spin systems: Irreversible algorithm and massive parallelization applied to chiral magnets

## (大規模モンテカルロシミュレーションによるカイラル磁性体の研究)

Yoshihiko Nishikawa
西川 宜彦

Department of Basic Science
Graduate School of Arts and Sciences
The University of Tokyo

東京大学大学院 総合文化研究科
広域科学専攻 相関基礎科学系

# 謝辞

はじめに指導教官である福島孝治教授に感謝いたします。修士課程から 5 年間に渡って多くの時間を議論に割いて下さり、直接研究に関する話題にとどまらない具体的なアドバイスをいくつも頂きました。この 5 年間の大学院生活を、これまでの人生で最も楽しく刺激的で充実したものにできたのは間違いなく福島さんのおかげだと考えています。そして何より、自由な議論と活発な情報交換を気軽に行うことのできる現在までの福島研の雰囲気を作り上げて下さったことに感謝申し上げます。

次に Manon Michel 博士と Werner Krauth 教授に感謝いたします。Manon Michel さんとは Part I でのアルゴリズム、Werner Krauth さんとは Part I アルゴリズムと Part III でのカイラル磁性体の相転移について共同研究を行いました。2016 年 3 月と 2017 年 7 月の二度の Ecole Normale Supérieure 訪問の際には直接議論して頂き、非常に刺激を受けました。また、ENS の他の学生とともに暖かく歓迎して下さり、日本とは違う生活スタイルを垣間見ることができたことも大きな刺激になりました。2017 年 1 月から 3 月まで Krauth さんが本郷に客員教授として滞在していた期間には週に何度も頻繁に議論することができ、福島研とは異なる研究の進め方を学ぶことができました。これらの体験によって、研究者としての決意が確実になったと考えています。

本博士論文は池田昌史准教授、尾関之康教授、加藤雄介教授、藤堂眞治准教授に審査をして頂きました。審査会の前にも研究内容を説明させて頂くためのお時間を取って下さり、さらに本博士論文の詳細まで多くのご批判やコメントを頂きました。特に加藤雄介教授には、本博士論文の研究に普段から興味を持って頂き、加藤研究室でのセミナーで発表する機会を下さるなど、大変お世話になりました。この場をお借りして深く御礼申し上げます。

この 5 年間の大学院生活において、福島研のメンバーの存在は非常に大きなものでした。特に、異なる研究対象を扱っているにも関わらず、常に興味を持って議論に付き合って下さった観山正道助教 [*1]、髙邉賢史助教[*2]、小松尚登博士に感謝いたします。観山さんには分子動力学法や粒子系など、それまで福島研であまり触れることのなかったことについて様々なことを教えて頂きました。髙邉さんとは同じ居室であったこともあり、スピングラスの話から政治や宗教、美術や音楽の話まで、非常に幅広い話題について日常的にお話しする機会がありました。雑談が好きな僕に長い時間お付き合い下さったばかりでなく、幅広い教養を教えて下さったことに非常に感謝しております。

大学院で研究を行うにあたって、基礎科学科での講義やセミナーなどから長い付き合いのある越田真史くん、高橋惇くん、高橋昂くん、松本健太郎くん、水野広介くん、水野雄太くんからは大きな刺激を受けました。基礎科学科での同期がこのメンバーでなければ、強い意志を持って博士課程まで進むことはなかったかもしれません。特に高橋惇くんは同じ福島研で 5 年間のうち最も長い時間を過ごした友人であり、当初知り合った時には考えもしなかったほど長い付き合いになりました。彼の物理だけに留まらない科学に対する深い知識と情熱は常に僕にとって衝撃であり、影響を受けてきました。彼の記憶に残り続けられるよう、今後もより一層努力する所存です。

福島研以外で最も深い付き合いのあった加藤研のみなさま、特に福井毅勇くん、星野晋太郎助教[*3]、正木祐輔さんには研究上の話から普段の会話まで大変お世話になりました。正木さん

[*1] 現東北大学
[*2] 現名古屋工業大学
[*3] 現埼玉大学

には博士課程の最後の 2 年間で様々な議論にお付き合い頂き、多くのことを教えて頂きました。また、星野さんには Part I のアルゴリズムの研究の当初から興味を持って頂き、そこから発展して異なる分野の面白さなど様々なことを教えていただきました。本博士論文の研究は少なからず星野さんに影響を受けています。また数多くの相談に乗って頂き、星野さんの人柄に助けられることも多々ありました。深く感謝いたします。

日本物理学会や国際会議など様々な場所でお世話になりました大関真之准教授、小渕智之助教、尾澤岬博士、池田晴國博士、白石直人博士に感謝いたします。特に池田さんには 2017 年 7 月にパリに滞在した際にガラスについての議論に付き合って頂いたほか、食事や休日に日帰り旅行に連れて行って頂くなど大変お世話になりました。

昨年度まで福島研の秘書を務められていた豊田久子さんと現在の秘書である長谷眞紀子さんには様々なことでお世話になりました。特に最後の一年間同じ居室であった長谷さんとは普段からたくさんお話しする機会がありました。長谷さんとの会話は博士課程最後の年の大きな楽しみであり、居室に来る大きなモチベーションになっていました。

本博士論文中の研究の着想は、駒場という環境だからこそ得られたものだと考えています。普段から福島研だけでなく加藤雄介教授や他の加藤研のメンバーと頻繁に話す機会があったからこそ、これらの研究を行うことができました。今後も駒場という場所を生かして、研究室間の盛んな交流や研究、研究成果の活発な発表が行われることを強く願っております。

最後に、博士課程を終えるまでの極めて長い時間、不安に思いながらも暖かく見守ってくれた両親に感謝します。博士課程という、誰もが受けられるわけではない高等教育を受けることができたのも、それを通して数多くの貴重な体験ができたのも両親のおかげです。ありがとうございました。

# 1 General Introduction

Since the two seminal papers, the first Markov chain Monte Carlo simulation by N. Metropolis and collaborators [1], and the first molecular dynamics simulation by B. Alder and T. E. Wainwright [2], numerical simulations have increased their importance, and been extensively utilized to find new understandings of our nature. In particular, Markov chain Monte Carlo simulations, based on fundamental mathematical theories of Markov chains, have been rapidly progressed with many innovative algorithms. Thanks to their simplicity and applicability, we can easily simulate any systems using our computers. Indeed, many works in physics, chemistry, engineering, and statistics have used Monte Carlo simulations. Monte Carlo simulation is now an essential tool in various fields of science along with theory and experiment.

To understand physics is closely related to simulation. We can imagine, or simulate in our mind, how a simple object moves in a simple situation according to the Newtonian dynamics, and thus predict its behavior. However, only with three objects interacting with each other, an extremely complex, chaotic behavior may be observed, and we cannot imagine their moves precisely. When extremely many objects move simultaneously with interactions, we no longer know how to imagine their dynamics. We cannot simulate in our mind a system with an extremely large number of objects and predict what will happen correctly without any a priori knowledge although to understand and to predict collective behaviors are fundamental and important problems. Phase transition is a typical example where many-body effects are essentially relevant. Numerical simulations of many objects are expected to extend our mind, and extend the possibility of our understandings of collective phenomena and phase transitions.

Phase transitions have been one of the major research subjects in physics for many years. Since the celebrated work by L. Onsager [3], in which an exact solution for the two-dimensional ferromagnetic Ising model is presented, many statistical models and their phase transitions have been solved exactly. Unfortunately, a very specific class of models is solvable while an infinite number of exactly solvable models can be constructed. Another analytical theory, the mean-field theory, may provide us a qualitative understanding of a phase transition. The mean-field theory usually explains a phase transition exactly in infinite dimensions. That helps us to know what physical quantities are involved in a phase transition even in finite dimensions. Nevertheless, the mean-field theory often contains uncontrolled approximations, and can be completely wrong in finite dimensions; the theory sometimes predicts a phase transition which does not exist actually, or a qualitatively different phase transition. Indeed, the Ginzburg criterion is often violated in the mean-field theory when the spatial dimension is lower than the upper critical dimension (which is usually 4 in systems without disorder). Renormalization group and scaling theory, developed by K. Wilson and L. P. Kadanoff, are considered as promising theories to understand phase transitions in finite dimensions beyond mean-field theory.

These theories developed the concept of the universality for continuous phase transitions of systems. The universality classes are characterized by the critical exponents, which allow us to understand them in terms of the spatial dimensionality and symmetry of the systems. We thus simply estimate by its spatial dimensionality and symmetry the universality class to which a phase transition in a system belongs. However, when a system has very low symmetry due to competition or frustration among interactions and fields, symmetry of the system is no longer useful for understanding its universality class. The nature of a possible phase transition in that case depends on each system, and there may be an unexpected type of phase transition.

Chiral magnets, which will be extensively studied in this thesis, have very low symmetry, especially in the presence of a magnetic field. That induces various complicated spin structures into the magnetic systems at low temperature. Many spins behave collectively as if they form interacting objects with a length scale larger than the lattice spacing, and ordering in chiral magnets are driven by the objects. While chiral magnets have been greatly investigated both experimentally and theoretically in the literature of condensed-matter physics, detail properties of their phase transitions at finite temperature have been poorly understood. In the present thesis, by means of large-scale numerical simulations, I consider two models of chiral magnets from a point of view which has not been noticed ever for the models.

Numerical simulation is the method which in principle enables us to study any statistical models without any approximation. We can access any physical quantities and any correlations through numerical simulations. However, as other methods, numerical simulations also have disadvantages; finiteness of the system size and the simulation time. If the system size is not sufficiently large, we may misunderstand physical properties of systems in the thermodynamic limit, especially near their phase transition points. A short simulation time also leads us to wrong results. Only if we resolve these serious problems, we obtain correct results from numerical simulations. I will show in this thesis that modern Monte Carlo approaches, an irreversible algorithm, and massively parallelized simulations implemented on GPUs, can indeed resolve the problems, and allows us to get new physical insights.

This thesis is composed of three parts. In Part I, we discuss the Markov-chain Monte Carlo method. We introduce the concept of Markov chains, their fundamental properties, and three time scales in Markov chains in the first chapter. Next, various Markov chain Monte Carlo algorithms are discussed focusing on their pros and cons. In Chapter 3, we consider the recently introduced event-chain Monte Carlo algorithm. We apply the event-chain algorithm to classical Heisenberg spin models such as the three-dimensional ferromagnetic model, the antiferromagnetic model on the triangular lattice, and the three-dimensional spin glass model, and discuss its performance in each model.

In Part II, we discuss a classical Heisenberg spin model of a uni-axial chiral magnet in three dimensions. Due to the Dzyaloshinskii–Moriya interaction, the model has a simple helical structure in the low temperature region without magnetic fields, and a non-trivial spin structure which is called the chiral soliton lattice in the presence of a magnetic field perpendicular to the helical axis. In the first chapter, we overview a theory of a one-dimensional continuum model at zero temperature. The continuum model shows a phase transition at finite field between the chiral soliton lattice and the paramagnetic phases. We also briefly review results of some experimental works using $Cr_{1/3}NbS_2$ on its phase diagram. In the next chapter, we detail the simulation method used in our Monte Carlo simulations. With the event-chain algorithm, we performed large-scale Monte Carlo simulations of the system with more than $10^6$ spins. In the last chapter, we present our results and discuss phase transition in the system. The universality class and the phase diagram are also discussed.

In Part III, melting transition of skyrmions which emerge in a two-dimensional chiral magnet is studied. Skyrmions are topological excitations with local energies, and locally-stable particle-like objects. They are also thermodynamically stable in chiral magnets because of the bi-axial Dzyaloshinskii–Moriya interaction. In the first chapter of the part, we review phase diagram of chiral magnets obtained by experiments. After that, we also review the famous Kosterlitz–Thouless–Halperin–Nelson–Young theory for two-dimensional melting of particles with/without a periodic substrate. In the next chapter, details of our Monte Carlo simulations are presented. In the last chapter, we present our Monte Carlo results and discuss phase diagram with an interpretation of skyrmions as point particles.

All of the original results presented in this PhD thesis are based on the following papers:

[4] Yoshihiko Nishikawa, Manon Michel, Werner Krauth, and Koji Hukushima,
Physical Review E **92**, 063306 (2015).
[5] Yoshihiko Nishikawa and Koji Hukushima,
Physical Review B **94**, 064428 (2016).
[6] Yoshihiko Nishikawa and Koji Hukushima
Journal of Physics: Conference Series **750**, 012014 (2016).
[7] Yoshihiko Nishikawa, Koji Hukushima, and Werner Krauth,
arXiv:1710.11095 (2017).

# Contents

# Part I

# Monte Carlo method in Statistical Mechanics

# 2

# Introduction to Markov chain Monte Carlo methods

Since the celebrated work by N. Metropolis and his collaborators [1], the Markov chain Monte Carlo method has been established as a standard tool in natural sciences. A rapid progress of modern computers in these decades allows us to access large-scale Monte Carlo simulations of systems with an extremely large number of degrees of freedom. Markov chains, the concept on which Monte Carlo simulations relies, are simple stochastic processes in which the transition probability depends on only the present state [*1]. Any Markov chain converges to its unique stationary probability distribution if the global balance, the irreducibility, and the aperiodicity conditions are satisfied. In this chapter, we introduce the concept of Markov chains, and discuss the conditions. We next discuss various Monte Carlo algorithms such as local, cluster, extended ensemble, and irreversible algorithms.

## 2.1 Markov chains

We overview the fundamental properties of Markov chains, especially those with discrete states and discrete time steps in this section. A Markov chain is specified by a state space, a transition probability matrix, and an initial distribution. By the Monte Carlo method using (pseudo-)random numbers, we can implement any Markov chain. We also discuss time scales and slowing down in Markov chains and Markov chain Monte Carlo simulations.

### 2.1.1 Markov chain and its convergence

In a Markov chain, a stochastic process with a random variable $\sigma$ on a set of discrete states $\Omega$ and a transition matrix $T$, the conditional probability that a state $\sigma_{t+1} = x_{t+1} \in \Omega$ appears at time $t+1$ depends on only the state $\sigma_t = x_t \in \Omega$, i.e.

$$P\left(\sigma_{t+1} = y \mid \{\sigma_0 = x_0, \cdots, \sigma_t = x_t\}\right) = P\left(\sigma_{t+1} = y \mid \sigma_t = x_t\right) = T\left(x_t, y\right). \tag{2.1}$$

Note that the transition probability matrix $T$ is normalized: $\sum_y T\left(x, y\right) = 1$. If, for every pair of $x, y \in \Omega$, there exists a finite integer $n$ such that $T^n\left(x, y\right) > 0$, then the Markov chain is irreducible, which means that any state can be reached from an arbitrary initial state in finite time steps. When the irreducibility holds for a Markov chain, then the Markov chain has a unique stationary distribution $\pi$, which satisfies the global balance

[*1] Technically, any stochastic process in which a state at time $t$ depends on a finite number of the past states at time $t-1, \cdots, t-k$ $(k \geq 1)$ is a Markov chain in the sense that it can be mapped to a Markov chain with $k = 1$.

condition [8]

$$\pi = \pi T \Leftrightarrow \forall y \in \Omega,\ \pi(y) = \sum_x \pi(x) T(x, y). \tag{2.2}$$

Here, for the consistency with the definition of the transition matrix, the stationary distribution $\pi$ is represented as a row vector. The global balance condition Eq. (2.2) always holds if the detailed balance condition $\pi(x) T(x, y) = \pi(y) T(y, x)$ is satisfied. Of course, when a distribution satisfies the detailed balance condition with the transition matrix $T$, the distribution is the unique stationary distribution. A Markov chain satisfying the detailed balance condition is called reversible.

While any Markov chains with irreducibility have only one stationary distribution $\pi$, periodic Markov chains, which will be specified below, with an initial distribution inequivalent to $\pi$ do not converge to $\pi$ even in the long time limit. Thanks to irreducibility, every state $x \in \Omega$ appears more than twice within a sufficiently long finite time step. We define a set of time steps $S(x) = \{t \mid t \geq 1, T^t(x, x) > 0\}$, and its period $d_x$ as the greatest common divisor of elements of $S(x)$. The period of every state of an irreducible Markov chain corresponds to each other [8], and thus the period $d$ of the Markov chain is defined as $d = d_x$ of a state $x$. An aperiodic Markov chain has $d = 1$, and any other chain with $d > 1$ is called periodic. For any Markov chains with irreducibility and aperiodicity, the convergence theorem holds, which states as follows [8]: Two constants $\alpha \in (0, 1)$ and $C > 0$ exist which satisfy

$$\delta(t) = \max_{x \in \Omega} \left\| T^t(x, \cdot) - \pi \right\|_{\mathrm{TV}} < C\alpha^t. \tag{2.3}$$

Here, $\|\cdot, \cdot\|_{\mathrm{TV}}$ denotes the total variation distance between two probability distributions defined as

$$\|\mu - \nu\|_{\mathrm{TV}} = \max_{x \in \Omega} |\mu(x) - \nu(x)|, \tag{2.4}$$

and $T(x, \cdot)$ represents the $x$-th row of the matrix $T$. Therefore, Markov chains with irreducibility and aperiodicity converge to the stationary distribution starting from an arbitrary initial distribution. Any Markov chain with a non-zero $T(x, x)$, which is the rejection rate, is always aperiodic, and thus any initial distribution converges to the stationary distribution in such a Markov chain. However, a rejection-free Markov chain can be periodic unless $S(x)$ has co-prime two elements.

In practice, our goal is to design a transition probability matrix that is irreducible and aperiodic so that its unique stationary distribution is of our interest, rather than to find the stationary distribution for a given transition matrix. The detailed balance condition has been traditionally adopted in designing, but the condition is sufficient for the convergence as discussed above. Indeed, some Markov chains and the corresponding Monte Carlo algorithms breaking detailed balance have been known. We will discuss a few of them in the end of this chapter, and in the next chapter.

### 2.1.2 Time scales and slowing down in Markov chains

While any Markov chains with irreducibility and aperiodicity converge exponentially to their stationary distribution, the convergence speed is not quite clear. To measure the speed of the convergence, we define the mixing time of a Markov chain as

$$\tau_{\mathrm{mix}}(\epsilon) = \min\{t \mid \delta(t) < \epsilon\}. \tag{2.5}$$

Direct computation of the mixing time is a computationally time-consuming task as the full information of the transition probability matrix is required. We can instead find other

time scales in reversible, irreducible, and aperiodic Markov chains that bounds the mixing time. In a reversible Markov chain, the transition matrix is symmetric, and it thus has real-valued eigenvectors and eigenvalues. Of course, thanks to the Perron–Frobenius theorem, the largest eigenvalue $\lambda_1 = 1$ (see Eq. (2.2)). The other eigenvalues $\{\lambda_i\}$ $(i = 2, \cdots |\Omega|)$ have $|\lambda_i| < 1$. The relaxation time of the Markov chain is defined as

$$\tau_{\mathrm{rel}} = \frac{1}{1 - \max_{i=2,\cdots|\Omega|} |\lambda_i|}. \tag{2.6}$$

The relaxation time gives upper and lower bounds of the mixing time if the Markov chain is irreducible and aperiodic [8]:

$$(\tau_{\mathrm{rel}} - 1) \log\left(\frac{1}{2\epsilon}\right) \leq \tau_{\mathrm{mix}}(\epsilon) \leq \log\left(\frac{1}{\epsilon \pi_{\mathrm{min}}}\right) \tau_{\mathrm{rel}}, \tag{2.7}$$

where $\pi_{\mathrm{min}} = \min_{x \in \Omega} \pi(x)$. However, unfortunately, the relaxation time is still difficult to be computed because it requires eigenvalues of the transition matrix. We thus usually focus on the correlation time determined by the autocorrelation function in practical Markov chain Monte Carlo simulations [9]. The autocorrelation function of a function $\mathcal{O}$ on the state space $\Omega$ is defined as

$$C_{\mathcal{O}}(t) = \frac{\langle \mathcal{O}(\sigma_t)\, \mathcal{O}(\sigma_0) \rangle_\pi - \langle \mathcal{O}(\sigma_t) \rangle_\pi \langle \mathcal{O}(\sigma_0) \rangle_\pi}{\langle \mathcal{O}^2(\sigma_0) \rangle_\pi - \langle \mathcal{O}(\sigma_0) \rangle_\pi^2}, \tag{2.8}$$

where the bracket $\langle \cdots \rangle_\pi$ represents the average over the stationary distribution $\pi$, and $\sigma_t$ is a state at time $t$. We define the exponential correlation time of a function $\mathcal{O}$ as

$$\tau_{\mathrm{exp}}(\mathcal{O}) = \limsup_{t \to \infty} \frac{t}{-\log C_{\mathcal{O}}(t)} \tag{2.9}$$

and the exponential correlation time of the Markov chain is defined as $\tau_{\mathrm{exp}} = \sup_{\mathcal{O}} \tau_{\mathrm{exp},\mathcal{O}}$ to find the slowest mode in the autocorrelation function. The exponential correlation time can be represented in terms of the eigenvalues as $\tau_{\mathrm{exp}} = -1/\log \max_{i=2,\cdots|\Omega|} |\lambda_i|$ [10], and $\tau_{\mathrm{exp}} < \tau_{\mathrm{rel}}$ if $\max_{i=2,\cdots|\Omega|} |\lambda_i|$ is sufficiently close to 1. We compute in practical Monte Carlo simulations the exponential correlation time of a function $\mathcal{O}_*$ with an assumption that the function $\mathcal{O}_*$ has the slowest relaxation mode of the Markov chain in its autocorrelation function.

In statistical mechanics, these time scales in Markov chains are closely related to phase transitions and spatial orders in the stationary distribution, i.e. the Gibbs distribution. For example, in a reversible Markov chain that has the Gibbs distribution of a lattice spin system as its stationary distribution, it was proved that the system has a short-range spatial order if the mixing time is finite for any system size [11]. In particular, for the two-dimensional Ising model at the critical temperature, which has a diverging correlation length in the thermodynamic limit, the relaxation time diverges polynomially with the system size [12] [*2]. While no general proof is known, the correlation time has been numerically shown to diverge polynomially at a continuous phase transition point in various models [13–16] [*3]. An exponent that characterizes the polynomial divergence of the time scales accompanied with continuous phase transitions is called the dynamical critical exponent $z$. For some Markov chains, the dynamical critical exponent is proved to

[*2] A rigorous proof was given in Ref. [12] using a continuous-time Markov chain.

[*3] If $\max_{i=2,\cdots|\Omega|} |\lambda_i| \to 1$ in the thermodynamic limit, both of the relaxation time and the exponential correlation time diverge with the same speed.

have a lower bound determined by the Gibbs distribution [17–20]. Note that the dynamical critical exponent strongly depends on the transition matrix $T$ even if the stationary distribution is identical: Cluster algorithms, which will be discussed below, have a much smaller $z$ than that of conventional algorithms. Conversely, we can measure the efficiency of each algorithm through the dynamical critical exponent. At a first-order phase transition point, where two different states separated by large free-energy barriers appear with equal statistical weights, on the other hand, the time scales diverge exponentially with the system size due to the nucleation process [21]. We thus can infer the order of phase transitions from the diverging behavior of the time scales.

## 2.2 Local Monte Carlo algorithm

Local Monte Carlo algorithm is the most used, simplest and straightforward algorithm to implement a Markov chain. We can sample from any probability distribution in the long time limit by using them. However, as we discussed above, with the local algorithms, we will be always confronted by the slowing down near a phase transition point. Nevertheless, because of their local nature, we can easily implement the algorithms in a spatially parallelized way. Recent Monte Carlo studies with massive parallelization indeed use local algorithms [22–26]. Here, we introduce the Metropolis–Hastings and the heat-bath algorithms (or Glauber dynamics).

### 2.2.1 Metropolis–Hastings algorithm

The original Metropolis algorithm is the first Markov chain Monte Carlo algorithm proposed in Ref. [1]. Let us consider a configuration $\boldsymbol{\sigma} = \boldsymbol{x}$ and another configuration $\boldsymbol{x}'$ proposed according to a symmetric proposal matrix $Q$, where $\boldsymbol{\sigma}$ is random variables following the Markov chain. The acceptance probability matrix $P_{\mathrm{Met}}$ in the Metropolis algorithm is

$$P_{\mathrm{Met}}\left(\boldsymbol{x} \to \boldsymbol{x}'\right) = \min\left[1, \frac{\pi\left(\boldsymbol{x}'\right)}{\pi\left(\boldsymbol{x}\right)}\right], \tag{2.10}$$

where $\pi\left(\boldsymbol{\sigma}\right)$ is the stationary probability distribution of the Markov chain. The algorithm simply satisfies the detailed balance condition as

$$\begin{aligned}\pi\left(\boldsymbol{x}\right) Q\left(\boldsymbol{x}, \boldsymbol{x}'\right) P_{\mathrm{Met}}\left(\boldsymbol{x} \to \boldsymbol{x}'\right) &= Q\left(\boldsymbol{x}, \boldsymbol{x}'\right) \min\left[\pi\left(\boldsymbol{x}\right), \pi\left(\boldsymbol{x}'\right)\right] \\ &= \pi\left(\boldsymbol{x}'\right) Q\left(\boldsymbol{x}', \boldsymbol{x}\right) P_{\mathrm{Met}}\left(\boldsymbol{x}' \to \boldsymbol{x}\right).\end{aligned} \tag{2.11}$$

For the Gibbs distribution at inverse temperature $\beta$, $\pi\left(\boldsymbol{\sigma}\right) = \exp\left(-\beta E\left(\boldsymbol{\sigma}\right)\right)/Z\left(\beta\right)$, we obtain the acceptance probability

$$P_{\mathrm{Met}}\left(\boldsymbol{x} \to \boldsymbol{x}'\right) = \min\left[1, \exp\left(-\beta\left(E\left(\boldsymbol{x}'\right) - E\left(\boldsymbol{x}\right)\right)\right)\right], \tag{2.12}$$

where $Z\left(\beta\right)$ is the partition function and $E\left(\boldsymbol{x}\right)$ is the energy of the configuration $\boldsymbol{x}$. We should notice here that the partition function $Z\left(\beta\right)$ does not appear in the transition probability Eq. (2.12). That implies we can simulate a Markov chain and sample from the stationary probability distribution $\pi\left(\boldsymbol{x}\right)$ without any a priori knowledge about the system except the energy.

About two decades after the work by Metropolis and coworkers, W. K. Hastings gave a generalization of the Metropolis algorithm, the Metropolis–Hastings algorithm [27]. In this generalized algorithm, the proposal matrix $Q$ does not need to be symmetric. The

acceptance probability matrix $P_{\mathrm{MH}}$, instead, is modified as

$$P_{\mathrm{MH}}\left(\boldsymbol{x} \to \boldsymbol{x}'\right) = \min\left[1, \frac{\pi\left(\boldsymbol{x}'\right) Q\left(\boldsymbol{x}', \boldsymbol{x}\right)}{\pi\left(\boldsymbol{x}\right) Q\left(\boldsymbol{x}, \boldsymbol{x}'\right)}\right]. \tag{2.13}$$

The factor $Q\left(\boldsymbol{x}, \boldsymbol{x}'\right) = 0$ if and only if $Q\left(\boldsymbol{x}', \boldsymbol{x}\right) = 0$ for an arbitrary pair of configurations $\boldsymbol{x}$ and $\boldsymbol{x}'$. We can easily check the transition probability in the Metropolis–Hastings algorithm $Q\left(\boldsymbol{x}, \boldsymbol{x}\prime\right) P_{\mathrm{MH}}\left(\boldsymbol{x} \to \boldsymbol{x}'\right)$ satisfies detailed balance as Eq. (2.11).

While the Metropolis–Hastings algorithm is the simplest algorithm and can be applied to any probability distributions, correlation between samples in the Markov chain remains large for a very long time. We have to be careful about the correlation time of this algorithm and simulate the system for much longer than the correlation time, and otherwise we will be led to a wrong result.

### 2.2.2 Heat-bath algorithm

The Metropolis–Hastings algorithm chooses one configuration from a proposed new configuration and the present one at each time step. The heat-bath algorithm, or Glauber dynamics, on the other hand, chooses one configuration from multiple configurations independent of the present configuration with satisfying detailed balance [*4]. The probability to choose a configuration $\boldsymbol{\sigma}_x$ from a set of configurations $\{\boldsymbol{\sigma}_y\}$ is

$$P_{\mathrm{HB}}\left(\boldsymbol{\sigma}_x\right) = \frac{\pi\left(\boldsymbol{\sigma}_x\right)}{\sum_y \pi\left(\boldsymbol{\sigma}_y\right)}. \tag{2.14}$$

In practice, we usually pick randomly (or sequentially, or according to other procedure) a few variables to be updated, and choose the set composing of all possible configurations which are equivalent to the present configuration except the picked variables. We illustrate the single-site heat-bath algorithm for the Gibbs distribution at inverse temperature $\beta$ of a $q$-state Potts model defined by the Hamiltonian $H\left(\boldsymbol{\sigma}\right)$, where each spin $\sigma_i = 0, \cdots, q-1$. Suppose that we choose a site $k$ to be updated. The probability to choose a configuration with $\sigma_k = a$ and other spins fixed is

$$P_{\mathrm{HB}}\left(\sigma_k = a\right) = \frac{\exp\left(-\beta H\left(\{\cdots, \sigma_k = a, \cdots\}\right)\right)}{\sum_{b\in\{0,\cdots,q-1\}} \exp\left(-\beta H\left(\{\cdots, \sigma_k = b, \cdots\}\right)\right)}. \tag{2.15}$$

The heat-algorithm can be better than the Metropolis–Hastings algorithm in a sense of the rejection rate when the number of components of the set is large. In particular, for some continuous spin models with classical Heisenberg spins, the heat-bath algorithm is rejection-free while the Metropolis–Hastings algorithm for these models has a finite rejection probability. Let us consider a classical Heisenberg spin model defined by the Hamiltonian

$$H\left(\{\boldsymbol{S}_i\}\right) = -\sum_{\langle i,j\rangle} \boldsymbol{S}_i \cdot J_{ij} \boldsymbol{S}_j - \sum_i \boldsymbol{h}_i \cdot \boldsymbol{S}_i, \tag{2.16}$$

where $\boldsymbol{S}_i$ is a three-dimensional vector with fixed length $|\boldsymbol{S}_i| = 1$, the bracket $\langle\cdot,\cdot\rangle$ represents a pair of interacting spins, $J_{ij}$ is a $3 \times 3$ matrix, and $\boldsymbol{h}_i$ is a three-dimensional vector. For a randomly chosen spin $\boldsymbol{S}_k$ to be updated, the normalization constant of this

[*4] The heat-bath algorithm is often regarded as a special case of the Metropolis–Hastings algorithm. Here, nevertheless, we introduce the heat-bath algorithm as another algorithm for clarity.

system excluding the contributions from the other fixed spins is

$$Z_k(\beta) = \int d\boldsymbol{S}_k e^{-\beta \boldsymbol{H}_k \cdot \boldsymbol{S}_k} = \int d\phi d(\cos\theta)\, e^{-\beta H_k \cos\theta} = 2\pi \frac{2\sinh(\beta H_k)}{\beta H_k}, \tag{2.17}$$

where $\boldsymbol{H}_k = \sum_j J_{ij}\boldsymbol{S}_j + \boldsymbol{h}_k$ and $H_k = |\boldsymbol{H}_k|$. We can sample a new orientation $(\theta', \phi')$ of the spin from $P_{\mathrm{HB}}(\cos\theta, \phi)\, d(\cos\theta)\, d\phi$ via its cumulative probability distribution using the inversion sampling technique as

$$\int_0^{\phi'} d\phi \int_{-1}^{\cos\theta'} d(\cos\theta)\, P_{\mathrm{HB}}(\cos\theta, \phi) = \frac{\phi'}{2\pi} \frac{e^{\beta H_k \cos\theta'} - e^{-\beta H_k}}{2\sinh(\beta H_k)}. \tag{2.18}$$

The probability to sample the old orientation as a new orientation is 0 in this algorithm.

Note here that the single-site heat-bath algorithm can be interpreted as direct sampling of a randomly chosen single spin from a conditional probability distribution under a condition that all other spins are fixed.

## 2.3 Cluster algorithm

The simple local Monte Carlo algorithms allow us to sample from the exact stationary probability distribution in the long time limit. However, as discussed above, the correlation time gets much longer and diverges with the system size either polynomially or exponentially at a phase transition point depending on the order of the phase transition. This dramatic increase of the correlation time makes Monte Carlo results have a large systematic error: Probability distributions of physical quantities obtained by short-time simulations may have different structures from the equilibrium ones. To solve this problem, we have to simulate for a very longer time than the correlation time, or consider an efficient algorithm in which correlations decay rapidly. Cluster algorithms can realize the rapid decorrelation in some models, and show us that slowing down near phase transition points that is caused by physical nature of systems can be reduced by artificial Monte Carlo dynamics. In this section we review some cluster algorithms and discuss their limitations.

### 2.3.1 Swendsen–Wang and Wolff algorithm

The Swendsen–Wang algorithm is the first algorithm that qualitatively changes dynamics of some systems [28]. By introducing extra variables which is called bond variables, many spins are updated in a cooperative manner. Here, for concreteness, we consider the $q$-state ferromagnetic Potts model defined by the Hamiltonian

$$H = -J \sum_{\langle i,j \rangle} \left( \delta_{\sigma_i, \sigma_j} - 1 \right), \tag{2.19}$$

where the bracket $\langle \cdot, \cdot \rangle$ represents an interacting pair of spins, and the spin variable $\sigma_i \in \{0, \cdots, q-1\}$. A configuration $\{\sigma_i\}$ appears at inverse temperature $\beta$ with probability

$$P_\beta^{\mathrm{Potts}}(\{\sigma_i\}) = \frac{1}{Z^{\mathrm{Potts}}(\beta)} \exp\left( \beta J \sum_{\langle i,j \rangle} \left( \delta_{\sigma_i, \sigma_j} - 1 \right) \right) \tag{2.20}$$

$$= \frac{1}{Z^{\mathrm{Potts}}(\beta)} \prod_{\langle i,j \rangle} \left[ p + (1-p)\, \delta_{\sigma_i, \sigma_j} \right], \tag{2.21}$$

where $p = \exp(-\beta J)$. We introduce bond variables $\{n_{ij}\}$ ($n_{ij} = 0, 1$) to the system that do not interact with each other so that the joint probability that a configuration $(\{\sigma_i\}, \{n_{ij}\})$ appears is

$$P_\beta^{\text{joint}}(\{\sigma_i\}, \{n_{ij}\}) = \frac{1}{Z^{\text{joint}}(\beta)} \prod_{\langle i,j \rangle} \left[ p\delta_{n_{ij},0} + (1-p)\,\delta_{\sigma_i,\sigma_j}\delta_{n_{ij},1} \right]. \tag{2.22}$$

Note that the normalization constants (the partition functions) for two probability distributions $Z^{\text{Potts}}(\beta)$ and $Z^{\text{joint}}(\beta)$ are identical, and the marginal distribution of $\{\sigma_i\}$ with $P_\beta^{\text{joint}}(\{\sigma_i\}, \{n_{ij}\})$ is equal to $P_\beta^{\text{Potts}}(\{\sigma_i\})$. We can directly sample $\{n_{ij}\}$ for a given $\{\sigma_i\}$ by Eq. (2.22) as

$$n_i = \begin{cases} 0 & \text{with probability } p/\left(p + (1-p)\,\delta_{\sigma_i,\sigma_j}\right) \\ 1 & \text{with probability } (1-p)\,\delta_{\sigma_i,\sigma_j}/\left(p + (1-p)\,\delta_{\sigma_i,\sigma_j}\right). \end{cases} \tag{2.23}$$

Every region of spins connected with $n_{ij} = 1$ is called a "cluster". After a direct sampling of $\{n_{ij}\}$, $\delta_{\sigma_i,\sigma_j}$'s are determined directly; $\delta_{\sigma_i,\sigma_j} = 1$ with probability $1\,(= (1-p)/(1-p))$ if $n_{ij} = 1$, and $\delta_{\sigma_i,\sigma_j}$ is arbitrary if $n_{ij} = 0$. In the original Swendsen–Wang algorithm [28], after identifying every cluster, new values of spins are randomly equally selected for each cluster independent of the former spin value. The Swendsen–Wang algorithm is often referred to as the multiple-cluster algorithm as every cluster is updated in every step. The Wolff algorithm proposed by U. Wolff [29], also known as the single-cluster algorithm, on the other hand, changes the spin value to a different one only for a single cluster. Although the Wolff algorithm seems to be just a variant of the Swendsen–Wang algorithm, its performance is usually slightly better than that of the Swendsen–Wang algorithm, especially for three-dimensional models [30]. Wolff also gave a generalization of the cluster algorithm to $O(n)$ continuous spin models [29] in which spins are reflected with respect to a randomly chosen axis.

The Swendsen–Wang and the Wolff algorithms dramatically reduce the dynamical critical exponent of simple ferromagnetic spin models, such as Ising, Potts, $XY$, and Heisenberg models. The dynamical exponent for the algorithms is rigorously bounded by a ratio of the static critical exponents as $z \geq \alpha/\nu$ [19].

### 2.3.2 Geometric cluster algorithm

The Swendsen–Wang and the Wolff algorithms were built on the representation of the partition function Eq. (2.22) derived from the Fortuin–Kasteleyn (FK) random-cluster representation of spin models [31–33]. The point of the cluster algorithms is, by introducing the bond variables, to update spin variables to a symmetric state in terms of the Hamiltonian that has the same statistical probability without any rejection. In particular, from this point of view, the Wolff algorithm can be understood without an explicit FK representation as follows:

1. Choose a spin $\sigma_i$ randomly.
2. Change the value of the spin $\sigma_i$ to $R(\sigma_i)$, where $R$ is an operator that preserves the Hamiltonian.
3. Put $i$ to a cluster.
4. For every spin $\sigma_j$ interacting with $\sigma_i$ except spins already in the cluster, change its value to $R(\sigma_j)$ with probability $1 - \exp(-\beta\Delta E_{ij})$, where $\Delta E_{ij} = E_{ij}(R(\sigma_i), \sigma_j) - E_{ij}(R(\sigma_i), R(\sigma_j))$.
5. Iterate 3–4 until the cluster growth stops.

The algorithm satisfies detailed balance if $R$ is self-inverse, i.e. $R^2 = \mathrm{id}$. By generalizing this abstract cluster algorithm, we can construct various cluster algorithms not only for spin systems but also for particle and any other models.

In 1996, C. Dress and W. Krauth proposed a pivot cluster algorithm for hard sphere systems in which positions of hard spheres are reflected with respect to a pivot [34]. Their algorithm utilizes point symmetry of the system, and it clearly satisfies the detailed balance condition. This algorithm was successfully applied to a binary mixture of hard objects [35] and a poly-disperse glassy system [36] in two dimensions. A finite-temperature counterpart of this cluster algorithm was proposed by J. Liu and E. Luijten [15], and it can significantly reduce critical slowing down at the liquid–gas critical point of a Lennard-Jones system. We also could consider a cluster algorithm for particles, or an avalanche algorithm, that utilizes translational symmetry of the system [37]; positions of many particles are moved with the same finite displacement. However, this cluster update often does not satisfy the detailed balance condition and almost all updates are rejected in the large density or low temperature region. We will discuss this algorithm in Section 3.1.1 again.

### 2.3.3 Limitation of cluster algorithms

The Swendsen–Wang and the Wolff cluster algorithms have been the most efficient algorithms for some simple models. However, they are powerless for more complicated models with frustration including, for example, spin glass models, and no speed up is seen in the dynamics for the models. A possible reason that the cluster algorithms cannot enhance decorrelation is the ratio of the cluster compared to the system size: The size of the clusters reaches to the system size even in a disordered phase, then almost all of spins are updated in the same manner and very small fraction of spins are effectively updated. Indeed, while the cluster size ratio is moderate in the two-dimensional ferromagnetic Ising model at the critical temperature, that in the antiferromagnetic Heisenberg model on the two-dimensional triangular lattice, is close to 1 or 0 independent of the system size at an estimated temperature of a possible phase transition [38], see Fig. 2.1. The same problem is seen in other complicated models such as the spin glass models in three-dimensions, and particle models in the geometric cluster algorithm by Dress and Krauth.

The cluster algorithms have been developed for systems with two-body interactions. We can easily generalize the algorithms to a system including one-body external fields, like magnetic fields, while their performance usually decreases for such systems. A more serious problem of the cluster algorithms is that their generalization to systems with many-body interactions is difficult. Note that a recent study indicates a possible way to design a cluster algorithm for many-body interactions [39].

## 2.4 Extended Ensemble algorithm

Thanks to the cluster algorithms proposed in the late 1980s, slowing down associated with equilibrium continuous phase transitions in simple spin systems such as ferromagnetic models is almost completely eliminated, and much precise values of transition temperatures and critical exponents are obtained for the models, see Ref. [40] for example. However, the cluster algorithms turned out not to be efficient for models with frustration including spin glasses. Also, their generalization to other models is not trivial as mentioned above.

In 1990s, Monte Carlo algorithms that avoids sampling from the Gibbs distribution with fixed parameters appeared: Extended (or generalized) ensemble algorithms. The idea of

extended ensemble algorithms is to sample from an artificial ensemble in which mixing and relaxation of a Markov chain is faster than the original one in the target distribution. We discuss briefly some of extended ensemble algorithms in this section.

### 2.4.1 Multicanonical algorithm

First-order phase transitions caused by multiple free-energy minima show a discontinuous change of a thermodynamic dominant state with $O(N)$ finite jumps of physical quantities in the thermodynamic limit. A coexistence state mixed with those two states has a finite surface free-energy of $O\left(L^{d-1}\right)$ ($L$ is the linear dimension of a system and $d$ is the spatial dimension) and thus it has an exponentially small probability in the canonical ensemble. Conventional local Monte Carlo algorithms have to go through the intermediate states with a nucleation process to make a transition from one state to another one, and it takes exponentially long time for sampling due to the small probability.

The canonical average of a physical quantity $A$ at inverse temperature $\beta$ can be com-

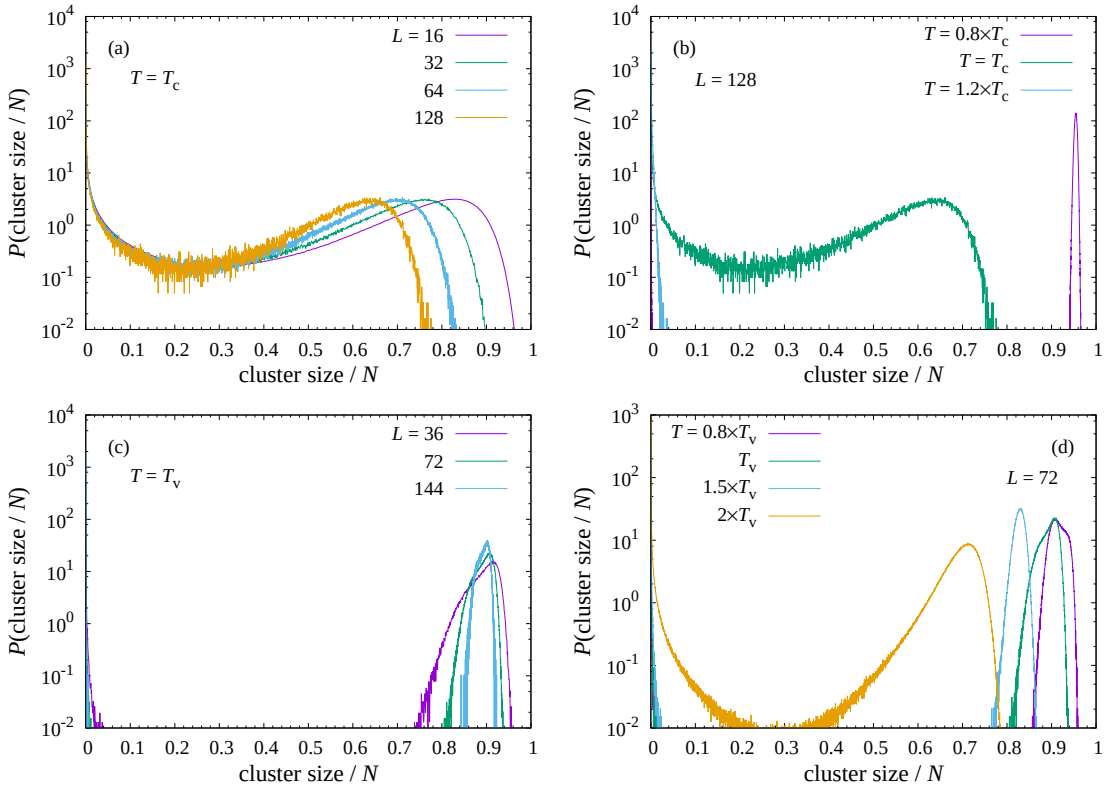


Fig. 2.1: (a,b) The distribution function of the cluster size in the Wolff algorithm for the ferromagnetic Ising model on a two-dimensional square lattice at the critical temperature, and at various temperatures, respectively. (c,d) The distribution function of the cluster size in the Wolff algorithm for the antiferromagnetic Heisenberg model on a two-dimensional triangular lattice at $T = T_{\mathrm{v}}$, a transition temperature of a possible phase transition, and at various temperatures, respectively. In (c) and (d), $T_{\mathrm{v}}/J = 0.285$ is used, which is estimated in Ref. [38].

puted by using samples drawn from an arbitrary distribution function as

$$\begin{aligned}\langle A\rangle_\beta &= \frac{\int d\boldsymbol{\sigma} A(\boldsymbol{\sigma}) \exp\left(-\beta E(\boldsymbol{\sigma})\right)}{\int d\boldsymbol{\sigma} \exp\left(-\beta E(\boldsymbol{\sigma})\right)} \\ &= \frac{\int d\boldsymbol{\sigma} A(\boldsymbol{\sigma}) \exp\left(-\beta E(\boldsymbol{\sigma}) - f(\boldsymbol{\sigma})\right) \exp(f(\boldsymbol{\sigma}))}{\int d\boldsymbol{\sigma} \exp\left(-\beta E(\boldsymbol{\sigma}) - f(\boldsymbol{\sigma})\right) \exp(f(\boldsymbol{\sigma}))} \\ &= \frac{\left[A(\boldsymbol{\sigma}) \exp(-\beta E(\boldsymbol{\sigma}) - f(\boldsymbol{\sigma}))\right]_f}{\left[\exp(-\beta E(\boldsymbol{\sigma}) - f(\boldsymbol{\sigma}))\right]_f}. \end{aligned} \tag{2.24}$$

In this expression, $\boldsymbol{\sigma}$ stands for a configuration of the system, $\exp\left(f\left(\boldsymbol{\sigma}\right)\right)$ is an arbitrary function of $\boldsymbol{\sigma}$, and $[\cdots]_f$ is average in the probability distribution $\exp\left(f\left(\boldsymbol{\sigma}\right)\right) / \int d\boldsymbol{\sigma}' \exp\left(f\left(\boldsymbol{\sigma}'\right)\right)$. We choose $f\left(\boldsymbol{\sigma}\right) = -\beta E\left(\boldsymbol{\sigma}\right)$ for the usual Gibbs distribution. The multicanonical algorithm [41, 42] is designed to sample from an artificial probability distribution with $f\left(\boldsymbol{\sigma}\right) = -\log \Omega\left(E\left(\boldsymbol{\sigma}\right)\right)$ to avoid the exponentially slow nucleation process, where $\Omega\left(E\right)$ is the density of states. The Metropolis–Hastings acceptance probability is frequently used to sample the probability distribution. With this probability distribution, we obtain a distribution function of the energy $E$

$$P\left(E\right) = \frac{\int \delta\left(E - E\left(\boldsymbol{\sigma}\right)\right) \Omega\left(E\left(\boldsymbol{\sigma}\right)\right)^{-1} d\boldsymbol{\sigma}}{\int \Omega\left(E\left(\boldsymbol{\sigma}\right)\right)^{-1} d\boldsymbol{\sigma}} = \frac{\int \Omega\left(E'\right) \delta\left(E - E'\right) \Omega\left(E'\right)^{-1} dE'}{\int \Omega\left(E'\right) \Omega\left(E'\right)^{-1} dE'} = \text{const.} \tag{2.25}$$

This means that we can sample an energy with probability independent of its value in contrast to the canonical ensemble in which intermediate energies between two thermodynamic relevant energies around a first-order transition point appears with exponentially small probability. Furthermore, the system can easily go through the intermediate region (via coexistence states) in the multicanonical ensemble, and thus this algorithm does not suffer from the exponential slowing down caused by the nucleation process. The density of states $\Omega\left(E\right)$, however, cannot be obtained a priori although it is determined only by the system Hamiltonian. B. A. Berg and T. Neuhaus pointed out that the exact density of states is not necessary to implement the multicanonical algorithm, and an approximate empirical density of state $\tilde{\Omega}\left(E\right)$ estimated by an iterative procedure is usually used in practice, see detailed discussions in Ref. [42, 43]. The Wang–Landau algorithm [44, 45] can also be utilized to estimate the density of states.

Thanks to the multicanonical algorithm, the exponential slowing down caused by the nucleation process in the first-order phase transitions is eliminated. However, for large systems, where the algorithm has to travel around many energy levels, a polynomially long time $O\left(N^2\right)$ is required for simulations as the speed of the algorithm is still limited by a diffusive process in the space of the energy. Parallelization in the energy space, or more sophisticated update scheme rather than the simple Metropolis–Hastings algorithm which can change the diffusive behavior to a ballistic one is expected to be necessary.

### 2.4.2 Exchange Monte Carlo method

The exchange Monte Carlo method, also known as "parallel tempering" algorithm, was introduced in Refs. [46–48]. In this algorithm, we simulate multiple replicas of a system with different parameters, and exchange the parameters between two replicas with keeping detailed balance. This simple procedure greatly accelerates relaxation of the system. Indeed, it has been numerically proven to be efficient for many kinds of systems such as spin glasses, protein models and structural glasses [48–56]. In the following, we discuss the exchange Monte Carlo method with different temperatures while it can be

applied to the case with any intensive parameters. Let us consider a composite system that consists of $M$ replicas with the same Hamiltonian and different inverse temperatures $\beta_1, \cdots, \beta_M$ ($\beta_1 > \cdots > \beta_M$). The Gibbs distribution of the system is written as

$$P\left(\{E_i\};\{\beta_i\}\right) = \prod_i p\left(E_i;\beta_i\right) = \prod_i \frac{\exp\left(-\beta_i E_i\right)}{Z\left(\beta_i\right)}, \tag{2.26}$$

where $E_i$ is the energy of replica $i$ and $Z\left(\beta_i\right)$ is the partition function of the system at $\beta_i$. Two temperatures are exchanged with probability $W_{jk}$ which satisfies the detailed balance condition

$$P\left(\{E_i\};\{\cdots,\beta_j,\cdots,\beta_k,\cdots\}\right) W_{jk} = P\left(\{E_i\};\{\cdots,\beta_k,\cdots,\beta_j,\cdots\}\right) W_{kj}. \tag{2.27}$$

We can choose

$$W_{jk} = \min\left\{1, \exp\left(\left(\beta_j - \beta_k\right)\left(E_j - E_k\right)\right)\right\} \tag{2.28}$$

for the Metropolis type, and

$$W_{jk} = \frac{\exp\left(\left(\beta_j - \beta_k\right)\left(E_j - E_k\right)\right)}{\exp\left(\left(\beta_j - \beta_k\right)\left(E_j - E_k\right)\right) + \exp\left(\left(\beta_k - \beta_j\right)\left(E_j - E_k\right)\right)} \tag{2.29}$$

for the heat-bath type acceptance probabilities. It is usual to try an exchange of two neighboring temperatures in practice. Note that the exchange Monte Carlo algorithm itself does not change configurations of the system, and we have to combine other algorithms such as Metropolis–Hastings algorithm.

The exchange Monte Carlo method applied to Ising spin glass models can be interpreted as a family of Replica Monte Carlo algorithm [57, 58], in which a cluster identified by an overlap between two replicas is updated [43]. Replica Monte Carlo algorithm is claimed to be much more efficient for a two-dimensional Ising spin glass model than the exchange Monte Carlo method while their performances are comparable for a three-dimensional Ising spin glass model [58]. However, it is difficult to generalize the concept of the cluster in Replica Monte Carlo algorithm to other models such as particle models. On the other hand, the exchange Monte Carlo method that utilizes only macroscopic physical quantities can be easily applied to many other models. Indeed, there is a tremendous amount of its applications ranging from statistical inference to quantum systems. Even for spin glass models, the exchange Monte Carlo method is the most used algorithm today.

It is necessary to keep the exchange probabilities high so that each replica can wander around the temperature space in a short time, and low exchange probabilities between replicas make the performance of the exchange Monte Carlo algorithm much worse. We expect the exchange probability is moderately high when the static energy distributions of two neighboring temperatures have a large enough overlap. Thus, first-order phase transitions are the most notorious examples that the algorithm does not work well: The exchange probability between two fixed temperatures below and above a first-order phase transition point decays exponentially with the system size due to a finite jump in the energy. The algorithm, in contrast to the multicanonical algorithm, is not suitable to reduce slowing down caused by the nucleation process in first phase transitions

Even for continuous phase transitions, we need $O\left(\sqrt{N}\right)$ replicas for a fixed interval of temperature to keep the probability $O\left(1\right)$ if the distribution of the energy is Gaussian. This large number of replicas also makes the performance of the algorithm worse even if the exchange probabilities are high; a time that each replica tunnels from the lowest temperature to the highest one scales as $\sim O\left(N\right)$ even if the dynamics in the temperature space is diffusive. Furthermore, the long correlation time of the energy of a system at low

temperature makes the exchange dynamics in the temperature space slower even if the exchange probabilities are high enough [*5]. We have to be very careful about not only the exchange probabilities but also the tunneling time in the temperature space.

## 2.5 Irreversible algorithm

The detailed balance condition forbids any net probability flow in the stationary distribution of a Markov chain. The chain with the condition is reversible, and have a diffusive random-walk behavior. Most Markov chain Monte Carlo algorithms were developed in the framework of detailed balance, and almost all existing Monte Carlo algorithms including those discussed above satisfy it. Note that sequential or checkerboard (or any other systematic) updates with the conventional algorithms break the detailed balance condition weakly, but convergence to the stationary distribution of such updates was also proved [59].

Although it has been widely known that detailed balance is sufficient for the convergence of Markov chains, few attempts were made to construct an irreversible algorithm, which breaks detailed balance, until the pioneering work by P. Diaconis, S. Holmes, and R. M. Neal [60] [*6], which discusses a one-dimensional irreversible Markov chain. In this section, we discuss the idea of "lifting" of Markov chain, a concept introduced by F. Chen, L. Lovász and I. Pak [61], and a practical algorithm by K. S. Turitsyn, M. Chertkov and M. Vecelja, which is a lifting algorithm. We also discuss another practical algorithm proposed by H. Suwa and S. Todo.

### 2.5.1 Lifting algorithm

#### 2.5.1.1 Lift of Markov chain

A lift of a Markov chain has been the most extensively studied framework of irreversible Markov chains. The idea of lifting is to generate a net probability flow and enhance mixing of a Markov chain by adding auxiliary variables. In Ref. [61], F. Chen and L. Lovász and I. Pak gave a general definition of a lift of a Markov chain: A Markov chain $\hat{X}$ on a discrete state space $\hat{V}$ is a lift of another Markov chain $X$ on $V$ if there exists a map $f : \hat{V} \to V$ such that

$$\pi(i) = \hat{\pi}\left(f^{-1}(i)\right) = \sum_{a \in f^{-1}(i)} \hat{\pi}(a), \tag{2.30}$$

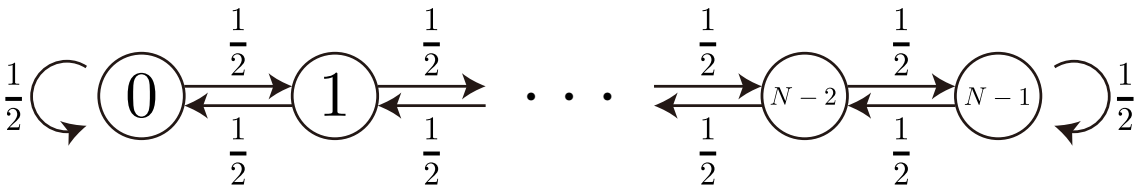


Fig. 2.2: A one-dimensional reversible Markov chain. The stationary distribution is the uniform distribution.

[*5] The exchange probabilities only depend on the thermodynamic energy distributions. Microscopic dynamics does not change the exchange probabilities, but can enhance tunneling in the temperature space by reducing the correlation time of the energy.

[*6] The paper first appeared in TR BU-1385-M, Biometric Unit, Cornell University (1997)

$$T(i,j) = \sum_{a \in f^{-1}(i), b \in f^{-1}(j)} \frac{\hat{\pi}(a)}{\hat{\pi}(f^{-1}(i))} \hat{T}(a,b), \tag{2.31}$$

where $T$ and $\hat{T}$ are the transition probabilities of $X$ and $\hat{X}$, respectively.

An irreversible Markov chain that P. Diaconis, S. Holmes and R. M. Neal [60] discussed is the first proposed lift of a Markov chain. Let us consider a Markov chain on a set of discrete states $V$ with the stationary distribution $\pi(i) = 1/N$ ($N = |V|$, $i \in V$), see Fig. 2.2. If we choose the transition probability $T(i,j)$ from a state $i$ to $j$ as

$$T(i,j) = \begin{cases} \frac{1}{2} & \text{if } j = i \pm 1 \text{ or } i = j = 0, N-1 \\ 0 & \text{otherwise,} \end{cases} \tag{2.32}$$

the Markov chain trivially satisfies the detailed balance condition, and thus it is reversible. Note that this Markov chain is aperiodic thanks to the boundary condition. To construct an irreversible Markov chain, the state space $V$ is doubled by adding an extra variable $\sigma$ that takes $\pm$: Each state $i$ is divided into $(i,+)$ and $(i,-)$. The transition probability $\hat{T}((i,\sigma),(j,\sigma'))$ is chosen as

$$\begin{cases} \hat{T}((i,+),(i+1,+)) = 1 - \frac{1}{N} & \text{if } 0 \le x < N-1 \\ \hat{T}((N-1,+),(N-1,-)) = 1 - \frac{1}{N} & \\ \hat{T}((i,+),(i+1,-)) = \frac{1}{N} & \text{if } 0 \le x < N-1 \\ \hat{T}((N-1,+),(N-1,+)) = \frac{1}{N} & \\ \hat{T}((i,-),(i-1,-)) = 1 - \frac{1}{N} & \text{if } 0 < x \le N-1 \\ \hat{T}((0,-),(0,-)) = 1 - \frac{1}{N} & \\ \hat{T}((i,-),(i-1,+)) = \frac{1}{N} & \text{if } 0 < x \le N-1 \\ \hat{T}((0,-),(0,-)) = 1 - \frac{1}{N} & \end{cases} \tag{2.33}$$

This Markov chain with $\hat{T}$ satisfies the global balance condition with the stationary distribution $\hat{\pi}(i,\sigma) = 1/2N$, but clearly violates detailed balance as, for example, $\hat{\pi}(i,+)\hat{T}((i,+),(i+1,+)) \neq \hat{\pi}(i+1,+)\hat{T}((i+1,+),(i,+))$. As an important property of this irreversible chain, the marginal distribution of $\sigma$ with $\{\hat{\pi}(i,\sigma)\}$ is equivalent to the original stationary distribution $\{\pi(i)\}$ of the reversible chain, as Eq. (2.30). Eq. (2.31) can also be easily confirmed to hold. See Fig. 2.3 for a schematic picture of the irreversible Markov chain.

F. Chen *et al.* rigorously proved in Ref. [61] that the best possible reduction of the mixing time with an appropriate lifting for Markov chains on discrete states is its square root. We have to notice that a unit time step is defined as one update trial of a variable rather than $N$ trials, which is usually used in Monte Carlo simulations for statistical mechanics. On the other hand, if a lift of a reversible Markov chain is also reversible, the reduction of the mixing time is limited by $O(\log N)$. Their result for the square-root reduction is recently generalized to Markov chains on continuous state spaces [62].

#### 2.5.1.2 Turitsyn–Chertkov–Vecelja algorithm

Applying the concept of the lifting, K. S. Turitsyn, M. Chertkov, and M. Vucelja proposed an irreversible Monte Carlo algorithm [63]. In their algorithm, a state space of a reversible Markov chain with the transition probability $T(i,j)$ and the stationary probability $\pi(i)$, are doubled by an extra variable $\sigma = \pm$, exactly as Ref. [60]. A configuration of the system is updated according to the transition probability $\hat{T}_{\pm}(i,j)$ that is chosen so that the "skew" detailed balance condition, $\hat{T}_{+}(i,j)\pi_i = \hat{T}_{-}(j,i)\pi_j$ ($T(i,j) = \hat{T}_{+}(i,j) + \hat{T}_{-}(i,j)$), is fulfilled. They applied the algorithm to the mean-field (or infinite-range) ferromagnetic

Ising model defined by the Hamiltonian $H(\{\tau_i\}) = -\frac{J}{N}\sum_{i<j}\tau_i\tau_j$ ($\tau_i = \pm 1$). Because of the mean-field nature of the system, every state of the system can be specified by its magnetization $m$ except for a permutation of the labels of sites, and its dynamics with reversible local algorithms is equivalent to that of a one-dimensional finite Markov chain. So their algorithm successfully reduce the correlation time, and the dynamical critical exponent of the system [63]. However, for two- and three-dimensional ferromagnetic Ising models in which the dynamics is essentially different from a one-dimensional Markov chain, the algorithm is not so efficient to reduce the exponent [64].

### 2.5.2 Suwa–Todo algorithm

A few irreversible Monte Carlo algorithms have been known until today. While most of them are based on the lifting framework discussed above, the Suwa–Todo algorithm proposed in Ref. [65] breaks detailed balance without any extra variable, and is not a lifting algorithm. Let us suppose an update in which a next state will be chosen from a set of states $V = \{0, \cdots, K-1\}$ with the stationary probability $\pi_i$ ($i = 0, \cdots, K-1$). We construct the transition probability $T(i,j)$ with satisfying the global balance condition

$$\pi_i = \sum_{j \in V} \pi_j T(j,i), \quad i \in V. \tag{2.34}$$

The global balance condition means that every stationary probability distribution $\pi_i$ of state $i$ is composed of fragments $\pi_j T(j,i)$ of $\pi_j$ ($j \in V$), and $T(j,i)$ determines how much ratio of $\pi_j$ goes to $\pi_i$. The idea of the Suwa–Todo algorithm is to design $(T(i,j))_{i,j}$ so that every stationary probability $\pi_i$ is filled by other stationary probabilities with as few states as possible. That is equivalent to choose a matrix $(\pi_i T(i,j))_{ij}$ so that the number of elements and the values of the diagonal elements is minimized. This is accomplished by choosing

$$\pi_i T(i,j) = \max\left[0, \min\left[\Delta_{ij}, \pi_i + \pi_j - \Delta_{ij}, \pi_i, \pi_j\right]\right]. \tag{2.35}$$

We can easily understand the idea visually, see Ref. [65]. The resultant transition probability of the Suwa–Todo algorithm is equivalent to the Metropolis acceptance probability if $K = 2$. They showed that this algorithm may be rejection-free when $K$ is large, and can shorten the (integrated) correlation time of a ferromagnetic Potts model and a spin-half antiferromagnetic $XXZ$ model. Although, unfortunately, the algorithm cannot reduce the dynamical critical exponent of a ferromagnetic Potts model [66], we can expect that the

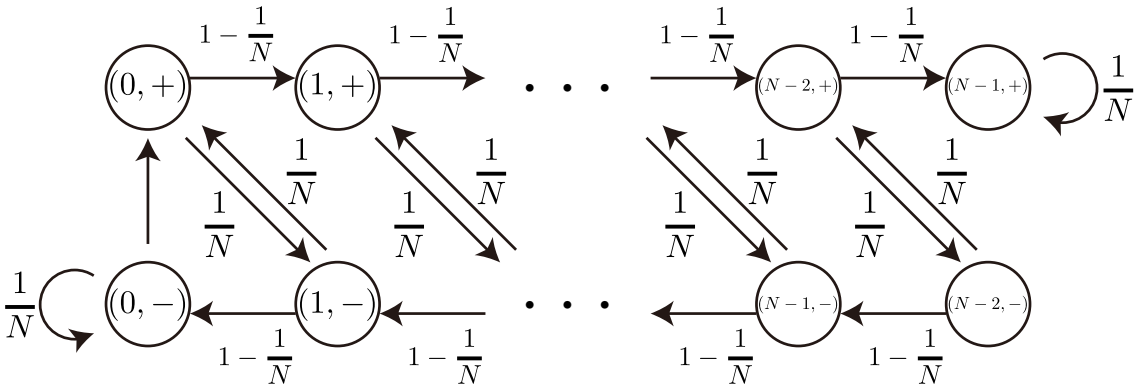


Fig. 2.3: A one-dimensional irreversible Markov chain. The stationary distribution is the uniform distribution.

Suwa–Todo algorithm allows us to simulate many models more efficiently with an $O(1)$ reduction of the correlation time.

# 3

# Event-Chain Monte Carlo algorithm

Monte Carlo algorithms that breaks detailed balance but satisfies global balance can enhance decorrelation as we discussed in the previous section. In particular, for lifting algorithms defined above, it is mathematically proven that breaking detailed balance can reduce in principle the mixing time of the Markov chain to its square root [61]. However, there had been no known algorithm breaking detailed balance that was shown to change the dynamical exponent $z$ even for simple ferromagnetic models in finite dimensions with a finite-temperature phase transition.

In this chapter, we introduce and discuss the event-chain Monte Carlo (ECMC) algorithm for particle and continuous spin models. The ECMC algorithm utilizes continuous degrees of freedom of a system while that could be generalized to a model with discrete states by introducing auxiliary continuous variables. We will show that the algorithm can change the dynamics qualitatively, and reduce the dynamical critical exponent for the three-dimensional ferromagnetic Heisenberg model. The performance of the algorithm for a frustrated spin model and a spin glass model are also discussed.

## 3.1 Event-chain algorithm for particle systems

### 3.1.1 Event-chain algorithm for hard spheres

Before discussing the ECMC algorithm, we review an avalanche algorithm for hard spheres that may induce a non-local cluster move to the system [37]. Hard spheres interact with each other by a hard-core potential

$$U(r) = \begin{cases} 0 & r > \sigma \\ \infty & r < \sigma \end{cases} \tag{3.1}$$

that forbids any overlap of spheres, where $\sigma$ is the radius of hard spheres. The hard sphere system in spatial dimensions $d \geq 2$ shows phase transitions in the high density region. The Metropolis algorithm is the simplest way to simulate hard spheres, but almost every proposed move is rejected and it falls out of equilibrium if the density gets higher. The avalanche algorithm is one kind of cluster algorithms that may update many hard spheres in a coherent way. The idea of the avalanche algorithm is not to reject any finite move that causes an overlap between two hard spheres: When the move makes an overlap between the sphere and another one, then the overlapped hard sphere moves with the same displacement. This dynamics can induce a cluster update in a chain-like manner, and may satisfy the detailed balance condition, i.e. the reverse chain can be constructed uniquely. However, the finite move of spheres often makes an overlap with multiple spheres. In this case, the chain branches, and then it is impossible to construct the reverse chain starting from one moving sphere unless the chain happens to converge

to one sphere in the end.

In Ref. [67], E. P. Bernard, W. Krauth, and D. Wilson resolved this serious problem in the avalanche algorithm by introducing infinitesimal moves. Infinitesimal moves make a multiple overlap occur with probability 0, and the chain never branches. We thus can construct the reverse chain uniquely. Each chain is truncated when the total displacements of hard spheres in the chain reach to a length $\ell$ that is a parameter of the ECMC algorithm. This algorithm with infinitesimal moves, referred to as the event-chain algorithm in [67] and the following, induces a rejection-free large cluster update. The only randomness for the ECMC algorithm for hard spheres is the choice of the initial direction of moves with fixed truncated length $\ell$. For hard spheres in a translationally symmetric box in $d$ dimensions, the algorithm can break the detailed balance condition yet satisfying the global balance condition by choosing the initial direction from only positive basis vectors $+\boldsymbol{e}_i$ $(i = 0, \cdots, d-1)$; no reverse chain appears during simulations, and every moved sphere never goes back to its former position.

The event-chain algorithm, especially the irreversible version, have been shown to outperform conventional algorithms, such as the Metropolis–Hastings Monte Carlo and the event-driven molecular dynamics [24, 67, 68]. E. P. Bernard and W. Krauth applied the algorithm to simulate two-dimensional $1024^2$ hard disks, and successfully equilibrated the system in the high density region [69].

### 3.1.2 Event-chain algorithm for particles with more general potentials

The original ECMC algorithm for hard spheres utilizes the concept of a collision, that is, a rejection of an infinitesimal move by another sphere. For particles with a more general potential at finite temperature, it is unclear how to define a collision between two particles that is expected to depend on temperature. In Ref. [70], E. P. Bernard and W. Krauth extended the ECMC algorithm to a general potential with a discretization of potentials. They define a collision as an event where an interacting energy between the moving particle and another one raises. This even-driven algorithm is a direct generalization of the original ECMC algorithm, and they showed in the paper that it reduces the correlation time. However, according to the definition of the collision, this generalized ECMC algorithm does not produce samples from the canonical distribution by itself; it never changes the energy of the system.

What is an appropriate definition of a collision that allows us to sample the canonical ensemble? We expect the collision occurs at finite temperature in a stochastic manner. The answer is given by E. A. J. F. Peters and G. de With in Ref. [71] that introduced an event-driven Monte Carlo algorithm for particles. Two years later, M. Michel, S. C. Kapfer, and W. Krauth [72] introduced the factorized Metropolis filter, and revealed that the event-chain and the event-driven algorithm by Peters and de With are lifting algorithms.

To illustrate the stochastic collision, let us consider two particles interacting with each other via $U(r)$ (where $r$ is the distance between two particles) in a $d$-dimensional box. The Metropolis–Hastings algorithm gives an acceptance probability when a particle $i$ $(i = 1, 2)$ moves from $\boldsymbol{x}_i$ to $\boldsymbol{x}_i + \boldsymbol{v}\Delta x$ as

$$P\left(\{\boldsymbol{x}_j\}_{j=1,2}, (i, \boldsymbol{v}), \Delta x\right) = \min\left[1, \exp\left(-\beta E_{(i,\boldsymbol{v})}(\Delta x)\right)\right] \tag{3.2}$$

$$= \exp\left(-\beta \max\left[0, E_{(i,\boldsymbol{v})}(\Delta x)\right]\right), \tag{3.3}$$

where $\beta$ is inverse temperature, $\boldsymbol{v}$ is a $d$-dimensional unit vector, and $E_{(i,\boldsymbol{v})}(\Delta x) = U\left(|\boldsymbol{x}_i + \boldsymbol{v}\Delta x - \boldsymbol{x}_{i'}|\right) - U\left(|\boldsymbol{x}_i - \boldsymbol{x}_{i'}|\right)$ (the other particle is denoted as $i' = |1 - i|$). In

the infinitesimal limit $\Delta x \to +0$,

$$P\left(\{\boldsymbol{x}_j\}_{j=1,2}, (i,\boldsymbol{v}), \Delta x \to +0\right) = \exp\left(-\beta \max\left[0, \frac{d}{dx} E_{(i,\boldsymbol{v})}(x)\right] dx\right), \tag{3.4}$$

and the rejection probability is

$$1 - P\left(\{\boldsymbol{x}_j\}_{j=1,2}, (i,\boldsymbol{v}), \Delta x \to +0\right) = \beta \max\left[0, \frac{d}{dx} E_{(i,\boldsymbol{v})}(x)\right] dx. \tag{3.5}$$

Instead of step-by-step acceptance-or-rejection procedure, we can sample in an event-driven way [73] a location $\boldsymbol{x}_i' = \boldsymbol{x}_i + s\boldsymbol{v}$ where a finite displacement $s$ along $\boldsymbol{v}$ is sampled via the conditional acceptance probability

$$P\left(\boldsymbol{x}_i \to \boldsymbol{x}_i'\right) = \exp\left(-\beta \int_0^s \max\left[0, \frac{d}{dt} E_{(i,\boldsymbol{v})}(t)\right] dt\right). \tag{3.6}$$

Considering the rejection as a stochastic collision, we can construct the event-chain algorithm for two particles with general potentials in the same manner as one for hard spheres, and sample from the Gibbs distribution.

To generalize the two-particle ECMC algorithm to $N$ particles, we introduce the factorized Metropolis acceptance probability

$$P_{\mathrm{fMet}}\left(\{\boldsymbol{x}_i\} \to \{\boldsymbol{x}_i'\}\right) = \prod_{\alpha} \exp\left(\max\left[0, \Delta E_\alpha\right]\right), \tag{3.7}$$

where $\{E_\alpha\}$ is a set of two-body interacting energies that is a decomposition of the system Hamiltonian, and $\Delta E_\alpha$ is the difference of $E_\alpha$ between $\{\boldsymbol{x}_i\}$ and $\{\boldsymbol{x}_i'\}$. We can easily check that $P_{\mathrm{fMet}}$ can satisfy detailed balance with an appropriate proposal probability as the usual Metropolis–Hastings acceptance probability. While this acceptance probability is usually lower than the Metropolis–Hastings acceptance probability, it has a distinct characteristic; the proposed move is accepted only if every interacting energy $E_\alpha$ agrees with the move. This means that we can define the collision for each pair of interacting particles with the factorized Metropolis probability by setting $\{E_\alpha\}$ to pairwise interacting energies where each is involving two particles.

In the event-chain algorithm, an extra variable $(i,\boldsymbol{v})$ changes at the moment when a move is rejected, and specifies which particle moves and what direction it moves. This can be regarded as a lifting variable that is updated as $(i,\boldsymbol{v}) \to (j,\boldsymbol{v})$ at the moment when a move is rejected, and help the algorithm break detailed balance. Although no reverse chain appears in the algorithm if the lifting variable, the vector $\boldsymbol{v}$, is chosen only from a set of basis vectors $\{+\boldsymbol{e}_0, \cdots, +\boldsymbol{e}_{d-1}\}$, any forward chain has to have the same probability to appear as its reverse chain when the vector $\boldsymbol{v}$ is chosen from $\{\pm\boldsymbol{e}_0, \cdots, \pm\boldsymbol{e}_{d-1}\}$. We thus cannot apply the event-chain algorithm with the update scheme $(i,\boldsymbol{v}) \to (j,\boldsymbol{v})$ to a system with a pair interacting energy $E\left(\boldsymbol{x}_i, \boldsymbol{x}_j\right)$ that does not satisfy

$$\frac{d}{dt} E_{(i,\boldsymbol{v})}(t) = -\frac{d}{dt} E_{(j,\boldsymbol{v})}(t) \left(= \frac{d}{dt} E_{(j,-\boldsymbol{v})}(t)\right), \tag{3.8}$$

where $E_{(i,\boldsymbol{v})}(t) = E\left(\boldsymbol{x}_i + t\boldsymbol{v}, \boldsymbol{x}_j\right) - E\left(\boldsymbol{x}_i, \boldsymbol{x}_j\right)$ (the last equation always holds). The easiest way to apply the algorithm to such a system is to change the lifting variables $(i,\boldsymbol{v})$ to $(i,-\boldsymbol{v})$ rather than $(j,\boldsymbol{v})$, when a collision occurs (or a move is rejected) by interacting energies which do not satisfy Eq. (3.8); we have a trivial equation for any interacting energy

$$\frac{d}{dt} E_{(i,\boldsymbol{v})}(t) = -\frac{d}{dt} E_{(i,-\boldsymbol{v})}(t). \tag{3.9}$$

However, this update of the lifting variables is expected to worsen the performance of the event-chain algorithm because moved particles can go back to their former position in a chain and the algorithm is reversible. More sophisticated update scheme is required to improve the algorithm for the case.

The event-driven Monte Carlo algorithm by Peters and de With [71] includes both the event-chain algorithm and the event-driven molecular dynamics for hard spheres as special cases. In contrast to the event-driven molecular dynamics in which all particles move at any time, only one single particle moves in the event-chain algorithm. Therefore, its implementation is much easier and faster than the event-driven molecular dynamics. On the other hand, the correlation time of the event-driven molecular dynamics in the high density region measured in the number of collisions is shorter than that of the event-chain algorithm. We thus could expect that the Peters–de With algorithm with all particles moving at finite temperature is more efficient than the event-chain algorithm in the sense of the time unit, especially for systems with interactions which do not satisfy Eq. (3.8).

## 3.2 Event-chain algorithm for continuous spin systems

The event-chain algorithm applied to some particle systems is shown to be much more efficient than the usual Metropolis–Hastings algorithm. As the algorithm utilizes continuous degrees of freedom of a system, we would expect that the algorithm can be generalized to any model that has continuous variables. In this section, we discuss the event-chain algorithm for classical continuous spin models, especially for classical Heisenberg spin models, and its performance.

We begin with the simplest Heisenberg spin model defined by the Hamiltonian

$$H\left(\{\boldsymbol{S}_i\}\right) = -\sum_{\langle i,j\rangle} \boldsymbol{S}_i \cdot J_{ij} \boldsymbol{S}_j - \sum_i \boldsymbol{h}_i \cdot \boldsymbol{S}_i, \tag{3.10}$$

where $\boldsymbol{S}_i$ is a three-dimensional vector with fixed length $|\boldsymbol{S}_i| = 1$, the bracket $\langle \cdot, \cdot \rangle$ represents a pair of interacting spins, $J_{ij}$ is a $3 \times 3$ matrix, and $\boldsymbol{h}_i$ is a three-dimensional vector. Let us consider a decomposition of the Hamiltonian (3.10)

$$H\left(\{\boldsymbol{S}_i\}\right) = \sum_{\alpha, i<j} E_{ij}^{\alpha}\left(\boldsymbol{S}_i, \boldsymbol{S}_j\right) + \sum_{\alpha, i} E_i^{\alpha}\left(\boldsymbol{S}_i\right), \tag{3.11}$$

where $E_{ij}^{\alpha}\left(\boldsymbol{S}_i, \boldsymbol{S}_j\right) = -\boldsymbol{S}_i \cdot J_{ij}^{\alpha} \boldsymbol{S}_j$, $E_i^{\alpha}\left(\boldsymbol{S}_i\right) = -\boldsymbol{h}_i^{\alpha} \cdot \boldsymbol{S}_i$, and $\sum_{\alpha} J_{ij}^{\alpha} = J_{ij}$, $\sum_{\alpha} \boldsymbol{h}_i^{\alpha} = \boldsymbol{h}_i$. As we discussed in the previous section, each $E_{ij}\left(\boldsymbol{S}_i, \boldsymbol{S}_j\right)$ has to satisfy Eq. (3.8) to update the lifting variables as $(i, \boldsymbol{v}) \to (j, \boldsymbol{v})$. In the event-chain algorithm for systems composed of continuous $O(n)$ spins ($n \geq 2$), spins are rotated with respect to a vector $\boldsymbol{v}$. The condition Eq. (3.8) thus is equivalent to the following condition for the Hamiltonian (3.10):

$$\begin{aligned} \frac{d}{dt}\left(R_{\boldsymbol{v}}(t)\, \boldsymbol{S}_i \cdot J_{ij}^{\alpha} \boldsymbol{S}_j\right) = \frac{d}{dt}\left(\left(J_{ij}^{\alpha}\right)^{\mathrm{T}} \boldsymbol{S}_i \cdot R_{-\boldsymbol{v}}(t)\, \boldsymbol{S}_j\right) &\Leftrightarrow \boldsymbol{S}_i \cdot D_{\boldsymbol{v}} J_{ij}^{\alpha} \boldsymbol{S}_j = \boldsymbol{S}_i \cdot J_{ij}^{\alpha} D_{\boldsymbol{v}} \boldsymbol{S}_j \\ &\Leftrightarrow \left[J_{ij}^{\alpha}, D_{\boldsymbol{v}}\right] = 0, \end{aligned} \tag{3.12}$$

where $R_{\boldsymbol{v}}(t)$ is a rotation matrix around a vector $\boldsymbol{v}$ with an angle $t$, and $D_{\boldsymbol{v}} = \frac{d}{dt} R_{\boldsymbol{v}}(t)\big|_{t=0}$. Note that the matrix $D_{\boldsymbol{v}}$ is skew symmetric. If a vector $\boldsymbol{v}$ satisfies Eq. (3.12) for a certain $J_{ij}^{\alpha}$, we can update as $(i, \boldsymbol{v}) \to (j, \boldsymbol{v})$ when a collision occurs due to the interaction energy $E_{ij}^{\alpha}$ (or a infinitesimal move is rejected by $E_{ij}^{\alpha}$). We should stress here that the Hamiltonian is invariant under the global transformation with $R_{\boldsymbol{v}}(t)$ if and only if the condition Eq. (3.12) holds for every $J_{ij}^{\alpha}$.

For the case that a collision occurs with external fields, $\{\boldsymbol{h}_i\}$, we no longer can change the moving spin. While another update scheme might be possible, the easiest update of the lifting variable is, again, $(i, \boldsymbol{v}) \to (i, -\boldsymbol{v})$. Initial directions of a rotation, $\boldsymbol{v}$, have to be chosen from a set of vectors that contains pairs of opposite vectors to satisfy the balance condition.

According to the above discussion, we can expect that the performance of the event-chain algorithm is maximal when it is applied to a system with continuous symmetry: The detailed balance condition can be maximally broken for the system. If a system does not have any continuous symmetry, only one spin (or particle) moves in a chain with the update scheme of the lifting variables $(i, \boldsymbol{v}) \to (i, -\boldsymbol{v})$. The event-chain algorithm can update the system only in a local manner, and its dynamics is essentially equivalent to local Monte Carlo algorithms for this case.

### 3.2.1 Performance of the event-chain algorithm

To demonstrate the performance of the ECMC algorithm for some continuous spin models, we consider an autocorrelation function of a physical quantity $\mathcal{O}$ defined in Eq. (2.8). In our actual simulations, one unit Monte Carlo time step is defined as one update per spin. The length of each chain $\ell$ is set to $N\pi/10$ in the following. We use the exponential correlation time Eq. (2.9) to find the slowest mode in the autocorrelation function. Due to the finiteness of available data, the autocorrelation function $C_{\mathcal{O}}(t)$ has a relatively large statistical error at large time that prevents us to find the exact $\tau_{\exp}(\mathcal{O})$. Here, to estimate the slowest time scale of the Markov chain, we assume that the slowest mode in $C_{\mathcal{O}}(t)$ appears at a time $t_*$ where $C_{\mathcal{O}}(t_*) = 0.1$, and define an approximate exponential correlation time as

$$\tau'_{\exp}(\mathcal{O}) = \frac{t_*}{-\log C_{\mathcal{O}}(t_*)}. \tag{3.13}$$

Hereafter, we discuss the performance of the event-chain algorithm by using this approximate exponential correlation time $\tau'_{\exp}(\mathcal{O})$. A physical quantity $\mathcal{O}$ is carefully chosen so that its autocorrelation function is expected to have the slowest mode of the Markov chain. Otherwise, if we set $\mathcal{O}$ to a quantity that is not involved in the order of the system, the autocorrelation function $C_{\mathcal{O}}(t; t_w)$ decays fast at any finite temperature.

#### 3.2.1.1 Heisenberg ferromagnetic model in three dimensions

The first example we consider is the ferromagnetic Heisenberg model in three dimensions. The Hamiltonian is

$$H(\{\boldsymbol{S}_i\}) = -J \sum_{\langle i,j \rangle} \boldsymbol{S}_i \cdot \boldsymbol{S}_j. \tag{3.14}$$

The lattice on which spins reside is the simple cubic lattice with the periodic boundary conditions. The model shows a phase transition from the paramagnetic phase to the ferromagnetic phase at finite inverse temperature $\beta_{\mathrm{c}} = 0.6930(1)$ [40].

We focus here on the dynamical critical exponent $z$ of the ECMC algorithm. The exponent was estimated as $z = 1.96(6)$ by using Metropolis–Hastings algorithm with the autocorrelation function of the magnetization $\boldsymbol{m} = \frac{1}{N}\sum_i \boldsymbol{S}_i$ [13]. Here, we measure not only the autocorrelation function of $\boldsymbol{m}$, but also that of the energy and the magnetic susceptibility $\chi = \frac{1}{N}|\boldsymbol{m}|^2$.

The autocorrelation function of the magnetization obtained by the event-chain algorithm displays an oscillation, which is not observed in a stochastic process with detailed balance, see Fig. 3.1. Furthermore, the autocorrelation is independent of the system size while that in the heat-bath algorithm decays slower with increasing the system size. At

first sight, the dynamical critical exponent $z \simeq 0$ in the event-chain algorithm. However, the autocorrelation function of other physical quantities, the energy density and the magnetic susceptibility, in the event-chain algorithm undoubtedly depends on the system size. Why does not the autocorrelation function depend on the system size? In the event-chain algorithm, many spins (about $O(N)$ spins in the choice of $\ell = N\pi/10$) rotate with the same axis in each chain. The magnetization is not invariant under global rotation of spins, and consequently the orientation of the magnetization is largely changed in one Monte Carlo time step. These oscillating behavior in the autocorrelation function of the magnetization is also found in the trivial global rotation of all of spins [4]. The magnetization is not a physical quantity for the event-chain algorithm that has the slowest mode in its autocorrelation function obtained [4]. We thus focus on the autocorrelation function of the magnetic susceptibility $\chi$, which is invariant under global rotation, and shows a polynomial divergence at the critical temperature.

The approximate exponential correlation time $\tau'_{\mathrm{exp}}(\chi)$ measured in $C_\chi(t)$ increases polynomially with the system size, which implies the critical slowing down, see Fig. 3.1. The slope of the size dependence of the correlation time yields the dynamical critical exponent $z \simeq 1.2$. This value is significantly smaller than that of the local algorithms, $z = 1.96(6)$ by the Metropolis algorithm. The reduction of the dynamical critical ex-

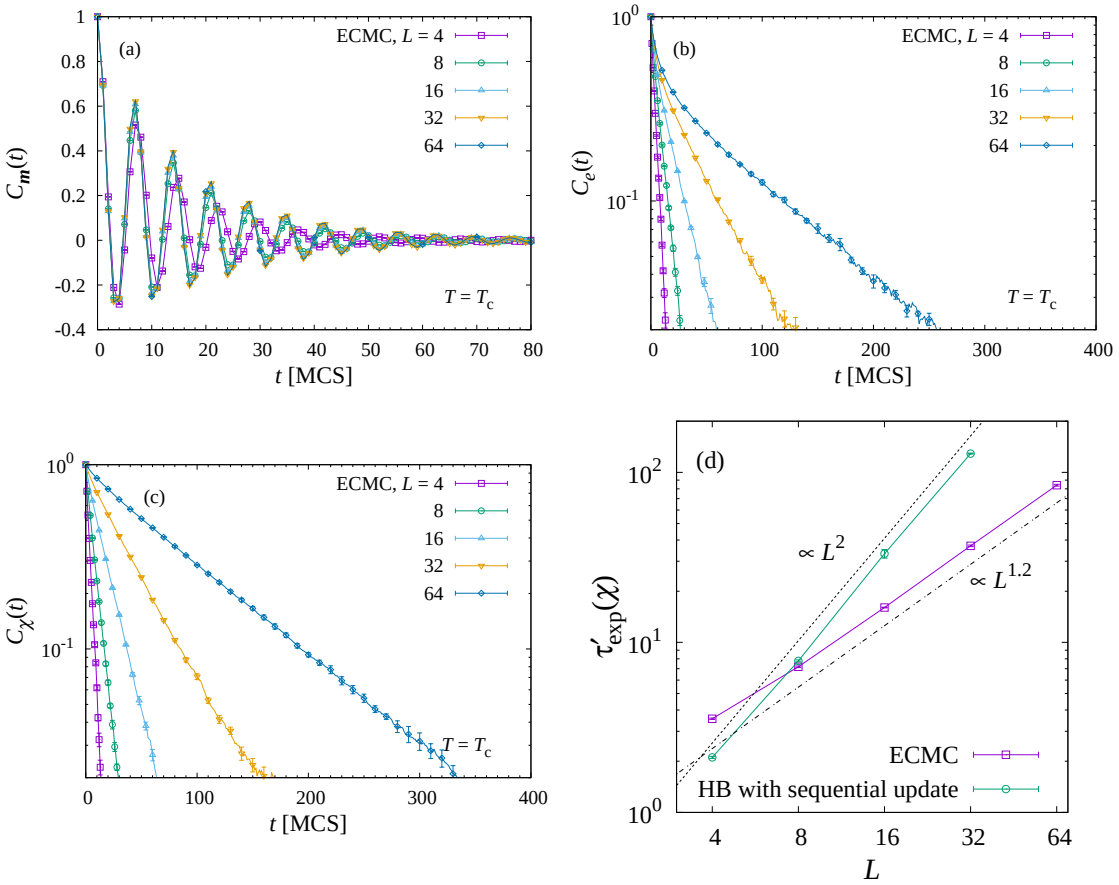


Fig. 3.1: (a–c) The autocorrelation function of the magnetization $\boldsymbol{m}$, the energy $e$, and the magnetic susceptibility $\chi$, respectively. (d) The correlation time of the magnetic susceptibility $\tau'_{\mathrm{exp}}(\chi)$ for both the event-chain algorithm (ECMC) and the heat-bath algorithm (HB) with sequential update.

ponent is not so dramatic as the Wolff cluster algorithm [40]. However, the event-chain algorithm realizes the reduction in a different manner from the cluster algorithm: Breaking the detailed balance condition. This is the first irreversible algorithm that can reduce the dynamical exponent of a finite-dimensional model with a finite-temperature phase transition. While the cluster algorithms do not work well in systems that do not have discrete (reflection) symmetry but has continuous symmetry, the event-chain algorithm is expected to be efficient for such systems.

3.2.1.2 Heisenberg antiferromagnetic model on a triangular lattice

Here we consider the Heisenberg antiferromagnetic model on a two-dimensional triangular lattice defined by the Hamiltonian

$$H\left(\{\boldsymbol{S}_i\}\right) = -J \sum_{\langle i,j \rangle} \boldsymbol{S}_i \cdot \boldsymbol{S}_j \quad (J < 0)\,. \tag{3.15}$$

Due to the geometrical frustration in each plaquette of the lattice, the ground state of the system is so-called 120° Néel state. In 1984, H. Kawamura and S. Miyashita [74] argued that this model has a Kosterlitz–Thouless-type phase transition at finite temperature driven by $Z_2$ vortices which are estimated to have a logarithmically diverging energy scale. The $Z_2$ vortex is a vortex formed by the chirality vector $\boldsymbol{\kappa}_i$ on each upward triangular plaquette of the lattice that is defined as

$$\boldsymbol{\kappa}_i = \frac{2}{3\sqrt{3}} \left(\boldsymbol{S}_{i,1} \times \boldsymbol{S}_{i,2} + \boldsymbol{S}_{i,2} \times \boldsymbol{S}_{i,3} + \boldsymbol{S}_{i,3} \times \boldsymbol{S}_{i,1}\right), \tag{3.16}$$

where $\boldsymbol{S}_{i,\alpha}$ ($\alpha = 1, 2, 3$) is the spin located at the left bottom site ($\alpha = 1$), the right bottom site ($\alpha = 2$), and the top site ($\alpha = 3$), respectively, see Fig. 3.2. A recent estimation of a possible phase transition temperature is $T_{\mathrm{v}}/J = 0.285(5)$ [38]. While the nature of the system in the low temperature region is still under debate, it is true that dynamics of $Z_2$ vortices at low temperature is very slow. We thus set $T/J = 0.25$ that is a sufficiently low temperature to demonstrate the performance of the event-chain algorithm. We choose $\mathcal{O}$ as the susceptibility of the chirality vector $\chi_{\mathrm{c}} = \frac{1}{N} \left|\sum_i \boldsymbol{\kappa}_i\right|^2$ that is invariant under global rotational transformation.

While the correlation time in the heat-bath algorithm at the temperature increases polynomially, that in the event-chain algorithm is almost constant for $L > 48$. If the

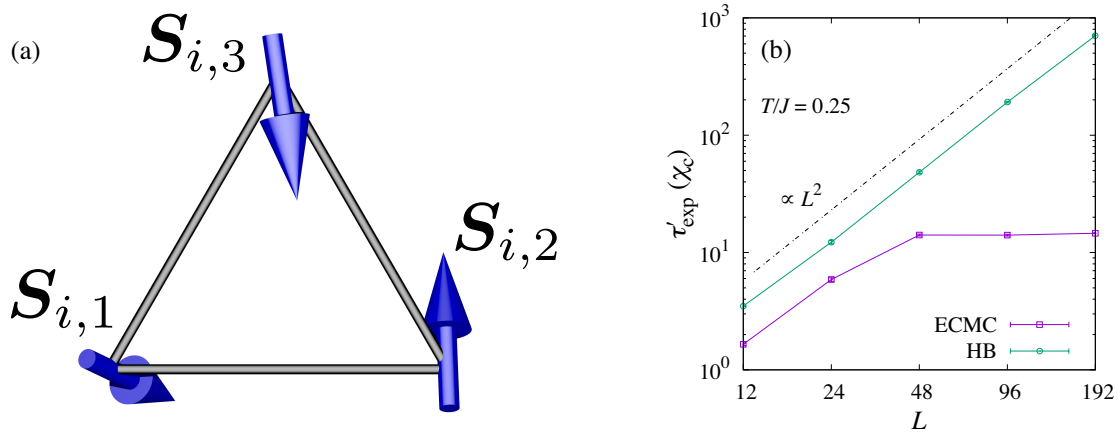


Fig. 3.2: (a) An elementary upward plaquette of a triangular lattice. (b) The correlation time $\chi_{\mathrm{c}}$ obtained by the heat-bath and the event-chain algorithm.

low temperature nature of the system is of the Kosterlitz–Thouless phase, the correlation time in the event-chain algorithm shows that the dynamical critical exponent is very small. A recent study [75] reports by using extreme-value statistics that the event-chain algorithm gives $z \to 0$ in the zero-temperature limit for the two-dimensional ferromagnetic $XY$ model although the mixing time is much longer than the equilibrium correlation time in the low temperature phase. The result in the two-dimensional antiferromagnetic Heisenberg model may be described by the same analysis. On the other hand, the correlation time in the event-chain algorithm can be also explained by assuming either that the low temperature phase is equivalent to the paramagnetic phase or that the susceptibility of the chiral vector is not involved in the low temperature phase. Anyway, the event-chain algorithm greatly enhances decorrelation of the correlation time of a physical quantity which increases rapidly in the heat-bath algorithm. We thus can conclude that the event-chain algorithm works efficiently in a frustrated antiferromagnet.

#### 3.2.1.3 Heisenberg spin glass model in three dimensions

As the last example, let us consider the Edwards–Anderson Heisenberg spin glass model on the three-dimensional simple cubic lattice. In the model, spins interact with each other through random coupling constants $\{J_{ij}\}$ drawn independently from a Gaussian distribution

$$P\left(J_{ij}\right) = \frac{1}{\sqrt{2\pi J^2}} \exp\left(-\frac{J_{ij}^2}{J^2}\right). \tag{3.17}$$

The Hamiltonian of the model depending on each realization $\{J_{ij}\}$ is

$$H_{\{J_{ij}\}}\left(\{\boldsymbol{S}_i\}\right) = -\sum_{\langle i,j\rangle} J_{ij} \boldsymbol{S}_i \cdot \boldsymbol{S}_j. \tag{3.18}$$

While the Heisenberg spin glass model is considered to have a spin glass phase transition at finite temperature $T_{\mathrm{SG}}$, another phase transition, a chiral glass transition, is claimed to occur at higher temperature $T_{\mathrm{CG}}$ associated to the $Z_2$ symmetry of the system [51, 76–79]. The chiral glass order parameter is defined as an average of an overlap between two replicas of the local chiral glass order

$$\chi_{i\mu} = \boldsymbol{S}_{i+\boldsymbol{e}_\mu} \cdot \left(\boldsymbol{S}_i \times \boldsymbol{S}_{i-\boldsymbol{e}_\mu}\right) \tag{3.19}$$

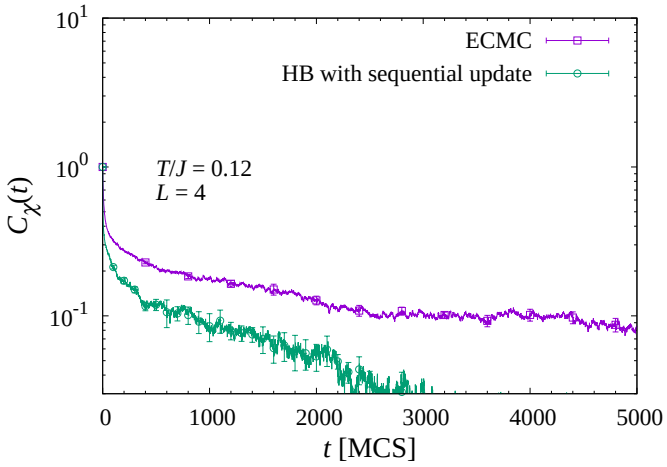


Fig. 3.3: The autocorrelation function of the chiral glass order $C_\chi\left(t\right)$ in the three-dimensional Heisenberg spin glass model.

over the lattice sites $i$ and the directions $\mu$, where $\boldsymbol{e}_\mu$ is a unit vector parallel to the $\mu$ direction ($\mu = x, y, z$). An opposite view on the model claims that the chiral and spin glass orders do not decouple, and $T_{\rm SG} = T_{\rm CG} = 0.129^{+0.003}_{-0.016}$ [80].

Here, we measure the autocorrelation function of the chiral glass order parameter averaged over 1024 realizations of random couplings. The temperature we consider is $T/J = 0.12$ which is expected to be lower than an estimated spin glass transition temperature no matter whether the two orders decouple or not.

The autocorrelation function in the event-chain algorithm decays slower than the heat-bath algorithm for $L = 4$ and 8, see Fig. 3.3. This clearly means that the event-chain algorithm is not efficient, and even worse than the conventional algorithm. We may understand this behavior by the discrete $Z_2$ nature of the chiral glass order: Global rotation, which is induced by the event-chain algorithm, does not change the sign of the chiral glass order, but global reflection does. Decorrelation of the chiral glass order is only achievable when configurations with the chiral glass order in both signs are equally sampled. The event-chain algorithm in the low temperature region of the spin glass model induces a global-rotation-like update while the heat-bath algorithm induces a random jump for each spin with finite displacements. Therefore the event-chain algorithm is not suitable for orders with discrete symmetry. Note that the event-chain algorithm is claimed to be efficient in the three-dimensional $XY$ model, and enhance decorrelation of the chiral glass order [81]. They compare the efficiency of the simple Metropolis algorithm and the event-chain algorithm, as the heat-bath algorithm is difficult to apply to $XY$ spin models. Their result implies that the event-chain algorithm works better than the Metropolis algorithm even though it is not so efficient for the spin glass model.

# 4

# Conclusion of Part I

In Part I, we discussed the Markov chain method in statistical physics. Any Markov chain that satisfies the irreducibility and the aperiodicity conditions converges to the unique stationary distribution. We can implement Markov chains without any a priori information about the system such as the normalization constant except its energy function. Markov chain Monte Carlo method is a powerful method in statistical physics that allows us to study statistical properties of an arbitrary finite-size system without any approximation in principle. However, due to correlations between samples and long correlation times in Markov chains, we sometimes obtain wrong results. In particular, at a phase transition point, the time scales diverge with the system size polynomially for continuous transitions, and exponentially for first-order transitions if we use the conventional local Monte Carlo algorithms. We have to simulate the system for a very long time in such cases. We also discussed some Markov chain Monte Carlo algorithms. Each algorithm has advantages compared to other algorithms, but does not work well for certain models.

In the last chapter, we presented the recently developed event-chain algorithm for particle and continuous spin systems. By introducing lifting variables, this algorithm can violate detailed balance with keeping global balance. We discussed a condition that the algorithm can maximally break detailed balance, especially for continuous spin systems. In the end of the chapter, we showed applications of the event-chain algorithm to some Heisenberg spin systems. The most surprising result there is the dynamical critical exponent $z$ of the algorithm for the three-dimensional ferromagnetic model: While conventional local Monte Carlo algorithms such as the Metropolis–Hastings and the heat-bath algorithm have $z \simeq 2$ scaling in the relaxation time, the event-chain algorithm has $z \simeq 1$ scaling. This is the first example of a reduction of the exponent by breaking detailed balance for a finite-dimensional system with a finite temperature phase transition. The event-chain algorithm is numerically proven to be efficient also for a frustrated system, an antiferromagnetic model on the two-dimensional triangular lattice. However, for a Heisenberg spin glass model in three-dimensions, the event-chain algorithm works worse than the heat-bath algorithm. A possible reason for its performance is the discrete nature of the order in the low temperature phase of the spin glass model.

The event-chain algorithm applied to the three-dimensional ferromagnetic Heisenberg model induces a rotation of $O(N)$ spins in a single chain if the chain length $\ell$ is sufficiently long. It is thus natural that the correlation time of the orientation of the magnetization vector is eliminated by the event-chain algorithm. However, the event-chain algorithm also reduces the correlation time, and the dynamical critical exponent of the length of the magnetization vector, the magnetic susceptibility, which seems a mode perpendicular to the orientation of the magnetization vector. This fact means that the dynamics of the event-chain algorithm is essentially different from the trivial global orientation. Some might expect that the reduction of the correlation time of the magnetic susceptibility in

the event-chain algorithm derives from the rejection-free nature of the algorithm. But, this is not true as the heat-bath algorithm, which is also rejection-free for the Heisenberg model, has the usual dynamic scaling $z \simeq 2$. Some also might think that breaking detailed balance produces the reduction of the dynamical critical exponent. This is not true either as any other algorithms breaking detailed balance are not reported to reduce the dynamical critical exponent. Thus, we can conclude that both of breaking detailed balance and a cluster update in the event-chain algorithm are essential for the reduction of the dynamical critical exponent. We need to understand a condition when the event-chain algorithm, and other algorithms breaking the detailed balance condition, can change the dynamics qualitatively which gives us a guiding principle to design new Monte Carlo algorithms.

The event-chain algorithm is built on the factorized Metropolis acceptance probability. This probability is a product of the conventional Metropolis acceptance probabilities, which can be calculated easily. We thus expect that the event-chain algorithm is applicable to any models straightforwardly as the conventional Metropolis algorithm. In particular, for statistical models with continuous degrees of freedom to which the heat-bath algorithm is not applicable (when the normalization constant cannot analytically integrable unlike the Heisenberg spin models as Eq. (2.17)), the event-chain algorithm should be a promising algorithm to investigate the systems in equilibrium efficiently. Continuous spin models defined by the Hamiltonian

$$H\left(\{\boldsymbol{S}_i\}\right) = \sum V_{ij}\left(\boldsymbol{S}_i \cdot \boldsymbol{S}_j\right), \tag{4.1}$$

where $V_{ij}$ is an arbitrary nonlinear function, are examples for which the heat-bath algorithm is not suitable due to non-trivial calculations of the normalization factor. They have various phases and phase transitions not observed when $V_{ij}$ is a linear function [82–85]. The conventional Metropolis algorithm suffers from rejection with high probability and the long correlation time at low temperature. The event-chain algorithm, on the other hand, is free from rejection, and thus it is expected to reduce the correlation time. However, whether a qualitative reduction of the correlation time in the models is realized by the event-chain algorithm is unclear. Another interesting examples for the event-chain algorithm are off-lattice particle models, especially structural glasses. In structural glasses, dynamics in molecular dynamics and Monte Carlo simulations with conventional algorithms is highly spatially heterogeneous at low temperature or high density [86, 87]. Immobile particles ("rattlers") are caged in neighboring particles. It takes a long time to move many particles cooperatively by conventional algorithms to destroy inactive regions in the system. The event-chain algorithm makes neighboring particles move cooperatively in one direction. The inactive regions in the structural glasses may possibly be destroyed efficiently by the algorithm. Extensive studies of the dynamics of the event-chain algorithm in complex systems including continuous spin systems with nonlinear interactions and structural glasses are necessary to understand the efficiency of the event-chain algorithm.

The major drawback of the event-chain algorithm is a difficulty of parallelization. A single cluster of displaced spins or particles formed in the event-chain algorithm extends over the whole system if the chain length $\ell$ is sufficiently long. Of course, such a large cluster is essential for the fast decorrelation by the algorithm, but that makes it difficult to find spatial regions which can be updated independently at the same time. A possible attempt to parallelize the algorithm for hard disks was reported in Ref. [88], where the system is decomposed into $O(L)$ parallel layers ($L$ is the linear dimension of the simulation box). Its maximal efficiency is thus $O(L)$ if the dynamics of the event-chain algorithm is not affected by the parallelization. Another parallelization strategy [89] is the checkerboard decomposition of the system as in Ref. [25] with a short chain length $\ell$. While the

maximal efficiency of this parallelization is $O(N)$, a short chain length largely decreases the efficiency of the algorithm, and the overall speedup is moderate [89].

A recent graphic processing unit (GPU) makes massive spatial parallelization of Monte Carlo simulations possible, and realizes $\sim 10^9$ updates per second both for particle and spin systems in two dimensions [22, 23, 25]. In particular, in the two-dimensional hard disk model, an $O(N)$ spatially parallelized simulation using a checkerboard decomposition with the conventional Metropolis algorithm [25] is 5 times faster than a serial Monte Carlo simulation with the event-chain algorithm in the sense of the correlation time measure in wall clock seconds. However, in higher dimensions, the parallelization efficiency is lower than that in two dimensions as the ratio of the regions in the system which can be updated at the same time decreases. Furthermore, the $O(N)$ spatial parallelization requires an advanced programming technique and fine tuning parameters in the program. On the other hand, the event-chain algorithm requires almost the same computational effort also in higher dimensions, and a straightforward implementation. We thus expect that the event-chain algorithm allows us to obtain more easily high-precision data of systems when the algorithm works well in the systems, i.e. the systems have continuous symmetry.

Our ultimate goal in designing Monte Carlo algorithms is to find a "good" cluster that can be used to enhance relaxation of each system. This requires us a deep understanding of physics of the system; its symmetry and orders. The Swendsen–Wang and Wolff algorithms, which have been regarded as the most successful cluster algorithms ever known, utilize discrete symmetry of systems to form clusters. That cluster in the algorithms is essentially important for very specific models (for example, as mentioned above, simple ferromagnetic models), but, for almost all models, it is not useful even if the models have discrete symmetry. The event-chain algorithm which utilizes continuous symmetry of systems also induces a large-cluster update in a different manner from the Swendsen–Wang and Wolff cluster algorithms. It thus can reduce slowing down in a different class of models. However, the event-chain algorithm is not so efficient for complex models like spin glasses, and obviously, models without continuous degrees of freedom. Any algorithm is not versatile, and we need a specific algorithm designed for each system that we would like to study.

Part II

# Phase transition in a three-dimensional uni-axial chiral magnet

# 5

# Introduction to uni-axial chiral magnets

Magnetic systems with competing (or frustrating) interactions and/or fields have lower symmetry in their spin space. Complicated spin structures, for example, spin ice, magnetic skyrmion, and spin liquid, emerge in such magnetic systems at low temperature. Phase transitions and phase diagrams of the systems with low symmetry are diverse, and may show unexpected properties. Uni-axial chiral magnets, in which the uni-axial antisymmetric Dzyaloshinskii–Moriya (DM) interaction [90–94] has an essential role in the spin structure, have recently attracted great interests to experimental and theoretical studies not only for its fundamental properties but also for applications [95–103]. They are experimentally realized in some materials, for example, $Cr_{1/3}NbS_2$ and $CsCuCl_3$, where their crystal structures are non-centrosymmetric [103]. In particular, $Cr_{1/3}NbS_2$ has been extensively studied, and shown to have a non-trivial spin structure, which is called the chiral soliton lattice (CSL) structure (see Fig. 5.1 for a schematic picture of the CSL structure), at low temperature in the presence of a magnetic field perpendicular to the helical axis [98–100, 102–104]. A phase transition between the CSL phase and the paramagnetic phase is experimentally observed through various physical quantities such as the magnetization [98, 100, 104], the magnetoresistance [99] and the ac susceptibility [102]. Two of the works [102, 104] reports that the phase transition qualitatively changes depending on the magnetic field.

The uni-axial chiral magnets have been theoretically studied by using a one-dimensional model with the ordinary exchange and the DM interactions with magnetic fields [90–92, 97, 105]. At zero temperature, the CSL structure indeed emerges in the model with a continuum approximation in the presence of the magnetic field, and a phase transition between the CSL and the paramagnetic phases occurs at finite magnetic field, see Fig. 5.1.

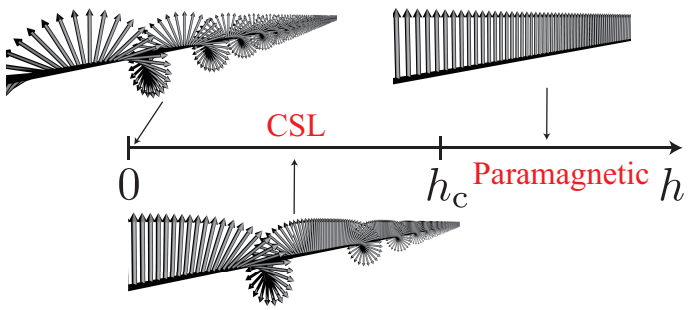


Fig. 5.1: Phase diagram of uni-axial chiral magnets at zero temperature. A phase transition between the CSL and the paramagnetic phases occurs at finite magnetic field $h_c$. Each arrow represents a spin.

A finite-temperature phase transition in three dimensions has been studied within mean-field approximations [106–110]. These works show that three types of phase transitions occur depending on the magnetic field; a continuous phase transition with classical critical exponents at weak and zero magnetic fields; a first-order phase transition with a latent heat; a "nucleation" type continuous phase transition [111] at strong magnetic field. In the mean-field level, the nucleation type continuous phase transition is described as a phase transition at which the average distance between two chiral solitons is infinity and only the uniform component of the magnetic susceptibility diverges while multiple wave vectors are necessary to characterize the ordered phase. In Refs. [107–110], the phase diagram and the detailed properties of phase transitions within the mean-field approximations are very detailed. Nevertheless, their mean-field approximation is essentially the same as the one-dimensional model because spins in the same plane perpendicular to the helical axis are assumed to have a very weak fluctuation. Thermal fluctuations at finite temperature appear in shrinkage of the length of the magnetization vector of each plane. Finite-dimensional effects on their mean-field approximation are not clear in their studies.

The phase diagram and a finite temperature phase transition of uni-axial chiral magnets in three dimensions is still unclear. Some attempts using renormalization group theory [112, 113] and a simple transformation of the Hamiltonian [114, 115] have been reported which consider the system without the magnetic field. However, their applicability is limited to the case. Monte Carlo simulations of the system with the magnetic field is thus expected to provide us detailed understandings of the phase transition. In particular, they allow us to access physical quantities such as the magnetization and the specific heat which can be measured in experiments and compare them obtained by experiments and simulations directly. Also, from the statistical-mechanical point of view, it is of significance to understand how the nucleation type phase transition appears in three-dimensions as its finite-dimensional counterpart has not been known to our knowledge.

In the following, we overview some results focusing on a phase transition at finite temperature and the phase diagram obtained by experiments on the uni-axial chiral magnets. Theoretical works on a one-dimensional continuum model of the chiral magnets at zero temperature and the mean-field theory are reviewed after that.

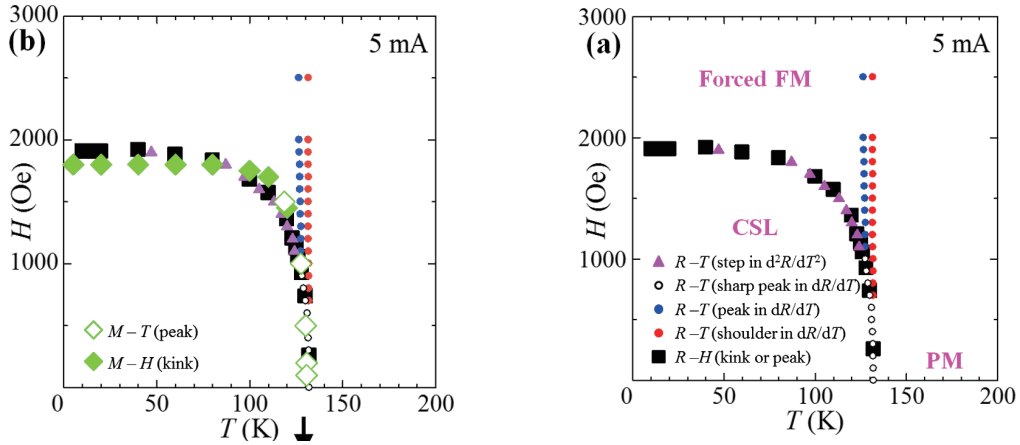


Fig. 5.2: Magnetic phase diagrams of $Cr_{1/3}NbS_2$ constructed by using the magnetization (left) and the magnetoresistance (right) [99].

## 5.1 Experiments on uni-axial chiral magnet

Most of the experiments studying finite-temperature properties of the uni-axial chiral magnet have used a single crystal of $Cr_{1/3}NbS_2$ [95, 96, 98–100, 102–104], whose crystal has a hexagonal structure. The CSL structure can be directly observed in the compound at finite temperature by transmission electron microscopy [98]. The magnetic phase diagram of the compounds has been constructed by using some physical quantities; the temperature and the magnetic field dependence of the magnetization [99, 100]; the magnetoresistance [99]; the ac susceptibility [102]. The phase diagrams obtained by each work qualitatively correspond to each other while the estimated value of the critical magnetic field at zero temperature is slightly different [99, 100, 102, 104].

In Ref. [99], they showed experimentally that the magnetoresistance is correlated to the period of the CSL structure, or equivalently, the number of the chiral solitons. At low temperature, the magnetoresistance monotonically decreases with increasing the magnetic field, which indicates that the number of chiral solitons also decreases. At slightly higher temperature, the magnetoresistance shows a positive change at phase transition point [99]. This suggests that the nature of the phase transition at finite magnetic field changes depending on temperature if the magnetoresistance still correlates to the number of chiral solitons at higher temperature. They also showed that no hysteresis is observed in their experiments. Another study [102] using the ac susceptibility claims that there exists a characteristic magnetic field that separates the CSL phase into two regions. A qualitative change in the ac susceptibility is observed depending on whether the magnetic field is above or below the characteristic value. In particular, they suggest a possibility of a first-order phase transition in the low magnetic field region. The order of a phase transition is also discussed in Ref. [104]. At low magnetic field, by measuring the entropy of spins, a first-order phase transition is claimed to occur at finite temperature. With increasing the magnetic field, the phase transition turns to be of second order.

While almost the same shape of the phase diagram of the uni-axial chiral magnet is obtained in many experimental works (see Fig. 5.2), detailed properties of the phase diagram of the uni-axial chiral magnet are still controversial: Is there a critical point at finite temperature and the magnetic field? Does a first-order phase transition occur in the low magnetic field region? A first-order phase transition discussed in [102, 104] clearly contradicts to the magnetization curve in which no hysteresis is seen [99]. If there exists a critical point in the phase diagram at which a first-order transition line terminates, criticality of the second-order phase transition at higher magnetic field is unclear.

## 5.2 Theory of the uni-axial chiral magnet

A one dimensional spin model of the uni-axial chiral magnet is defined by the Hamiltonian

$$H\left(\{\boldsymbol{S}_i\}\right) = -J\sum_i \boldsymbol{S}_i \cdot \boldsymbol{S}_{i+\boldsymbol{e}_y} - \boldsymbol{D}\cdot\sum_i \boldsymbol{S}_i \times \boldsymbol{S}_{i+\boldsymbol{e}_y} - \boldsymbol{h}\cdot\sum_i \boldsymbol{S}_i, \tag{5.1}$$

where, $\boldsymbol{S}_i$ is a classical Heisenberg spin. The second term corresponds to the Dzyaloshinskii–Moriya interaction, and $\boldsymbol{D} = D\boldsymbol{e}_y$. With this choice of $\boldsymbol{D}$, a helical structure along the one-dimensional lattice is induced. We take the magnetic field $\boldsymbol{h} = h\boldsymbol{e}_z \perp \boldsymbol{D}$. At zero temperature, all of spins are in the $x$-$z$ plane, and thus the Hamiltonian Eq. (5.1) can be written by parametrization $\boldsymbol{S}_i = (\sin\phi_i, 0, \cos\phi_i)$ as

$$H\left(\{\phi_i\}\right) = -J\sum_i \cos\left(\phi_{i+\boldsymbol{e}_y} - \phi_i\right) - D\sum_i \sin\left(\phi_{i+\boldsymbol{e}_y} - \phi_i\right) - h\sum_i \cos\phi_i \tag{5.2}$$

For very small $D/J$, the angle between two spins $|\phi_i - \phi_{i+\boldsymbol{e}_z}| \to 0$, and we obtain a continuum Hamiltonian which is exact in the limit $D/J \to 0$

$$H\left[\phi\left(y\right)\right] = J\int \mathrm{d}y \left[\frac{1}{2}\left(\frac{d\phi\left(y\right)}{dy}\right)^2 - \arctan\left(\frac{D}{J}\right)\frac{d\phi\left(y\right)}{dy} - \frac{h}{J}\cos\phi\left(y\right)\right] \tag{5.3}$$

A variational analysis gives a spatial profile $\phi\left(y\right) = 2\mathrm{am}\left(\sqrt{h}z/\sqrt{J}k\right)$, where $\mathrm{am}\left(x\right)$ is the Jacobi amplitude function, and $k$ is the elliptic modulus. This profile is periodic with the period $L = 2kK\left(k\right)\sqrt{J/h}$, where $K\left(k\right)$ is the complete elliptic integral of the first kind. The value of $k$ $(0 < k < 1)$ is again determined by a variational calculation of the energy per a period. With approaching $h_{\mathrm{c}} = \left(\pi \arctan\left(D/J\right)\right)^2 J/16$ from below, the elliptic modulus $k \to 1$, and the period $L$ diverges as $\sim -\log\left(h_{\mathrm{c}} - h\right)$. The magnetization $m$ and the uniform magnetic susceptibility $\chi$ also have singular behaviors, $m \sim 1 - \frac{1}{\log(h_{\mathrm{c}} - h)}$ [92, 97, 103] and $\chi \sim 1/\left(h_{\mathrm{c}} - h\right)\log\left(h_{\mathrm{c}} - h\right)$ [92], respectively. The spin structure (or, equivalently, $\phi\left(z\right)$) of the system with finite $h/J$ is indeed the CSL structure characterized by multiple wave vectors. The phase transition at zero temperature with the diverging period $L$ and uniform magnetic susceptibility $\chi$ is called the nucleation type continuous phase transition [111].

At finite temperature, phase transitions are studied within mean-field approximations for the continuum model [106, 107, 109], and for the discrete lattice model with the Hamiltonian Eq. (5.1) [108, 110]. They show that a tricritical point between the first-order and the ordinary continuous transition lines and a multicritical point between the first-order and the nucleation type continuous transition lines exist in the magnetic phase diagram, see Fig. 5.3. However, no theoretical study that systematically considers finite-dimensional effects on the system has not been known. Finite-dimensional fluctuations in the same perpendicular plane may completely blow out the mean-field picture. We thus need a theory of the uni-axial chiral magnet beyond the mean-field approximations to understand the nature of phase transitions and the phase diagram.

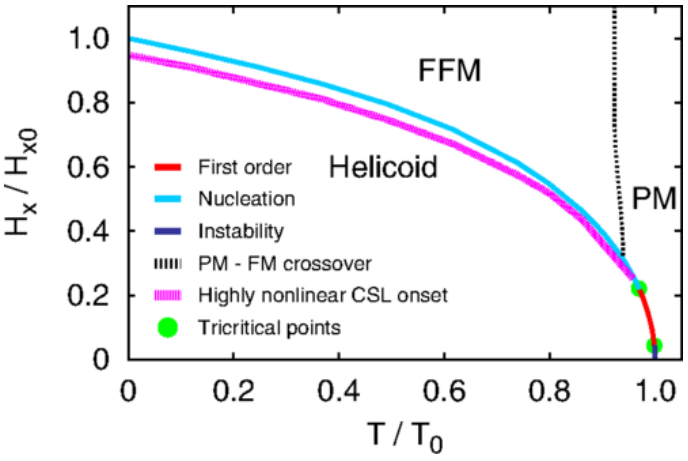


Fig. 5.3: Phase diagram of the uni-axial chiral magnetic model with a mean-field and a continuum approximations [109].

# 6 Simulation method

In this chapter, we introduce a classical Heisenberg spin model of a uni-axial chiral magnet, and physical quantities which are useful to study phase transitions in the model. Detailed parameters of the used algorithms are also presented.

## 6.1 Model

The model we consider here is a classical Heisenberg spin model with the ordinary exchange interaction, the Dzyaloshinskii–Moriya (DM) interaction, and a magnetic field. Its Hamiltonian is the following:

$$H\left(\{\boldsymbol{S}_i\}\right) = -J\sum_{\langle i,j\rangle}\boldsymbol{S}_i\cdot\boldsymbol{S}_j - \boldsymbol{D}\cdot\sum_i\left(\boldsymbol{S}_i\times\boldsymbol{S}_{i+\boldsymbol{e}_y}\right) - \boldsymbol{h}\cdot\sum_i\boldsymbol{S}_i, \tag{6.1}$$

where $\boldsymbol{S}_i$ is a classical Heisenberg spin model with $|\boldsymbol{S}_i| = 1$, $\boldsymbol{D} = D\boldsymbol{e}_y$ is the DM vector, and $\boldsymbol{h} = h\boldsymbol{e}_z$ is a magnetic field perpendicular to the DM vector $\boldsymbol{D}$. The bracket $\langle\cdot,\cdot\rangle$ represents a pair of neighboring sites of the lattice. The lattice on which spins reside is a simple cubic lattice where the linear length of the $y$ direction (parallel to the DM vector) is $\alpha$ times as long as the $x$ and $z$ directions. We denote the linear length of the $x$ and the $z$ directions of the lattice as $L$ and the total number of sites is $N = \alpha L^3$. We set $\alpha = 8$ through this work. Periodic boundary conditions are used on the $x$ and the $z$ directions and a free boundary condition on the $y$ direction. The linear length of the system in our simulations ranges from $L = 2$ (the total number of spins $N = 2\times16\times2$) to $L = 64$ ($N = 64\times512\times64$).

The ground state structure parallel to $\boldsymbol{D}$ of the system without the magnetic field can be easily obtained by local optimization of each local energy if we assume that $L_y\to\infty$, or $L_y$ is commensurate to the structure. Since the Hamiltonian is invariant under a rotation with an axis $\boldsymbol{e}_y$ and a translation, it is natural to suppose that a spin at $i$-th site $\boldsymbol{S}_i \parallel \boldsymbol{e}_z$. We can easily minimize the local energy of $\boldsymbol{S}_i$ and $\boldsymbol{S}_{i+\boldsymbol{e}_y}$, $-JS_{i+\boldsymbol{e}_y,z} - DS_{i+\boldsymbol{e}_y,x}$, by parametrizing $\boldsymbol{S}_{i+\boldsymbol{e}_y} = (\sin\theta, 0, \cos\theta)$, and find the optimal angle $\theta_{\mathrm{GS}} = \arctan\left(D/J\right)$. The ground state of the system with $h = 0$ is characterized by one single wave vector

$$\boldsymbol{q}_{\mathrm{chiral}} = \arctan\left(\frac{D}{J}\right)\boldsymbol{e}_y. \tag{6.2}$$

By transforming spins $\boldsymbol{S}_{\boldsymbol{r}}\to\boldsymbol{\sigma}_{\boldsymbol{r}} = R_{\boldsymbol{e}_y}\left(-\theta_{\mathrm{GS}}r_y\right)\boldsymbol{S}_{\boldsymbol{r}}$, where $\boldsymbol{r} = (r_x, r_y, r_z)$ is a position of a lattice site and $R_{\boldsymbol{e}_y}(\theta)$ is a rotation matrix around $\boldsymbol{e}_y$ for an angle $\theta$, the Hamiltonian is converted to

$$H'\left(\{\boldsymbol{\sigma}_i\}\right) = -J\sum_{\langle i,j\rangle_\perp}\boldsymbol{\sigma}_i\cdot\boldsymbol{\sigma}_j - \sum_i\boldsymbol{\sigma}_i\cdot A\boldsymbol{\sigma}_{i+\boldsymbol{e}_y}, \tag{6.3}$$

where

$$A = \begin{pmatrix} \sqrt{J^2 + D^2} & & \\ & J & \\ & & \sqrt{J^2 + D^2} \end{pmatrix}, \tag{6.4}$$

and the summation in the first term runs over the neighboring pairs of two lattice sites which are in the same $x$-$z$ plane [114, 115]. This Hamiltonian (6.3) for a finite value of $D$ has the same symmetry with the $XY$ model, and therefore, the original system is expected to belong to the same universality class of the three-dimensional ferromagnetic $XY$ model [114].

In the presence of the magnetic field $\boldsymbol{h} = h\boldsymbol{e}_z$ perpendicular to the DM vector, the structure of the ground state is modulated depending on $h$, and cannot be determined locally. For $0 < h < h_{\mathrm{c}}\,(< \infty)$, the chiral soliton lattice structure emerges, and all spins are parallel to the magnetic field for $h > h_{\mathrm{c}}$. The precise value of $h_{\mathrm{c}}$ is unclear for arbitrary value of $D/J$ while those for $D/J \ll 1$ with a continuum approximation [90–92, 97, 103, 105] and for $D/J = 1$ are calculated [116]. In the CSL state at zero temperature, there are more than one local length scales such as the distance between two chiral solitons and the length scale of one chiral soliton, and hence, multiple wave vectors are expected to be required to characterize the CSL structure.

## 6.2 Physical quantities

In this section, we define several physical quantities to study phase transitions in our system.

Any periodic spin structure is identified by the wave-vector-dependent magnetization

$$\boldsymbol{m}(\boldsymbol{q}) = \frac{1}{N}\sum_j \boldsymbol{S}_j \exp\left(-i\boldsymbol{q}\cdot\boldsymbol{r}_j\right), \tag{6.5}$$

where $\boldsymbol{q}$ is a three-component wave vector. The wave-vector-dependent susceptibility associated with $\boldsymbol{m}(\boldsymbol{q})$ is defined as

$$\chi(\boldsymbol{q}) = \beta N\left[\langle \boldsymbol{m}(\boldsymbol{q})\,\boldsymbol{m}(-\boldsymbol{q})\rangle - \langle \boldsymbol{m}(\boldsymbol{q})\rangle\langle \boldsymbol{m}(-\boldsymbol{q})\rangle\right], \tag{6.6}$$

where $\beta$ is inverse temperature and the bracket $\langle\cdots\rangle$ denotes the thermal average at $\beta$. Note that $\chi(\boldsymbol{q})$ is proportional to a Fourier component of the spin correlation function

$$C(\boldsymbol{r}) = \frac{1}{N}\sum_i \left(\langle \boldsymbol{S}_i\cdot\boldsymbol{S}_{i+\boldsymbol{r}}\rangle - \langle \boldsymbol{S}_i\rangle\cdot\langle \boldsymbol{S}_{i+\boldsymbol{r}}\rangle\right) \tag{6.7}$$

in the thermodynamic limit $N \to \infty$, or with periodic boundary conditions. We especially focus on the susceptibility with a wave vector $\boldsymbol{q}$ parallel to the DM vector $\boldsymbol{D}$ that we denote as $\chi^{\parallel}(q)$ $(q = |\boldsymbol{q}|)$. While an order parameter of the ground state of the system without the magnetic field is $\boldsymbol{m}(\boldsymbol{q} = \boldsymbol{q}_{\mathrm{chiral}})$, which $\boldsymbol{m}(\boldsymbol{q})$'s characterize phase transitions of the system at finite temperature is not obvious even if the magnetic field is absent. We thus compute the wave-vector dependence of $\chi^{\parallel}(q)$ to find the wave vectors $\boldsymbol{q}_0$ at which $\chi^{\parallel}(q_0)$ gives maximum values. By using $\chi(\boldsymbol{q})$, the wave-vector-dependent finite-size correlation length can be measured as

$$\xi_L(\boldsymbol{q}) = \frac{1}{2\sin\left(|\boldsymbol{q}_{\min}|/2\right)}\sqrt{\frac{\chi(\boldsymbol{q})}{\chi(\boldsymbol{q}+\boldsymbol{q}_{\min})} - 1}, \tag{6.8}$$

where $\boldsymbol{q}_{\min}$ is the minimum wave vector parallel to $\boldsymbol{q}$ [117]. We denote the finite-size correlation length depending on a wave vector $\boldsymbol{q}$ parallel to $\boldsymbol{D}$ as $\xi_L^{\parallel}(q)$ as the susceptibility, where $\boldsymbol{q}_{\min}$ in Eq. (6.8) is set to $\boldsymbol{q}_{\min} = (0, 2\pi/\alpha L, 0)$.

We also measure a distribution function of the energy density $e$

$$P(e) = \left\langle \delta\left(e - \frac{1}{N} H(\{\boldsymbol{S}_i\})\right)\right\rangle. \tag{6.9}$$

This distribution function shows a double-peak structure near a first-order phase transition point. The specific heat $c$ is computed as the variance of the energy distribution

$$c = \beta^2 N \left(\left\langle \left(\frac{H}{N}\right)^2 \right\rangle - \left\langle \frac{H}{N} \right\rangle^2\right). \tag{6.10}$$

The peak value of the specific heat $c_*(L)$ diverges with the system size as $L^d$ asymptotically, where $d$ is the spatial dimension of the system, if the system has a first-order phase transition [118]. On the other hand, for second-order phase transitions, $c_*(L)$ is involved in the nontrivial critical exponents of the specific heat $\alpha$ and the correlation length $\nu$. If $\alpha > 0$ (the specific heat diverges at a phase transition point), $c_*(L)$ scales as $c_*(L) \sim L^{\frac{\alpha}{\nu}}$, while $c_*(L) \simeq c_*(\infty) - sL^{\frac{\alpha}{\nu}}$ if $\alpha < 0$ and the specific heat has a cusp singularity at a phase transition point in the thermodynamic limit [40].

## 6.3 Algorithms

To equilibrate the system with more than $10^6$ Heisenberg spins, we use the event-chain, the heat-bath, the over-relaxation, and the exchange Monte Carlo algorithms together. In this section we explain the detail parameters of the algorithms used in our simulations.

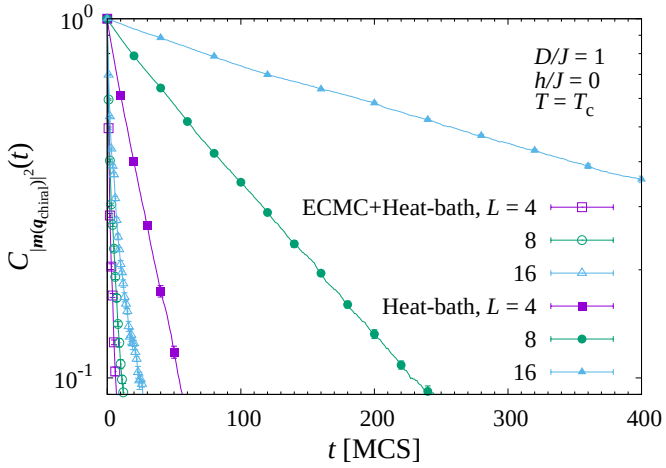


Fig. 6.1: The autocorrelation function $C_{|\boldsymbol{m}(\boldsymbol{q}_{\rm chiral})|^2}(t)$ of the square of the wave-vector-dependent magnetization $|\boldsymbol{m}(\boldsymbol{q}_{\rm chiral})|^2$ of the system without magnetic fields. Open and filled symbols represent $C_{|\boldsymbol{m}(\boldsymbol{q}_{\rm chiral})|^2}(t)$ with and without the ECMC algorithm, respectively. The temperature is set to the critical temperature $T_{\rm x}$ estimated in the next chapter.

| | $h/J=0$ | | $h/J=0.1$ | | $h/J=0.2$ | | $h/J=0.3$ | |
|---|---|---|---|---|---|---|---|---|
| $L$ | $T_{\min}/J$ | $T_{\max}/J$ | $T_{\min}/J$ | $T_{\max}/J$ | $T_{\min}/J$ | $T_{\max}/J$ | $T_{\min}/J$ | $T_{\max}/J$ |
| 2 | 1.5 | 1.9 | | | | | | |
| 4 | 1.55 | 1.8 | 1.5 | 1.9 | 1.45 | 1.85 | 1.4 | 1.5 |
| 8 | 1.62 | 1.77 | 1.5 | 1.9 | 1.45 | 1.85 | 1.4 | 1.5 |
| 16 | 1.65 | 1.75 | 1.62 | 1.72 | 1.55 | 1.65 | 1.4 | 1.5 |
| 32 | 1.66 | 1.71 | 1.60 | 1.7 | 1.55 | 1.65 | 1.43 | 1.47 |
| 48 | | | | | | | 1.443871 | 1.446129 |
| 64 | 1.67 | 1.7 | 1.65 | 1.67 | 1.59 | 1.61 | 1.44 | 1.45 |
| | | | | | | | 1.443871 | 1.446129 |

Table 6.1: The lowest and highest temperatures in our Monte Carlo simulations. For $L = 64$ and $h/J = 0.3$, simulations are performed for two temperature sets.

### 6.3.1 Event-chain and heat-bath algorithm

The Hamiltonian of our model except the magnetic field is invariant under a rotation with $\boldsymbol{v} = \boldsymbol{e}_y$. We thus can apply the event-chain algorithm with the update scheme of the lifting variables $(i, \boldsymbol{v}) \to (j, \boldsymbol{v})$, which maximally breaks detailed balance, if the rotation axis $\boldsymbol{v} = \boldsymbol{e}_y$, see Section 3.2. However, the event-chain algorithm for Heisenberg spins with a single rotational axis $\boldsymbol{v} = \boldsymbol{e}_y$ is not irreducible, i.e. the ergodicity condition is not satisfied. We may apply the algorithm with another rotation axis using an update $(i, \boldsymbol{v}) \to (i, -\boldsymbol{v})$, which means a moving spin goes back to the opposite direction when a move is rejected. Here, instead, we combine the heat-bath algorithm to restore the ergodicity condition.

A parameter of the event-chain algorithm $\ell$ which determines the length of each chain, or the total rotation angles in a chain, is set to $N\pi/10$. The heat-bath update is carried out sequentially every 100 event chains.

As discussed in Chapter 3, the event-chain algorithm is expected to greatly reduce the correlation time of several models. Indeed, the autocorrelation function of $|\boldsymbol{m}(\boldsymbol{q}_{\text{chiral}})|^2$ at the phase transition temperature (described below) decreases much faster if the event-chain and the heat-bath algorithms are combined, see Fig. 6.1. Here, one unit Monte Carlo time step is defined as $N$ spin updates in both cases.

### 6.3.2 Over-relaxation algorithm

To further enhance decorrelation, we use the over-relaxation algorithm together with the event-chain and the heat-bath algorithms. The over-relaxation algorithm updates spins as

$$\boldsymbol{S}_i \to -\boldsymbol{S}_i + \frac{2\boldsymbol{S}_i \cdot \boldsymbol{H}_i}{|\boldsymbol{H}_i|^2}\boldsymbol{H}_i, \tag{6.11}$$

where $\boldsymbol{H}_i$ is the local field made by interacting spins and external fields. Although this algorithm is deterministic and never changes the energy of the system, it greatly helps decorrelation when combined with algorithms that sample from the Gibbs distribution. In our simulations, 5 over-relaxation sweeps are performed for every event chain.

### 6.3.3 Exchange Monte Carlo method

We use the exchange Monte Carlo algorithm for 32 replicas with different temperatures. Two neighboring temperatures are exchanged with the Metropolis-type exchange proba-

bility, Eq. (2.28). Temperatures lie at regular intervals between the lowest and highest temperatures, which are denoted as $T_{\min}$ and $T_{\max}$, respectively. To keep the exchange probability high, we change the temperature range in our simulations depending on the system size and the magnetic field, see Tab. 6.1.

# 7

# Phase transitions and Ordering structures of the uni-axial chiral magnet

In this chapter, we present results of our Monte Carlo simulations of the system with and without the magnetic field. Without the magnetic field, we show by finite-size scaling analyses of the correlation length and the magnetic susceptibility that the system belongs to the three-dimensional $XY$ model as discussed in Section 6.1 and predicted by theories. In the presence of the magnetic field perpendicular to the axis of the helical structure, we find that the nature of a phase transition depends on the magnetic field, and at least one critical point exists in the magnetic phase diagram. We also show results for dynamics of the system consistent with the results obtained by our Monte Carlo simulations.

## 7.1 Universality class of the system without magnetic fields

In this section we discuss a phase transition of the system without the magnetic field and its universality class. Below a phase transition temperature $T_{\rm c}$, the system is expected to have a long-range helical order characterized by a single wave vector, and the wave-vector-dependent magnetic susceptibility associated with the wave vector diverges polynomially with the system size $L$ at $T_{\rm c}$ (the susceptibility scales as $L^d$ even below a phase transition temperature in finite systems if the Hamiltonian has symmetry that is spontaneously broken with the phase transition). The wave-vector-dependent magnetic susceptibility has two clear peaks at $\boldsymbol{q}_{\rm chiral}$ at low temperature independent of the system size, see Fig. 7.1. This means that the wave vector $\boldsymbol{q}_{\rm chiral}$, which characterizes the ground-state spin structure, also characterizes the structure of the system around $T_{\rm c}$, and $\boldsymbol{m}\left(\boldsymbol{q}_{\rm chiral}\right)$ is an order parameter of the phase transition. The wave-vector-dependent correlation length $\xi_L^{\parallel}\left(q_{\rm chiral}\right)$ divided by $\alpha L$ increases with decreasing temperature for all system sizes, and each pair of $\xi_L^{\parallel}\left(q_{\rm chiral}\right)/\alpha L$ and $\xi_{2L}^{\parallel}\left(q_{\rm chiral}\right)/2\alpha L$ has a clear intersection at $T/J \simeq 1.68$ (Fig. 7.2 (a)). We assume a finite-size scaling form for the correlation length

$$\frac{\xi_L^{\parallel}\left(q_{\rm chiral}\right)}{\alpha L} = F\left[\left(\frac{T-T_{\rm c}}{J}\right)(\alpha L)^{1/\nu}\right], \tag{7.1}$$

where the transition temperature $T_{\rm c}$ and the critical exponent of the correlation length $\nu$ are estimated so that data for different system sizes fall into a universal curve $F$ with each other. We use a recently proposed method based on Bayesian inference [119, 120] to estimate $T_{\rm c}$ and $\nu$. Four sets of the data that consist of three successive system sizes $L_{\rm min}$, $2L_{\rm min}$ and $4L_{\rm min}$ are used for the analysis. The finite-size scaling form works very well, especially for the data set with $L_{\rm min} = 16$ which include the largest system size $L = 64$ in our simulations, see Fig. 7.2 (b). The estimated values of the critical temperature and the exponent for $L_{\rm min} = 16$ are $T_{\rm c} = 1.68672(4)$ and $\nu_\xi = 0.676(3)$, respectively. We should notice that, with increasing $L_{\rm min}$, the estimated value of the exponent decreases,

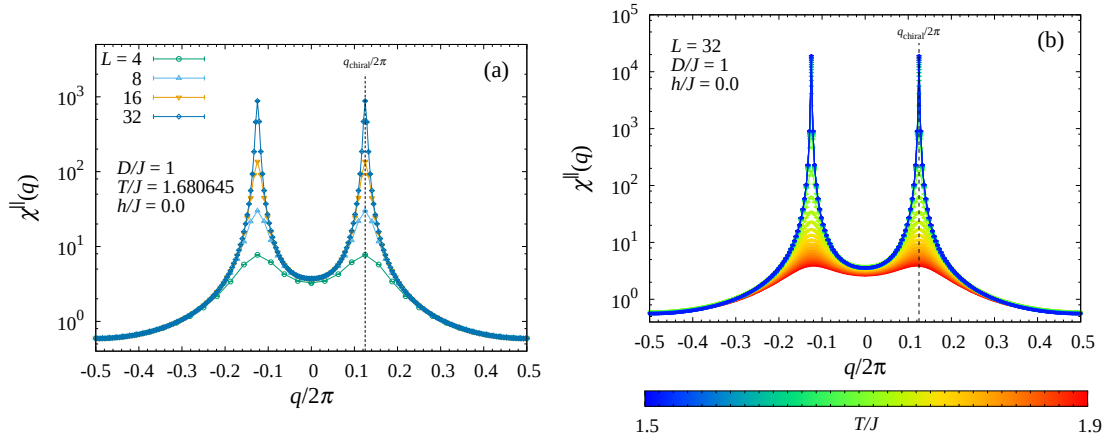


Fig. 7.1: Wave-number dependence of $\chi^{\parallel}(q)$ of the three-dimensional uni-axial chiral magnetic model without magnetic fields (a) for various system sizes at $T/J = 1.680645$, which is close to the critical temperature, and (b) with $L = 32$ at various temperatures above and below the critical temperature.

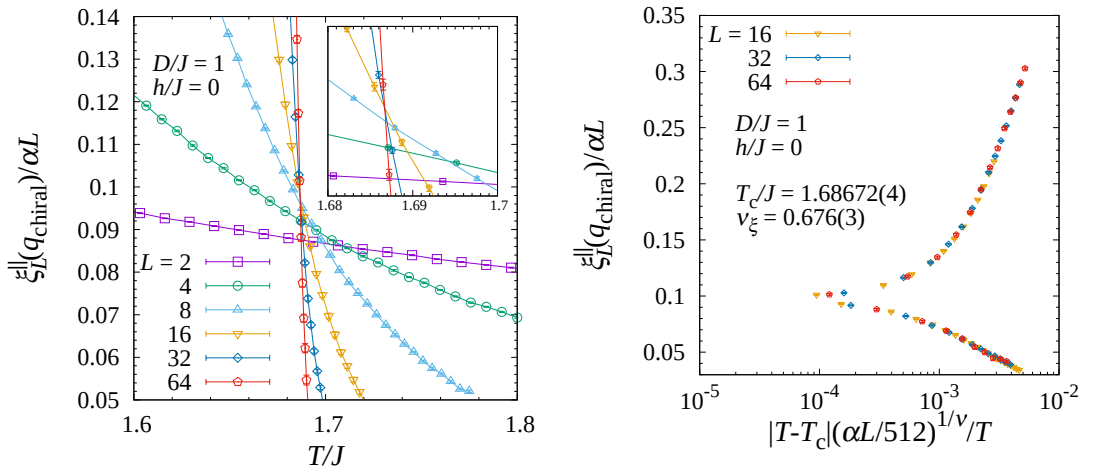


Fig. 7.2: (a) Temperature dependence of the finite-size correlation length $\xi^{\parallel}(q_{\rm chiral})$ divided by $\alpha L$ of the system without magnetic fields. Inset shows an enlarged view around the critical temperature. (b) A finite-size scaling plot of the finite-size correlation length $\xi_L^{\parallel}(q_{\rm chiral})$ divided by $\alpha L$ of the system without magnetic fields. The smallest system size of this FSS plot is $L_{\rm min} = 16$. The critical temperature $T_{\rm c}$ and the critical exponent $\nu$ are estimated as $T_{\rm c}/J = 1.68672(4)$ and $\nu = 0.676(3)$, respectively.

and the value of $\nu_\xi$ is definitely lower than that of the three-dimensional ferromagnetic Heisenberg model $\nu = 0.704(6)$ [40], and comparable to that of the three-dimensional ferromagnetic $XY$ model $\nu = 0.67155(27)$ [121] (see Tab. 7.1). We also analyze the magnetic susceptibility $\chi^{\parallel}(q_{\rm chiral})$ for the same data sets by assuming a finite-size scaling form

$$\chi^{\parallel}(q_{\rm chiral}) = (\alpha L)^{\gamma/\nu_\chi}\, G\left[\left(\frac{T-T_{\rm c}}{J}\right)(\alpha L)^{1/\nu_\chi}\right]. \tag{7.2}$$

Here, the value of the transition temperature $T_{\rm c}$ obtained in the finite-size scaling analysis of $\xi_L^{\parallel}(q_{\rm chiral})/\alpha L$ is used for this analysis. The critical exponent of the correlation length $\nu_\chi$ slightly decreases with increasing $L_{\rm min}$ as that estimated using $\chi^{\parallel}(q_{\rm chiral})$. The resul-

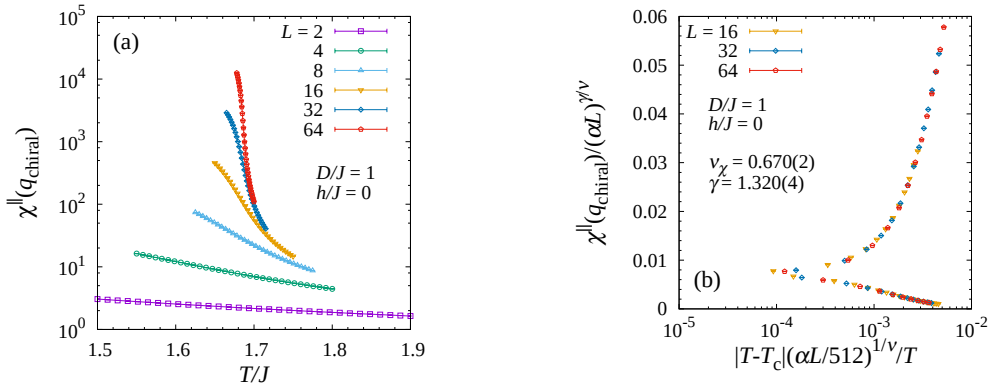


Fig. 7.3: (a) Temperature dependence of the wave-vector-dependent magnetic susceptibility $\chi^{\parallel}(q_{\mathrm{chiral}})$ of the system without magnetic fields. (b) A finite-size scaling plot of $\chi^{\parallel}(q_{\mathrm{chiral}})$ of the system without magnetic fields. The value of the critical temperature $T_{\mathrm{c}}$ estimated by the finite-size scaling analysis of the finite-size correlation length ratio $\xi_L^{\parallel}(q_{\mathrm{chiral}})/\alpha L$ is used.

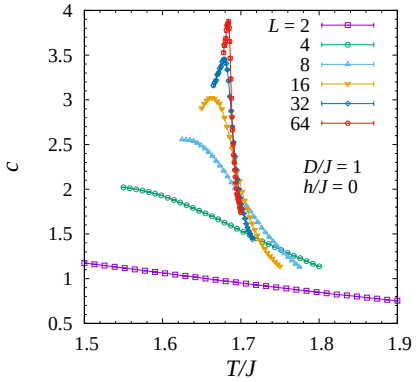


Fig. 7.4: Temperature dependence of the specific heat $c$ of the system without magnetic fields.

tant value of the critical exponent $\nu_\chi$ for $L_{\mathrm{min}} = 16$ is again in good agreement with that of the $XY$ model, and that of another exponent $\gamma = 1.320(4)$ is also close to $\gamma = 1.3177(5)$ in the $XY$ model, see Fig. 7.3.

For models that belong to the ferromagnetic $XY$ universality class, we find that the critical exponent of the specific heat $\alpha$ is negative by using the hyperscaling relation $d\nu = 2 - \alpha$. Indeed, the specific heat of the ferromagnetic $XY$ model has a finite value even at the critical temperature $T_{\mathrm{c}}$, but it has a cusp singularity [122]. The specific heat $c$ of our model develops a singularity with increasing $L$ (Fig. 7.4), but its peak value does not seem to diverge in the thermodynamic limit, see Fig. 7.5 (b). This is, again, consistent with the ferromagnetic $XY$ universality class. We therefore conclude that the system without magnetic fields undergoes a phase transition from a paramagnetic phase to a uni-axial chiral magnetic phase as temperature decreases with the critical exponents of the three-dimensional $XY$ model, as predicted in Refs. [112–115].

| $L_{\min}$ | $T_{\rm c}/J$ | $\nu_\xi$ | $\nu_\chi$ | $\gamma$ |
|---|---|---|---|---|
| 2 | 1.688(1) | 0.72(2) | 0.711(5) | 1.45(1) |
| 4 | 1.6871(2) | 0.696(5) | 0.682(2) | 1.314(4) |
| 8 | 1.68683(5) | 0.681(4) | 0.671(1) | 1.303(3) |
| 16 | 1.68672(4) | 0.676(3) | 0.670(2) | 1.320(4) |

Table 7.1: The estimated values of the critical temperature and the critical exponents of the correlation length and the susceptibility by finite-size scaling analyses. The values of the critical temperature $T_{\rm c}$ and the exponent of the correlation length denoted as $\nu_\xi$ are estimated using the data of the finite-size correlation length $\xi_L^{\parallel}\left(q_{\rm chiral}\right)/\alpha L$. Using the estimated value of $T_{\rm c}$, the value of critical exponents of the susceptibility $\gamma$ and that of the correlation length denoted as $\nu_\chi$ are estimated by FSS analyses of the susceptibility $\chi^{\parallel}\left(q_{\rm chiral}\right)$.

## 7.2 Phase transition under a magnetic field perpendicular to the DM vector

In the presence of the magnetic field, the system has no continuous symmetry in the Heisenberg spin space, and hence, it is natural to expect that a possible phase transition between the paramagnetic phase and the chiral-soliton lattice phase belongs to another universality class, or is of first order. We present in this section our Monte Carlo results of the system with the magnetic field $h/J = 0.1$, 0.2, and 0.3.

For weak magnetic fields $h/J = 0.1$ and 0.2, the specific heat shows a temperature dependence similar to that of the system without the magnetic field; it seems to have a cusp singularity at finite temperature, see Fig. 7.6 (a). When the specific heat has a cusp with a phase transition, a peak value of the specific heat $c_*\left(L\right)$ scales with the system size $L$ as [40]

$$c_*\left(L\right) = c_*\left(\infty\right) - sL^{\alpha/\nu}, \tag{7.3}$$

where $s$ is a constant. The peak value $c_*\left(L\right)$ for both $h/J = 0.2$ and 0.3 has almost the same value as for $h/J = 0$, and we expect that the system with $h/J = 0.2$ and 0.3 has a critical exponent ratio $\alpha/\nu$ that is very akin to, or the same as that of the three-dimensional $XY$ model. On the other hand, at $h/J = 0.3$, the specific heat has a very large peak at finite temperature $T/J \simeq 1.445$, and $c_*\left(L\right)$ shows a strong divergence with the system size as well as or stronger than $L^3$ (Fig. 7.5 (b)). We see a similar size dependence for a peak value of the uniform magnetic susceptibility $\chi\left(\boldsymbol{0}\right)$, Fig. 7.5 (a). These indicate that at least one critical point exists between $h/J = 0.2$ and 0.3, and the nature of the phase transition is qualitatively changed depending on the magnetic field.

At low temperature, the $q$-dependence of the magnetic susceptibility $\chi^{\parallel}\left(q\right)$ has multiple peaks independent of the magnetic field $h > 0$ while that has only two peaks at high temperature as the case without the magnetic field, see Fig. 7.7. These peaks are located at integer multiples of the wave number of the first peak (which we denote as $q_0$), and they grow with the system size. These observations indicate that a periodic spin structure, e.g. a chiral soliton lattice, emerges in the low-temperature region. Local length scales in the spin structure are represented by the inverse of the wave numbers at which $\chi^{\parallel}\left(q\right)$ has a peak, and especially the distance between two chiral solitons $2\pi q_0^{-1}$. The wave number $q_0$ decreases with the magnetic field $h$ (see Fig. 7.8), which means the distance increases with $h$, and, for example, at $h/J = 0.3$, the distance is $2\pi q_0^{-1} \simeq 10$ lattice spacings.

The value of $q_0$, which determines the wave-vector-dependent magnetization $\boldsymbol{m}\left(q_0\right)$

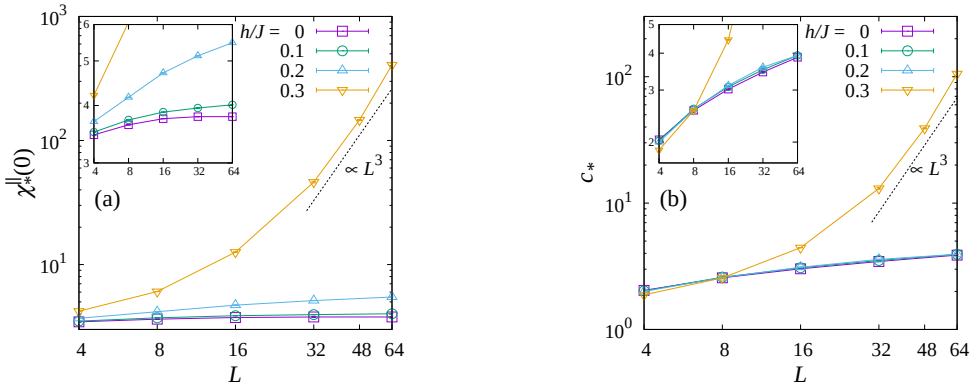


Fig. 7.5: System-size dependence of the peak value of the susceptibility $\chi^{\parallel}_{*}(0)$ (a) and the specific heat $c_*$ (b) of the system with a magnetic field perpendicular to the DM vector $h/J = 0$, 0.1, 0.2, and 0.3. The black dotted lines are proportional to $L^3$. The insets show enlarged views.

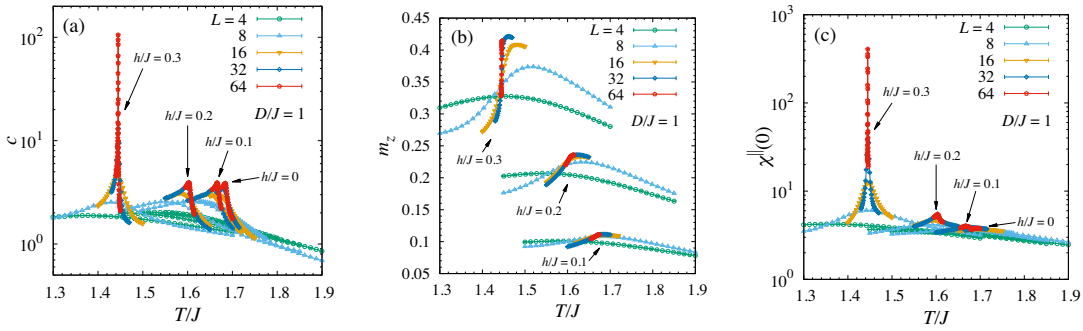


Fig. 7.6: Temperature dependence of (a) the specific heat $c$, (b) the magnetization $m_z$ parallel to the magnetic field $\boldsymbol{h}$, and (c) the uniform magnetic susceptibility $\chi$ of the system with and without the magnetic field.

characterizing the spin structure of the system with each system size, depends on temperature and even on the system size. The peak locations in the thermodynamic limit are expected to have real numbers, and deviate from those in finite discrete lattices, which have a finite number of wave vectors. It is difficult to identify the precise value of $q_0$ in the thermodynamic limit by numerical simulations of finite size systems and the order parameter of the phase transition. We may calculate the finite-size correlation length $\xi^{\parallel}_{L}(q_0)$ using Eq. (6.8) for each system size and each temperature as the case without magnetic fields. However, due to the change of $q_0$ depending on temperature, $\xi^{\parallel}_{L}(q_0)$ shows a sudden change with decreasing temperature, and hence $\xi^{\parallel}_{L}(q_0)$ is not an appropriate physical quantity to calculate a transition temperature and a critical exponent of the system with the magnetic field.

Instead of $\boldsymbol{m}(\boldsymbol{q})$, we calculate an overlap between spin configurations of two independent replicas as a possible order parameter. The overlap between two replicas $q = \sum_i \boldsymbol{S}_i^{(1)} \cdot \boldsymbol{S}_i^{(2)}/N$ [*1] is well known as the spin glass order parameter [123], and is also useful for detecting ordinary periodic orders such as ferromagnetic and antiferromagnetic orders.

[*1] The overlap is usually denoted as $q$ in the literature of the spin glass theory. It is a confusing notation here as wave vectors are represented as $\boldsymbol{q}$. Nevertheless we use this usual notation because it is easy to understand which one is represented as $q$ in each sentence.

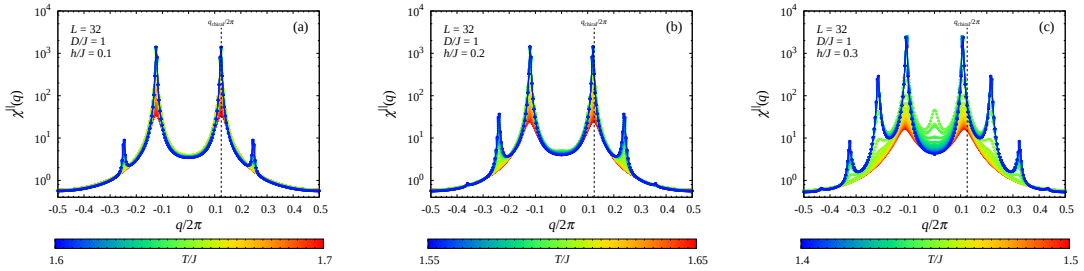


Fig. 7.7: Wave-number dependence of $\chi^{\parallel}(q)$ of the system with $L = 32$ near the estimated phase transition temperature. The values of the magnetic fields perpendicular to the DM vector are (a) $h/J = 0.1$, (b) $h/J = 0.2$, and (c) $h/J = 0.3$.

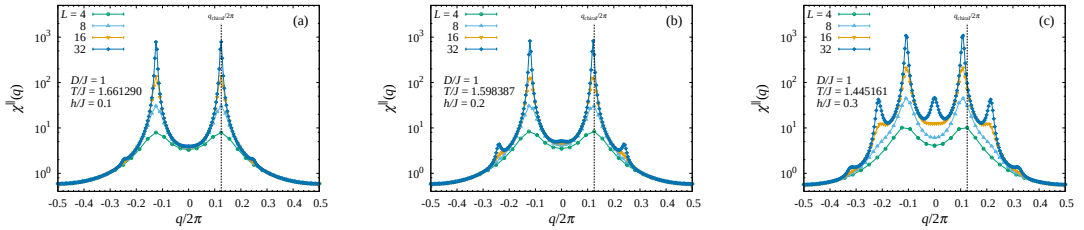


Fig. 7.8: Wave-number dependence of $\chi^{\parallel}(q)$ of the system for various system sizes in the low-temperature region. The values of the magnetic fields perpendicular to the DM vector are (a) $h/J = 0.1$, (b) $h/J = 0.2$, and (c) $h/J = 0.3$.

The susceptibility and the correlation length associated with the overlap can be defined in the same manner as $\boldsymbol{m}(\boldsymbol{q})$. We should notice that the relevant wave vector in the overlap is zero no matter which wave vectors the intrinsic order has. As a matter of fact, for our system without the magnetic field, the correlation length defined using the overlap (which we denote $\xi_L$ in the following) divided by $\alpha L$ has an intersection, and allows us to get almost the same transition temperature $T_c$ and the critical exponent $\nu$ estimated in the previous section by assuming the same finite-size scaling form Eq. (7.1), see Fig. 7.9. At $h/J = 0.2$, we also find a clear intersection in the correlation length ratio at finite temperature, and, again with the finite-size scaling form Eq. (7.1), we obtain a transition temperature $T_c/J = 1.6061(2)$ and the critical exponent of the correlation

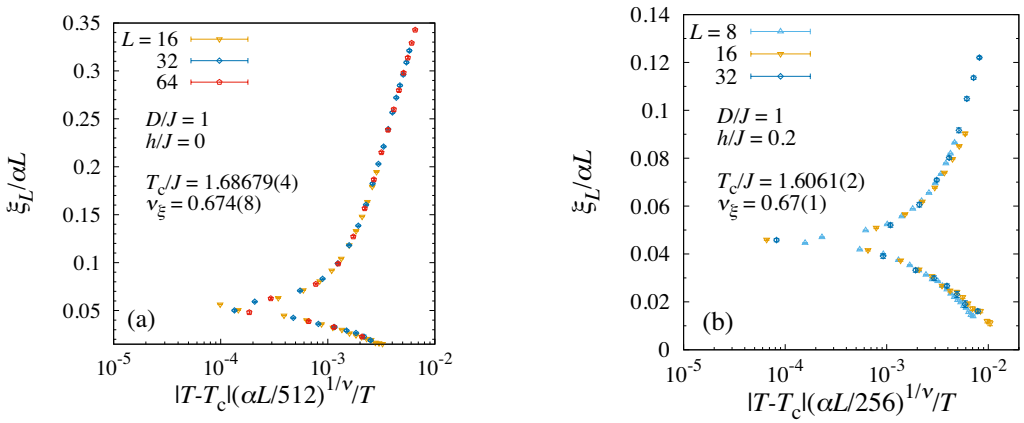


Fig. 7.9: A finite-size scaling plot of the finite-size correlation length of the spin overlap divided by $\alpha L$. The magnetic field $h/J = 0$ (a) and 0.2 (b).

length $\nu = 0.67(1)$. We thus expect that the system with the magnetic field $h/J = 0.2$ still belongs to the three-dimensional $XY$ model although it no longer has any continuous symmetry due to the magnetic field. This weak magnetic field may be an irrelevant field to the helical order $\boldsymbol{m}(\boldsymbol{q}_{\text{chiral}})$, and a single wave vector $\boldsymbol{q}_0$ characterizes the phase transition, which means that only $\chi(\pm\boldsymbol{q}_0)$ diverges at $T_c$, while multiple wave vectors are required in the chiral soliton lattice phase to characterize its structure. Renormalization group analysis would possibly help us to understand this phase transition.

At $h/J = 0.3$, as discussed above, a possible scenario of the phase transition of the system is largely changed from the case with $h/J = 0.2$. As for $h/J = 0$ and 0.2, the correlation length defined using the spin overlap divided by $\alpha L$ has a intersection at around a temperature $T_*/J \simeq 1.446$ where the specific heat has a large peak. The simple finite-size scaling form Eq. (7.1), however, does not work well even though we consider the corrections to scaling: Any combination of data for three system sizes does not fall into a universal curve. One of the possible reasons is that finite size effects in the system are extraordinarily large that the leading corrections-to-scaling term does not work. If so, we have to simulate larger system sizes to obtain the transition temperature and the critical exponents. Another possible reason is that the finite-size scaling form Eq. (7.1) may be not appropriate for this case. In Ref. [92], I. E. Dzyaloshinskii predicts theoretically by using a one-dimensional continuum model of a uni-axial chiral magnet with the magnetic field that the specific heat diverges toward a phase transition temperature $T_*$ from below as

$$c \propto \frac{1}{(T_* - T)\log^2(T_* - T)} \tag{7.4}$$

while no critical divergence is seen above $T_*$. This suggests that $\alpha \leq 0$ and $\alpha' = 1$. Then, if assume the hyperscaling relation $d\nu = 2 - \alpha$ for each side of the phase transition temperature, we obtain different values for $\nu$ and $\nu'$. If the theory by Dzyaloshinskii holds for our model, another finite-size scaling form is necessary.

After all, what is the order of the phase transition in the system with $h/J = 0.3$? For first-order phase transitions, because of finite jumps in physical quantities such as the energy density, their susceptibilities (for example, the specific heat for the energy density) diverge as $L^d$ with the system size, where $d$ is the spatial dimension of the system, and

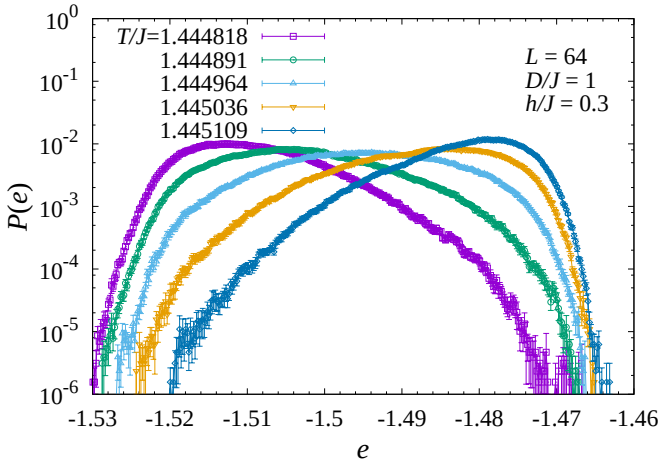


Fig. 7.10: The energy-density distribution function $P(e)$ of the system with the magnetic field $h/J = 0.3$. The system size $L = 64$ is the largest size in our simulations and the temperatures are close to the transition temperature.

the finite-size peak location $T_*(L)$ depends on the system size as

$$T_*(L) = T_*(\infty) + O\left(L^{-d}\right). \tag{7.5}$$

The "critical" exponents are $\alpha = 1$, $\gamma = 1$, and $\nu = 1/d$ with vanishing asymptotic amplitude of the correlation length [118]. Also, at around the phase transition temperature, the probability distributions of the physical quantities have double-peak structures. Our data show that the system size dependences of the specific heat and the uniform magnetic susceptibility are marginally compatible with $L^d$ for $L \geq 32$. However, the Dzyaloshinskii's theory predicts the same scaling for the peak value of the specific heat $\sim L^{\frac{\alpha}{\nu}} = L^3$ if we again assume the hyperscaling relation, and hence, we cannot distinguish them by the system size dependence of the peak value of the specific heat. On the other hand, the peak location $T_*(L)$ does not follow the finite size scaling of first-order phase transitions Eq. (7.5) up to $L = 32$. Furthermore, the probability distribution of the energy density does not have a double-peak structure although the system size dependence of the specific heat reaches to $L^d$, see Fig. 7.10. Therefore, it is natural to conclude within our simulations that the system with $h/J = 0.3$ has a continuous phase transition with nontrivial critical exponents. Further calculations for much larger systems and detailed data analyses using, for example, the multiple reweighting method [124], are necessary to conclude decisively the nature of the phase transition.

A recent mean-field study [110] claims that the system with the same parameters, $D/J = 1$ and $h/J = 0.3$, shows a first-order phase transition. As in the conventional naive mean-field approximation, they assume spin fluctuations in the same $x$-$z$ planes are small enough. However, in our Monte Carlo simulations, fluctuations in the same $x$-$z$ planes are unexpectedly strong. Each $x$-$z$ plane looks like a coexistence state mixed of spins parallel and antiparallel to the magnetic field, see Fig. 7.11. These large fluctuations should be essential in the phase transition at the magnetic field, and thus the naive mean-field approximation may not be applicable. Further analysis is required to characterize the large fluctuations.

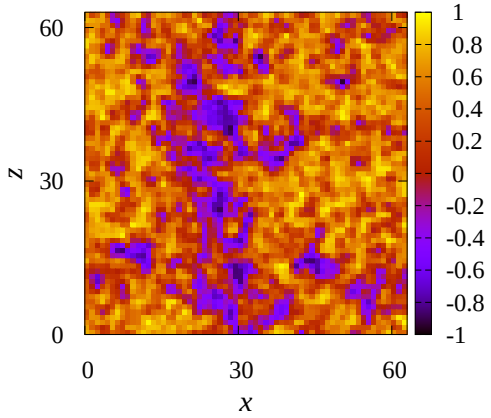


Fig. 7.11: A typical snapshot of an $x$-$z$ plane of the system at the estimated transition temperature with $h/J = 0.3$. The color represents the $z$ component of each spin, which is the component parallel to the magnetic field.

## 7.3 Dynamics

In this section, We study Monte Carlo dynamics of the system, especially the correlation time $\tau_{\mathcal{O}}$ of a physical quantity $\mathcal{O}$ at the phase transition temperature by using only the heat-bath algorithm. The value of the dynamical critical exponent $z$, which is estimated in finite systems as $\tau_{\mathcal{O}} \propto L^z$, implies an order of its phase transition: The correlation time diverges with the system size algebraically for continuous phase transitions ($z$ is finite), and exponentially for first-order phase transitions. We set temperature to the estimated phase transition temperature by the finite-size scaling analysis for $h/J = 0$ and 0.2, and the peak location of the specific heat for $h/J = 0.3$. We choose the energy density $e$ and the uniform magnetization $\boldsymbol{m}(\mathbf{0})$ to measure the autocorrelation Eq. (2.8). As in the Section 3.2.1, we use the exponential correlation time. Here, however, to compute the approximate exponential correlation time $\tau'_{\mathrm{exp}}(\mathcal{O}) = -t_*/\log C_{\mathcal{O}}(t_*)$, $t_*$ is defined as the time where $C_{\mathcal{O}}(t_*) = 0.01$.

The exponential correlation time of the energy density increases algebraically with the system size $L$ up to the system sizes, see Fig. 7.12. The exponent $z \simeq 2.0$ for $h/J = 0.2$, and $z \simeq 2.7$ for $h/J = 0.3$. The exponential correlation time of the uniform magnetization also shows an algebraic increase for both magnetic fields, but its exponent is smaller than that of the energy density. The autocorrelation of the energy density thus has a slower mode than the autocorrelation function of the magnetization. The algebraic increase implies a continuous phase transition occurs for both magnetic fields. The exponent $z \simeq 2.0$ for $h/J = 0.2$ is consistent with the three-dimensional $XY$ model [14]. At $h/J = 0.3$, the exponent is significantly larger than that for $h/J = 0.2$. That indicates the nature of the phase transition at $h/J = 0.3$ is different from that at $h/J = 0.2$. If we assume a lower bound of the dynamical critical exponent $z \geq \gamma/\nu$ [17, 18] holds in the system, the critical exponent $\nu$ for $h/J = 0.3$ is possibly much smaller than that in the three-dimensional $XY$ universality class.

When a first-order phase transition occurs with a latent heat, the exponential correlation time of the energy density diverges exponentially with the system size. Our result shows that the correlation at $h/J = 0.3$ does not increase exponentially, but algebraically up to $L = 16$. While a larger system size should be studied to conclude it, the increase of the correlation time is consistent with the result of equilibrium Monte Carlo simulations presented in the previous section.

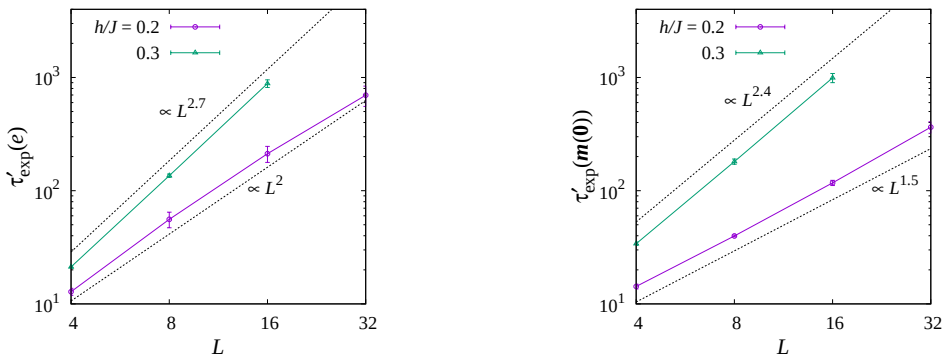


Fig. 7.12: The exponential correlation time of the energy density $e$ (a) and the uniform magnetization $\boldsymbol{m}(\mathbf{0})$ (b) in the system with $h/J = 0.2$ and 0.3.

## 7.4 Phase diagram

A phase diagram of the system obtained by our simulations is presented in Fig. 7.13, where we denote the paramagnetic phase and the CSL phase as "P" and "CSL", respectively. The filled square at $h/J = 0$ is estimated by the FSS analysis in Section 7.1, and the other squares and circles are estimated by the peak temperature of $\chi(\mathbf{0})$ at $h/J = 0.1$, 0.2 and 0.3 for $L = 64$ and at $h/J = 0.35$ for $L = 16$. The phase transitions at the transition temperatures represented by the squares belongs the three-dimensional $XY$ universality class as discussed in the previous section. On the other hand, at $h/J = 0.3$, a completely different criticality is observed at the transition temperature shown in the phase diagram as a circle. Almost the same system-size dependence of the peak values of the specific heat and the uniform magnetic susceptibility is seen at $h/J = 0.35$ up to $L = 16$. The zero-temperature critical magnetic field $h_c/J$, the diamond in the phase diagram, can be computed as a magnetic field where the energy cost of one chiral soliton in a one-dimensional model is zero. The value should coincide with a mean-field result, and thus $h_c/J = 0.50884(3)$ [116]. According to our results presented in the previous section, there should be at least one (multi-)critical point between $h/J = 0.2$ and 0.3 in the phase diagram which divides the phase boundary. At the time when our work on the uni-axial chiral magnet [5] was completed, even an existence of at least one critical point was not established in the model of the uni-axial chiral magnets in three dimensions. However, after the completion of our work [5], the two mean-field studies [109, 110] report that two critical points divide the phase boundary between the paramagnetic and the CSL phases. From this viewpoint, our data are obviously not enough to claim the existence of one single critical point in the phase diagram. To testify the mean-field results, physical quantities exactly on the phase boundary should be studied. If a first-order phase transition line lies

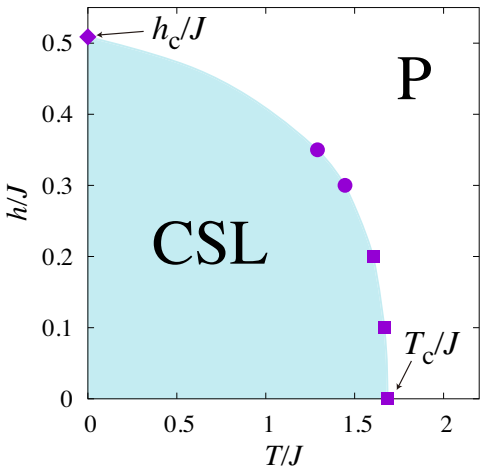


Fig. 7.13: A possible magnetic phase diagram of the system. In the phase diagram, "CSL" and "P" denote the chiral soliton lattice phase and paramagnetic phase, respectively. The filled squares and circles are estimated transition temperatures by our numerical simulations, and the diamond is the critical magnetic field at zero temperature $h_c/J$ (see text for the precise value). The three-dimensional $XY$ criticality appears at the filled squares while another critical behavior with strong divergences in the specific heat and the uniform magnetic susceptibility is observed at the filled circles.

on the phase boundary, the Binder parameter of the energy or the magnetization should show a negative diverging behavior on the line while it has a finite value at a continuous phase transition point. Much larger-scale Monte Carlo simulations are required to conclude the structure of the phase diagram. Nevertheless, in the following, we assume the single critical point $(T_{\rm d}/J, h_{\rm d}/J)$ on the phase boundary for further discussions.

The phase boundary $h_{\partial{\rm CSL}}(T)$ between the paramagnetic phase and the CSL phase has a finite slope, which are also observed in experimental works of a uni-axial chiral magnet [99, 100, 102]. When the free-energy density of the system in the thermodynamic limit is differentiable at a point on the phase boundary $(T_0, h_{\partial{\rm CSL}}(T_0))$, which means that the phase transition is continuous, the finite slope of the phase boundary yields a general relation

$$\Delta\chi\Delta c - T\left(\Delta\omega\right)^2 = 0, \tag{7.6}$$

where $\omega$ and $\chi$ are the temperature derivative and the magnetic-field derivative of the magnetization parallel to the field, and

$$\Delta X = X_{\rm CSL} - X_{\rm P} \tag{7.7}$$

for any $X \in \{c, \chi, \omega\}$ is a difference of $X$ in the limit from inside the CSL phase and from the paramagnetic phase to $(T_0, h_{\partial{\rm CSL}}(T_0))$, respectively. The system in the magnetic field with $0 < h < h_{\rm d}$ belongs to the universality class of the three-dimensional ferromagnetic $XY$ model as discussed above, then the specific heat is continuous on the phase boundary, $\Delta c = 0$. In this system for a fixed $h < h_{\rm d}$, the uniform susceptibility has a finite value, $\Delta\chi < \infty$. Therefore, Eq. (7.6) requires $\Delta\omega = 0$, meaning that the magnetization parallel to the magnetic field is smooth at the transition temperature. This is consistent with our results for the magnetization, where it does not show any jump or singular behavior at around the transition temperature, Fig. 7.6.

For $h > h_{\rm d}$, on the other hand, the specific heat diverges at a phase transition temperature. The difference $\Delta c$ is infinitely large unless the critical amplitude ratio is accidentally 1 with the same critical exponent above and below the critical temperature which may unlikely occur in finite dimensions. The relation of Eq. (7.6) allows typically two cases:

(i) $\Delta\chi \lesssim \Delta c^{-1}$ and $\Delta\omega$ is finite, or
(ii) $\Delta\chi \gtrsim \Delta c^{-1}$ and $\Delta\omega$ is infinitely large.

Our result on the divergence of $\chi(\mathbf{0})$ indicates the latter case unless, again, the critical amplitudes and the exponents above and below the critical point are identical. Technically speaking, $\chi$ is not equivalent to $\chi(\mathbf{0})$, but, in our system, a singular part in $\chi(\mathbf{0})$ originates from $\chi$. The specific heat $c$ divided by the susceptibility $\chi(\mathbf{0})$ seems to have a finite value even in the thermodynamic limit in our simulations. This implies that the exponent of the divergence of $\chi(\mathbf{0})$ coincides with that of the specific heat. Furthermore, the temperature dependence of the magnetization is also described by the same singularity at least either above or below the critical temperature. Thus, the critical singularity of the specific heat appears in other observables unrelated to the critical nature through the relation of Eq. (7.6), while in a conventional system where $\chi$ is an order-parameter susceptibility, the relation yields the scaling relation $\alpha + 2\beta + \gamma = 2$ among the critical indices.

# 8

# Conclusion of Part II

In Part II, we have numerically studied the classical Heisenberg spin model of a uni-axial chiral magnet in three dimensions by equilibrium Monte Carlo simulations. The event-chain algorithm introduced in the previous part works very efficiently in the model, and it allows us to equilibrate the system with more than $10^6$ Heisenberg spins. We particularly focused on its finite-temperature phase transition between the chiral-soliton-lattice phase (the helical phase) and the paramagnetic phase with and without a magnetic field perpendicular to the axis of the helical structure. Without the magnetic field, detailed finite-size scaling analyses revealed that the system undergoes a continuous phase transition with critical exponents of the three-dimensional ferromagnetic $XY$ model. This is consistent with some theoretical studies using a renormalization group calculation [112, 113] and a simple transformation of the Hamiltonian [114, 115].

In the presence of the magnetic field, the nature of the phase transition strongly depends on $h/J$ while the low temperature phase is common. The chiral soliton lattice structure is characterized by multiple wave vectors, and order parameters which are involved in the phase transition are unclear. To avoid this problem, we used the spin overlap, also known as the spin glass order parameter, to compute the finite-size correlation length. We found that the system with $h/J = 0.1$ and 0.2 shows a phase transition which is very similar to that in the absence of the magnetic field: A cusp singularity in the specific heat, and no divergence in the uniform magnetic susceptibility. A finite-size scaling analysis yields the critical exponent $\nu$, which is consistent with the three-dimensional ferromagnetic $XY$ model. At $h/J = 0.3$, we observed a completely different phase transition with strong divergences of the peak values with a scaling $\sim L^3$ both in the specific heat and the uniform magnetic susceptibility. The correlation length ratio indeed has an intersection, but the conventional finite-size scaling ansatz for it fails to find the critical exponent.

Our results clearly demonstrate that at least one critical point exists in the region where $0.2 < h/J < 0.3$ in the phase diagram of the system while we cannot rule out a possibility that there exist two or more critical points in the region. The critical nature at low magnetic field, whose exponent is consistent with that of the three-dimensional $XY$ model, is surprising in the sense of the symmetry of the Hamiltonian. A renormalization group study would support our results; if a renormalization-group flow goes into the zero-field critical point $T_c/J$, the same critical nature as the zero-field case should appear at finite but low magnetic field. The phase transition at higher magnetic field remains unclear. While the peak value of the specific heat diverges as $\sim L^3$, which is usually seen in a first-order phase transition, a double-peak structure in the distribution function of the energy density is not observed. Also, at the phase transition temperature, the equilibrium relaxation time seems to diverge polynomially, which suggests a continuous nature of the transition. We thus found no evidence of a first-order phase transition in any other physical quantities at $h/J = 0.3$.

The assumption that a spin fluctuation is small enough to be ignored in the naive mean-field theories is usually incorrect in systems in low dimensions. The upper critical spatial dimension $d_{\mathrm{U}}$ below which a mean-field theory breaks down is determined by self-consistency of the theory, or the Ginzburg criterion [125]. For the continuous phase transition with the classical critical exponents such as ferromagnetic phase transitions, the upper critical dimension $d_{\mathrm{U}} = 4$. Between $d_{\mathrm{U}}$ and the lower critical dimension $d_{\mathrm{L}}$, a phase transition with nontrivial critical exponents occurs at finite temperature, and it disappears below $d_{\mathrm{L}}$. The validity of mean-field theories can be tested by itself for continuous phase transitions. On the other hand, for first-order phase transitions, a mean-field theory is always self-consistent if they remain in finite dimensions within the theory as fluctuations are weak at first-order phase transition points. However, a first-order phase transition in the mean-field theory is sometimes replaced by a second-order phase transition in finite-dimensional models such as the three-state ferromagnetic Potts model [126]. Non-perturbative finite-dimensional effects may eliminate first-order phase transitions in the mean-field theory, and the theory cannot yield its validity by itself. In our model of uniaxial chiral magnets, the recent mean-field study [110], in which a spin fluctuation in the same plane perpendicular to the helical structure is assumed to be very small, claims that a first-order phase transition with a latent heat occurs at the parameters, $D/J = 1$ and $h/J = 0.3$. As discussed above, the mean-field theory should always be self-consistent even if the theory gives an incorrect result. A large fluctuation ignored in the mean-field can completely change the mean-field picture of the phase transition while the order of the phase transition might not be changed even if the fluctuation exists. A snapshot of a plane perpendicular to the helical axis Fig. 7.11 in our simulations indeed indicates a large fluctuation ignored in the theory. This suggests that the phase transition is driven by the fluctuation in each plane rather than the mean-field scenario. Whether the fluctuation plays an important role at the phase transition temperature should be extensively studied by numerical simulations through an appropriate physical quantity which captures the fluctuation [*1].

This work considers phase transitions in a system with a field that is not conjugate to an order of the system without the field. A field conjugate to an order of a system explicitly breaks symmetry in its Hamiltonian, and generally suppresses a phase transition in the original system without the field. On the other hand, a weak field which is not conjugate to an order of a system but breaks continuous symmetry down to discrete one in its Hamiltonian does not remove a phase transition and may induce nontrivial effects on the critical exponents of a phase transition [127, 128]. Such a field may be dangerously irrelevant in the sense that the fixed point of the renormalization group analysis is the original one and thus the critical exponent $\nu$ is identical, but some of the critical exponents such as $\gamma'$ and $\gamma$ are modified [*2]. The magnetic field in our model of

[*1] For example, a susceptibility

$$\chi_{\mathrm{plane}} = \sum_{r_y} \chi\left(r_y\right), \tag{8.1}$$

where

$$\chi\left(r_y\right) = L^2 \beta \left[\left\langle \boldsymbol{m}_{r_y}^2 \right\rangle - \left\langle \boldsymbol{m}_{r_y} \right\rangle^2\right], \tag{8.2}$$

$$\boldsymbol{m}_{r_y} = \frac{1}{L^2} \sum_{\boldsymbol{r} \in \left\{(x,y,z) \mid y = r_y\right\}} \boldsymbol{S}_{\boldsymbol{r}} \tag{8.3}$$

may be utilized to study the fluctuation. These quantities can be directly computed in numerical simulations.

[*2] Here we denote the critical exponent that characterizes the divergence of the susceptibility $\chi$ at a critical temperature $T_{\mathrm{c}}$ from higher temperature as $\gamma$ ($\chi \sim (T - T_{\mathrm{c}})^{-\gamma}$) and that from lower

a uni-axial chiral magnet is a field which breaks the continuous symmetry of the system without the magnetic field. We thus expect our model in the magnetic field can be explained by the theory. Indeed, according to the results obtained in our Monte Carlo simulations, the critical exponent $\nu$ of the phase transition of the system with the weak magnetic field is identical to that of the system without the magnetic field, i.e. the three-dimensional $XY$ model. We have not estimated other critical exponents here, but some of the exponents above and below the critical temperature can be different from each other as the models in Refs. [127, 128]. More surprisingly, the magnetic field, an irrelevant field when $h/J = 0.1$ and 0.2 in our model, completely changes the criticality of the phase transition. At higher magnetic field, $h/J = 0.3$ in our simulations, strong divergences in the specific heat and the uniform magnetic susceptibility are observed at the critical temperature. The magnetic field is no longer irrelevant at $h/J = 0.3$. We may expect naively that two different phases with two different broken symmetry exist in the low temperature region with two different types of phase transitions. However, the symmetry of the system with the magnetic field is independent of the value $h/J$, and the low temperature CSL phase is identical. It is very important for understanding of the system to see how fixed points corresponding to the phase transition at low and high magnetic fields appear and relate to each other, and renormalization flows converge to each fixed point in the renormalization group theory.

We used the spin glass order parameter, or the spin overlap, $q = \sum_i \boldsymbol{S}_i^{(1)} \cdot \boldsymbol{S}_i^{(2)}/N$ to detect the phase transition of the system with the magnetic field. For translationally invariant systems, the spin overlap can be written using the wave-vector-dependent magnetizations by Fourier transformation as

$$q \propto \sum_{\boldsymbol{k},\boldsymbol{k}'} \boldsymbol{m}(\boldsymbol{k}) \cdot \boldsymbol{m}(\boldsymbol{k}') \,. \tag{8.4}$$

Thus, the overlap is expected to detect periodic orders characterized by the magnetizations with several wave vectors. For our system with a free boundary condition in the $y$ direction, Eq. (8.4) needs some corrections. However, the corrections vanish in the thermodynamic limit, and the overlap gives the correct critical exponents by using a usual finite-size scaling analysis with corrections to scaling. Indeed, it gives a consistent value of the critical exponent of the correlation length $\nu$ (see Fig. 7.9) of the system without the magnetic field, and we successfully obtain the exponent $\nu$ in the presence of the magnetic field $h/J = 0.2$. We can detect through the overlap an order with a spatially modulated structure even when the order is characterized by multiple wave vectors. While a consistent value of the exponent $\nu$ is obtained numerically at least in the case $h/J = 0$, the applicability of the overlap, or the types of orders and phase transitions detectable by the overlap, are not clear. We can naively expect that any periodic orders accompanying slowing down in the autocorrelation function of spins can be detected by the overlap. On the other hand, it has been reported that the spin glass order parameter does not detect a spin nematic order [129, 130]. Further theoretical and numerical studies are necessary to clarify the limitation of the spin overlap as an order parameter.

temperature as $\gamma'$ ($\chi \sim (T_c - T)^{-\gamma'}$).

# Part III

# Melting of skyrmions in two spatial dimensions

# 9

# Introduction to skyrmions in chiral magnets and two-dimensional melting

Skyrmions are particle-like excitations introduced in field theory by T. H. R. Skyrme in 1962 [131]. They are characterized by a topological integer, and topologically stable objects in the sense that any continuous change cannot destroy them. After decades, skyrmions are turned out to be significant in magnetic systems [132–134]; many spins form a topologically stable particle-like vortex. Various magnetic systems have been known in which skyrmions are stabilized [134]; spin systems with frustrating exchange interactions [135] and dipole-dipole interactions [136]; the Kondo lattice model with classical localized spins [137]. In these systems, skyrmions and anti-skyrmions, which has a topological integer with an opposite sign, emerge with the same energy, or statistical weight because of chiral symmetry in the systems.

In recent years, skyrmions that emerge in chiral magnets have been extensively studied both experimentally and theoretically. They are stabilized by competition between the exchange interactions, the antisymmetric Dzyloshinskii–Moriya (DM) interactions, and a magnetic field. As the bi-axial antisymmetric DM interactions break chiral symmetry, only one kind of skyrmion (or anti-skyrmion) with the same topological integer emerges. Such skyrmions have been observed in various chiral magnets such as MnSi, $Fe_{1-x}Co_xSi$ [134, 138–144]. Real-space observation of skyrmions is reported using transmission electron microscopy [140, 145], and their size is known to be typically ten times larger than the lattice spacing of spins [134].

Phase diagram of chiral magnets strongly depends on their spatial dimensionality. In three-dimensional bulk systems, skyrmions are observed only in a very narrow window in the phase diagram at finite temperature as skyrmion triangular crystal states in both experiments and Monte Carlo simulations [134, 138, 139, 141, 146]. On the other hand, in two-dimensional chiral magnets, or quasi-two-dimensional thin films of chiral magnets, skyrmions exist in a wide region of the phase diagram at low temperature [134, 140–142, 145, 147–150]. Furthermore, a triangular skyrmion crystal state exists as the ground state, and it is reported stable at finite temperature [134, 140–142, 147, 149]. As one of the largest differences from three-dimensional bulk systems, skyrmions in thin films are stable even when they are isolated. We thus expect that a completely different phase transition from the three-dimensional system occurs at finite temperature.

As skyrmions can be stable isolated objects in two dimensions, we can effectively interpret them as particles interacting with each other. Phase transitions in two-dimensional chiral magnets involved in skyrmions thus should be studied in the analogy with two-dimensional particles. In two-dimensional particle models, particles cannot form a crystal state at finite temperature (or finite density) [151], which has a long-range positional order. However, they can form a solid with a quasi-long-range positional order and a long-range orientational order [152]. With increasing temperature (or decreasing density), the solid state melts into a hexatic state with a short-range positional order and a quasi-long-range

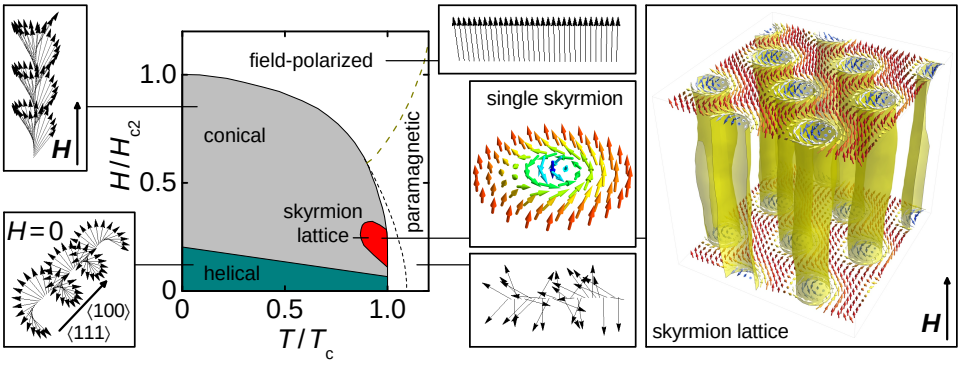


Fig. 9.1: Phase diagram of a three-dimensional bulk MnSi [162]. Skyrmions are thermodynamically stable only in the skyrmion lattice phase, also known as the "A phase".

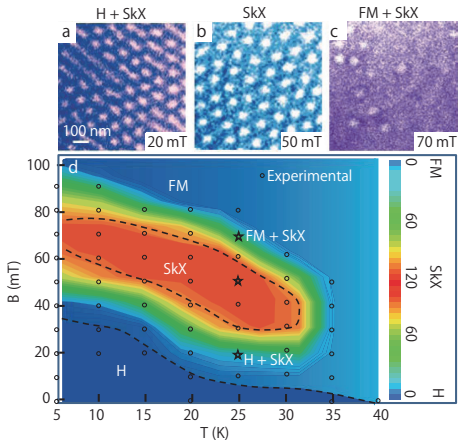


Fig. 9.2: Phase diagram of a thin film of $Fe_{0.5}Co_{0.5}Si$ [140]. Skyrmions exist in a wide region of the phase diagram.

orientational order, and finally, the hexatic state melts into a liquid phase, where both the positional and the orientational orders have short-range correlations [69, 153]. These melting transitions have been discussed for decades from the first Monte Carlo simulation by N. Metopolis and coworkers [1], the first event-driven molecular dynamics simulation by B. J. Alder and T. E. Wainwright [154], and the Kosterlitz–Thouless–Halperin–Nelson–Young (KTHNY) theory [155–160], to recent studies by large-scale Monte Carlo simulations [24, 69, 153] and a high-precision experiment [161].

In this chapter, we review some of the experimental facts on the phase diagram of chiral magnets in both three dimensions and two dimensions. We also discuss the theory of two-dimensional melting transition in particle systems, the KTHNY theory, and recent results on the systems obtained by numerical simulations.

## 9.1 Experiments on skyrmions in chiral magnets

In a three-dimensional crystal of MnSi, we can find four different phases of spins [138, 139, 162]; the paramagnetic phase, the helical phase, the conical phase, and the skyrmion crystal phase, see Fig. 9.1. In the skyrmion crystal phase, also known as the "A phase" [138], a triangular lattice structure extends to the plane perpendicular to the magnetic field. Skyrmions are observed only in the A phase, a very small region in the phase

diagram, in three dimensions. Phase transitions into the skyrmion crystal phase are of first order [139]. At lower temperature, the conical state has a lower energy than the skyrmion crystal state, and thus the state is dominant in the low temperature region. The crystal state is stabilized entropically at finite temperature. The small region of the crystal phase is also found in other materials [141, 142].

With reducing the thickness of materials such as MnSi and FeGe, the region of the skyrmion crystal phase becomes larger, and eventually, extends to zero temperature [134, 140–142, 145], see Fig. 9.2 for the phase diagram of a thin film of $Fe_{0.5}Co_{0.5}Si$. The conical state, which has a three-dimensional structure parallel to the magnetic field, can no longer exist in thin films. Surprisingly, in thin films of chiral magnets, skyrmions are thermodynamically stable even in the paramagnetic phase as isolated excitations. This suggests that a phase transition between ordered and disordered phases of skyrmions occurs in contrast to the three-dimensional bulk chiral magnets.

## 9.2 Two-dimensional melting of particles

### 9.2.1 The KTHNY theory

The KTHNY theory [155–160] of melting transition in two-dimensions was developed by B. I. Halperin, D. R. Nelson, and A. P. Young based on the Kosterlitz–Thouless (KT) theory for the two-dimensional $XY$ model, a thin film of $^4$He, and two-dimensional particles [155, 156]. The KT theory predicts, as in the two-dimensional $XY$ model, a solid–liquid melting transition at temperature $T_{\mathrm{m}}$ driven by unbinding of topological defects, dislocations, in two-dimensional particles. Halperin and Nelson [157, 159], and Young [158] pointed out that the melted phase with unbound dislocations is not a simple isotropic liquid phase, but a hexatic phase with bounded disclinations, where the orientational and the positional correlations decay algebraically and exponentially, respectively. At higher temperature $T_{\mathrm{I}} > T_{\mathrm{m}}$, the hexatic phase melts into a liquid phase with free disclinations that makes all of correlations short-ranged. See Tab 9.1 for the correlations of the orientational and the positional orders in each phase.

At low temperature (or high density) in the solid phase without periodic substrates, the system can be described by the following effective Hamiltonian:

$$H_{\mathrm{E}} = \frac{1}{2}\int d\boldsymbol{r} \sum_{i,j} \left(2\mu u_{ij}^2(\boldsymbol{r}) + \lambda u_{ii}^2(\boldsymbol{r})\right), \tag{9.1}$$

where $\boldsymbol{u}(\boldsymbol{r}) = (u_x(\boldsymbol{r}), u_y(\boldsymbol{r}))$ is the deviations from the complete triangular crystal structure in the ground state, the linearized symmetric tensor

$$u_{ij}(\boldsymbol{r}) = \frac{1}{2}\left(\frac{\partial u_i}{\partial r_j} + \frac{\partial u_j}{\partial r_i}\right) \quad (i,j = x,y), \tag{9.2}$$

and $\mu$ and $\lambda$ are Lamé coefficients. The effective Hamiltonian gives at very low but finite

| | Orientational order | Positional order |
|---|---|---|
| Liquid | Short-range | Short-range |
| Hexatic | Quasi-long-range | Short-range |
| Solid | Long-range | Quasi-long-range |

Table 9.1: Correlations of the orientational and the positional orders in each phase.

temperature that

$$g_{\boldsymbol{k}_0}(r) \sim r^{-\eta_{\boldsymbol{k}_0}(T)}, \tag{9.3}$$

$$\eta_{\boldsymbol{k}_0} = \frac{k_{\mathrm{B}} T \left|\boldsymbol{k}_0\right|^2 (3\mu + \lambda)}{4\pi (2\mu + \lambda)}, \tag{9.4}$$

where $\boldsymbol{k}_0$ is a reciprocal vector of the lattice structure. This algebraic decay in the positional correlation means that two-dimensional particles do not form a crystal, which has a long-range positional correlation, at any finite temperature. However, the orientational order parameter

$$\psi(\boldsymbol{r}) = \exp(6i\theta(\boldsymbol{r})), \tag{9.5}$$

has a long-range correlation, $\langle \psi^*(\boldsymbol{r})\psi(\boldsymbol{0})\rangle > 0$ even in the limit $|\boldsymbol{r}| \to \infty$, where $\theta(\boldsymbol{r})$ is the orientational field defined as

$$\theta(\boldsymbol{r}) = \boldsymbol{e}_z \cdot \nabla \times \boldsymbol{u}(\boldsymbol{r}) = \frac{1}{2}\left(\frac{\partial u_i}{\partial r_j} - \frac{\partial u_j}{\partial r_i}\right). \tag{9.6}$$

These are completely consistent with the theory of the harmonic solid by N. D. Mermin [152]. A free dislocation has a diverging energy $\sim \log(L)$ ($L$ is the linear dimension of the box), thus no free dislocation exists in the solid phase. The energy scale of a dislocation determines a melting transition $T_{\mathrm{m}}$ of the solid state. Just above $T_{\mathrm{m}}$, the density of free dislocations is finite. By taking account of contributions from dislocations in the effective Hamiltonian, we find using renormalization group calculation the exponentially decaying correlation length of the positional order with increasing temperature

$$\xi_+(T) = \exp(\mathrm{const}/(T - T_{\mathrm{m}})^{\nu}), \tag{9.7}$$

where $\nu = 0.3696...$ [159]. Approaching $T_{\mathrm{m}}$ from below, the exponent $\eta_{\boldsymbol{k}_0}(T)$ increases, and in the limit $T \to T_{\mathrm{m}}$, $\eta_{\boldsymbol{k}_0}(T) \to 1/3$. Any solid with the exponent $\eta_{\boldsymbol{k}_0}(T) > 1/3$ is unstable due to unbinding of dislocations.

Above the melting temperature $T_{\mathrm{m}}$, if the orientational order is not short-ranged, the system on large length scale is controlled by an effective Hamiltonian

$$H_{\mathrm{A}} = \frac{1}{2} K_{\mathrm{A}} \int d\boldsymbol{r} \left|\nabla\theta(\boldsymbol{r})\right|^2, \tag{9.8}$$

as in the ferromagnetic $XY$ model in two dimensions [155, 156]. Here, $K_{\mathrm{A}}$ is essentially the same as the Frank constant that has a positive value in the presence of a (quasi-)long-range correlation in the orientational order. By renormalization group analysis, the Frank constant $K_{\mathrm{A}}$ is found to have a finite value if the system is in a smooth substrate, which implies a quasi-long-range correlation in the orientational order. The effective Hamiltonian Eq. (9.8) indeed gives an algebraic decay in the correlation function of the orientational order

$$\langle \psi^*(\boldsymbol{r})\psi(\boldsymbol{0})\rangle \sim r^{-\eta_6(T)}. \tag{9.9}$$

As the case of the melting transition of solid, by taking disclinations into account, we obtain the exponent $\eta_6(T) \to 1/4$ with approaching the transition temperature $T_{\mathrm{I}}$ from below, which is again estimated by the energy scale of a free disclination. The correlation length of the orientational order can be also calculated as

$$\xi_\psi(T) = \exp\left(\mathrm{const}/(T - T_{\mathrm{I}})^{1/2}\right). \tag{9.10}$$

In the presence of a periodic substrate under particles, the KTHNY theory slightly modified depending on the strength, the shape, and the fineness of the substrate [157–159]. If the periodic substrate is commensurate to the lattice structure of the solid state, a true crystal state with a long-range positional correlation exists at finite temperature. In the following, we particularly focus on the case of a weak incommensurate periodic substrate. Let us consider an effective Hamiltonian of particles in a periodic substrate

$$H_{\mathrm{P}} = H_{\mathrm{E}} - \sum_{\boldsymbol{r}} V\left(\boldsymbol{r} + \boldsymbol{u}\left(\boldsymbol{r}\right)\right), \tag{9.11}$$

where $H_{\mathrm{E}}$ is the effective Hamiltonian for the solid phase Eq. (9.1), and $V\left(\boldsymbol{r}\right)$ is the periodic substrate. Assuming that an angle of between the orientation of the solid state and the underlying periodic substrate varies slowly and small, we then find the effective Hamiltonian Eq.(9.11) can be written as

$$H_{\mathrm{P}} = \frac{1}{2}\int \sum_{i,j} \left(2\mu u_{ij}\left(\boldsymbol{r}\right) + \lambda u_i^2\right) + 4\gamma\theta^2\left(\boldsymbol{r}\right), \tag{9.12}$$

where $\gamma$ is an elastic constant determined by the periodic substrate. We can find by using this effective Hamiltonian that the low-temperature solid phase and the dislocation-unbinding transition are qualitatively the same as the case of particles without periodic substrate. However, at temperature slightly higher than $T_{\mathrm{m}}$, Halperin and Nelson argued that the Frank constant can be infinitely large, which indicates that the orientational order has a long-range correlation, and at $T_{\mathrm{I}}$, the two-dimensional Ising type phase transition occurs to an isotropic liquid phase if the periodic substrate has a square-lattice shape [157, 159].

### 9.2.2 Melting of hard and soft particles in a smooth substrate

After the KTHNY theory, many theoretical and experimental works studied the melting transition in two-dimensional particles, especially in hard disks, but, contradicting results had been reported until recently. For example, by using isobaric Monte Carlo simulations of 1000 hard disks, J. Lee and K. J. Strandburg showed an evidence of a first-order phase transition [163]. On the other hand, by large-scale Monte Carlo simulations of hard disks, C. H. Mak claimed that two continuous phase transitions occur according to the KTHNY theory [164]. However, E. P. Bernard and W. Krauth [67] showed using the event-chain algorithm (discussed in the previous part) that another scenario holds in two-dimensional hard disks: A first-order phase transition between the liquid and the hexatic, and a KT phase transition between the hexatic and the solid. This result is confirmed by numerical simulations with three independent algorithms [24], and a recent experiment [161].

Melting transition in soft disks with an interaction $U\left(r\right) = \left(\sigma/r\right)^n$ is also investigated recently [153]. The model includes the hard disks in the limit $n \to \infty$. Surprisingly, the nature of the hexatic–liquid phase transition depends on $n$: While $n \gtrsim 6$, the transition is of first-order as hard disks, it becomes a KT transition when $n \lesssim 6$. The melting transitions also depend on the shape of particles. Two-step melting with both a first-order and a KT hexatic–liquid transitions is observed depending on the shape, and even one-step direct solid–liquid melting is found [26].

# 10 Simulation method

In this chapter, we introduce a classical Heisenberg spin model of a two-dimensional chiral magnet. We also discuss a difficulty of Monte Carlo simulations of the model and our strategy to study a phase transition. A detail of massive spatial parallelization using GPUs is presented. Three important order parameters, the orientational, positional, and directional order parameters, are introduced in the end of the chapter.

## 10.1 Model

As a model of a two-dimensional chiral magnet, we consider a system defined by the Hamiltonian

$$H\left(\{\boldsymbol{S}_i\}\right) = -J\sum_{\langle i,j\rangle}\boldsymbol{S}_i\cdot\boldsymbol{S}_j - \boldsymbol{D}_x\cdot\sum_i \boldsymbol{S}_i\times\boldsymbol{S}_{i+\boldsymbol{e}_x} - \boldsymbol{D}_y\cdot\sum_i \boldsymbol{S}_i\times\boldsymbol{S}_{i+\boldsymbol{e}_y} - \boldsymbol{h}\cdot\sum_i \boldsymbol{S}_i. \quad (10.1)$$

In this Hamiltonian, $\boldsymbol{S}_i$ is a classical Heisenberg spin with $|\boldsymbol{S}_i| = 1$ on a site $i$ of the two-dimensional square lattice with periodic boundary conditions. The bracket $\langle\cdot,\cdot\rangle$ represents a neighboring pair of lattice sites. The second and third terms in the Hamiltonian constitute the DM interaction. We take $\boldsymbol{h}$ parallel to the $z$-axis, $\boldsymbol{D}_x$ parallel to the $x$-axis, $\boldsymbol{D}_y$ parallel to the $y$-axis, and choose $|\boldsymbol{D}_x| = |\boldsymbol{D}_y| = J$. Bloch-type skyrmions [144] are stabilized at low temperature with the choice of parameters in the magnetic field, for example, $h/J = 0.6$, see Fig. 10.1.

Due to the bi-axial DM interaction, the model has no continuous symmetry even if the magnetic field is absent. The only discrete symmetry in the spin space of the model without the magnetic field is inversion symmetry $\boldsymbol{S}_i \to -\boldsymbol{S}_i$. In the presence of the

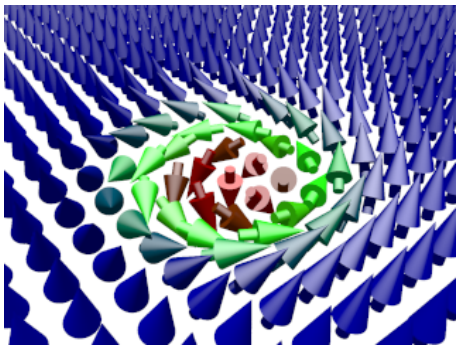

Fig. 10.1: A Bloch-type skyrmion in the model of a two-dimensional chiral magnet defined by the Hamiltonian Eq. (10.1).

magnetic field, the system only has symmetry involved in the underlying spin lattice; for example, trivial translation symmetry

$$(r_x, r_y) \to (r_x + \delta_x, r_y + \delta_y) \quad (\delta_x, \delta_y \in \mathbb{N}), \tag{10.2}$$

and lattice inversion symmetry coupled with spin inversion

$$\begin{cases} (r_x, r_y) \to (\pm r_x, \mp r_y), \\ \boldsymbol{S}_i = (S_{i,x}, S_{i,y}, S_{i,z}) \to \boldsymbol{S}'_i = (\mp S_{i,x}, \pm S_{i,y}, S_{i,z}). \end{cases} \tag{10.3}$$

The ground state structure of the system, especially in the presence of the magnetic field, is highly nontrivial due to competition of the isotropic, the DM interactions and the magnetic field. Recent studies [134, 141, 147, 150, 165] report that the ground state is either the helical, the skyrmion crystal, or the paramagnetic phase depending on the magnetic field. The skyrmion crystal state has long-range positional and orientational orders with a triangular-lattice structure. However, the winding number in the helical phase, and the density of skyrmions in the skyrmion crystal phase are unclear. Numerical calculations to compare the energies of states with various winding number of helices and various skyrmion numbers are necessary to determine detailed properties of each phase and transition points.

## 10.2 Choice of lattice parameters

The skyrmions in the low temperature region are expected to form a triangular lattice structure. A complete triangular lattice with "base" orientation, in which each elementary triangle points upward, has a linear dimension in the $y$ direction which is $\frac{\sqrt{3}}{2}$ times shorter than that of the $x$ direction. The skyrmion crystal and solid states are sensitive to the boundary conditions and expected to have large finite-size effects if the lattice structure is incommensurate to the simulation box although they vanish in the thermodynamic limit. We thus set the linear dimensions of the underlying spin lattice $L_x = k \times 97$ in the $x$ direction and $L_y = 84 \times k$ in the $y$ direction ($k \in \mathbb{N}$) to study the skyrmion crystal and solid states with triangular lattice structures. This choice of the linear dimensions realizes a ratio $L_x/L_y \simeq 0.865979$ that is very close to $\sqrt{3}/2 \simeq 0.866025$.

On the other hand, at low magnetic field, the system is in the helical phase in which helices go up or down with $\pm\pi/4$ tilting (this angle $\pm\pi/4$ is determined by the choice of the parameters $|\boldsymbol{D}_x| = |\boldsymbol{D}_y|$). The rectangular-shape spin lattice above is incommensurate to the helical states. A skyrmion crystal state with a square lattice structure commensurate to the underlying spin lattice, which is in principle possibly realized at zero temperature, is also incommensurate to it. We use a square-shape spin lattice with linear dimensions $L$ for these two cases.

## 10.3 Zero-temperature simulated annealing

At zero temperature, energy minimization and simulated annealing along the magnetic field are carried out by using the heat-bath algorithm at zero temperature, where spins are aligned to the local field determined by interacting spins and the magnetic field. The zero-temperature phase diagram can be constructed by directly comparing the energy density of the helical states with various winding numbers, the skyrmion crystal states with various densities, and the paramagnetic state. We use $4 \times 10^3$ sweeps to minimize the energy of the system at each magnetic field. The helical initial configurations are prepared at $h/J = 0$ using a single wave vector $\boldsymbol{q} = 2m\pi/L\,(1, 1)$ ($m \in \mathbb{N}$). Triangular and square

skyrmion configurations with various densities are produced from many skyrmions placed very close to the corresponding lattice sites (each skyrmion is prepared in a small system with $7 \times 7$ spins at $h/J = 0.6$). Simulated annealing runs are performed from $h/J = 0$ to higher magnetic field for helical states with $|\Delta h/J| = 0.001$, and from $h/J = 0.6$ to lower and higher magnetic field with the same $|\Delta h/J|$ for triangular skyrmion states. To find whether square skyrmion states can have a lower energy than triangular states in the low density region, i.e. in the vicinity of the transition field $h_{\mathrm{SP}}$, we also perform simulated annealing simulations from $h/J = 0.7$ to lower magnetic field with $|\Delta h/J| = 0.0001$.

## 10.4 Difficulty of simulation of skyrmions at low temperature

Each skyrmion consists of tens of spins with our choice of the parameters. A large free-energy barrier prevents regular Monte Carlo algorithms such as the heat-bath and the over-relaxation algorithms from destroying/creating skyrmions in a short time. That causes a serious relaxation problem in the low temperature region: Physical quantities, even the energy density, starting from completely different initial conditions, a ferromagnetic and a random configuration, do not coincide with each other for more than $10^6$ Monte Carlo sweeps even for a small system with $128^2$ spins, see Fig. 10.2. We may apply the event-chain algorithm discussed in Section 3 to the system. However, unfortunately, due to a lack of continuous symmetry, it does not work well, and no speed-up is seen by the event-chain algorithm for the system.

Skyrmions are topological excitations with local energies, and we expect the free-energy barrier is $O(1)$ but takes a large value at low temperature. To create/destroy skyrmions, or to change the number of skyrmions in a short time, we consider an algorithm that realizes a heating and an annealing process of a local region with keeping the detailed balance condition (which is referred to as Annealing/Heating-Operation (AHO) algorithm in the following). Let us suppose a region where $\ell$ spins $\boldsymbol{\sigma}$ reside in a system with inverse temperature $\beta$. We change temperature of the region according to a schedule $S = \{\beta \to \beta_0 \to \cdots \to \beta_{M-1} \to \beta_{M-1} \to \beta_{M-2} \to \cdots \beta_0 \to \beta\}$. At each temperature, spins in the region are updated using the heat-bath algorithm with other fixed spins outside the region. A new spin configuration $\boldsymbol{\sigma}'$ is accepted by the Metropolis acceptance probability

$$P(\boldsymbol{\sigma}, \boldsymbol{\sigma}', S) = \min(1, r), \tag{10.4}$$

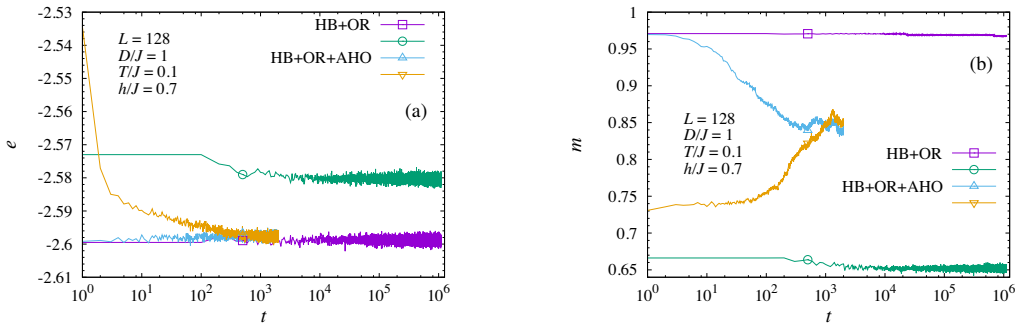


Fig. 10.2: Monte Carlo time dependence of the energy density (a) and the magnetization (b) starting from the ferromagnetic configuration (square and upward triangular symbols) and a random configuration (circle and downward triangular symbols). "HB", "OR", and "AHO" stand the heat-bath, the over-relaxation, and the Annealing/Heating-Operation algorithms, respectively.

where

$$r = \exp\{(\beta_0 - \beta)(E_0 - E_{2M}) + (\beta_1 - \beta_0)(E_1 - E_{2M-1}) + \cdots \\ \cdots + (\beta_{M-1} - \beta_{M-2})(E_{M-1} - E_{M+1}).\} \quad (10.5)$$

to satisfy detailed balance. Here, $E_i$ is the energy of the system at $i$-th temperature in the schedule $S$. This AHO algorithm with well tuned parameters, for example, $\ell = 16$, $M = 1200$, $\beta = 10$, and $\beta_M = 4$, has a considerable acceptance probability, and allows the energy density and the magnetization starting from two completely different states to coincide with each other in a short Monte Carlo time steps, see Fig. 10.2. However, unfortunately, it takes $O(M)$ times longer real time for every step than regular algorithms, and the algorithm seems not to be useful for our system even though the convergence time is more than $M$ times faster.

We may construct a geometric cluster algorithms as discussed in Section 2.3.2 using the symmetry Eq. (10.2) or Eq. (10.3), but, the algorithms are inefficient due to the cluster-size problem discussed in Section 2.3.3, with which cluster algorithms are confronted for many complex models.

## 10.5 Strategy for Monte Carlo simulations at finite temperature

To overcome the difficulty of conventional Monte Carlo simulations of the system, we perform Monte Carlo simulations in two stages as follows. In the first stage, by extensive simulated annealing simulations from high temperature where the skyrmion number changes fast, we find the thermodynamic dominant number of skyrmions $N_{\rm s}$ at low temperature. Cooling rate dependence of the resultant $N_{\rm s}$ is carefully checked to obtain the correct value of $N_{\rm s}$. In the second stage, we compute some physical quantities presented below with the fixed number of skyrmions $N_{\rm s}$, which is estimated in the first stage. Results obtained by this procedure coincide with those obtained by regular Monte Carlo simulations toward the thermodynamic limit.

At the magnetic field $h/J = 0.5$, in our simulated annealing simulations starting from $T/J = 0.955$ to $0.155$ with $\Delta T/J = 0.01$, the number of Monte Carlo steps at each temperature $M$ is controlled, where one Monte Carlo time step consists of one heat-bath sweep followed by ten over-relaxation sweeps. Both algorithms are carried out with a sequential update. The equilibrium number of skyrmions is obtained in the limit of vanishing cooling rate $\theta \to 0$. After the thermodynamic dominant value $N_{\rm s}$ is found, we fix the number during simulations to calculate physical quantities. In the simulations, one unit Monte Carlo time step consists of one heat-bath sweep and $10^4$ over-relaxation sweeps. The number of skyrmions is checked every Monte Carlo time step using an integer-valued topological charge [166], and a new configuration is rejected if the number of skyrmions is changed from the thermodynamic dominant value. This algorithm strictly preserves the number of skyrmions during simulations.

## 10.6 Massive parallelization with GPU

Because of the local nature of the Hamiltonian, we can implement the heat-bath and the over-relaxation algorithms with spatial parallelization. Recently, a general-purpose graphic processing unit (GPU) is extensively utilized for massive parallel computations ranging from exact numerical diagonalization of large matrices to large-scale molecular

dynamics and Monte Carlo simulations. In this work, we use GPUs to simulate our system with massive spatial parallelization using the two-color checkerboard decomposition of the system proposed in Refs. [22, 23]. The checkerboard consists of many "blocks" which are composed of $\ell \times \ell$ sites, see Fig. 10.3. Blocks on one of the two sub-lattices of the checkerboard are updated independently. In each block, spins residing on one of the two sub-lattices are updated simultaneously, and spins on the other sub-lattice are updated by turns. We choose $\ell = 16$ in our simulations. A parameter of this spatial parallelization using the checkerboard decomposition is the number of sweeps $K$ in each block. While the balance and the ergodicity conditions are always satisfied for any $K$, we take $K = 1$, which seems to be the best in the sense of the relaxation time of physical quantities such as the global orientational order of skyrmions (that is discussed below).

Our checkerboard decomposition that consists of many blocks with $16 \times 16$ spins is incommensurate to the rectangular-shaped underlying spin lattice with $L_x = 97 \times k$ and $L_y = 84 \times k$, and not all of the spins are updated in the checkerboard at a time. We randomly shift the checkerboard after every $10^2$ over-relaxation sweeps to assure the ergodicity condition.

## 10.7 Positions of skyrmions

We interpret skyrmions as point particles with an isotropic interaction. To this end, we define a position of each skyrmion $\boldsymbol{R} = (R_x, R_y)$ in the two-dimensional plane using lattice sites of spins composing the skyrmion and the spin variables as

$$R_\alpha = \frac{1}{A_{\mathrm{sk}}} \sum_{i \in \text{skyrmion}} (r_\alpha + S_{i,\alpha}), \quad (\alpha = x, y) \tag{10.6}$$

where $A_{\mathrm{sk}}$ is the number of spins composing the skyrmion, and $r_\alpha$ is a position of lattice site $i$. A connected cluster of spins with $S_{i,z} < 0$ is regarded as a skyrmion. An isolated skyrmion at zero temperature has a symmetric structure around its core, and spins near a core of a skyrmion are antiparallel to the magnetic field (they thus point into the $-z$ direction)). The definition gives the exact center of each skyrmion if it has a complete symmetric shape. At finite temperature, on the other hand, the thermal fluctuations of the Heisenberg spins induce fluctuations in the determination of the skyrmion position. While we may use other definitions of a position of a skyrmion, we expect that the same

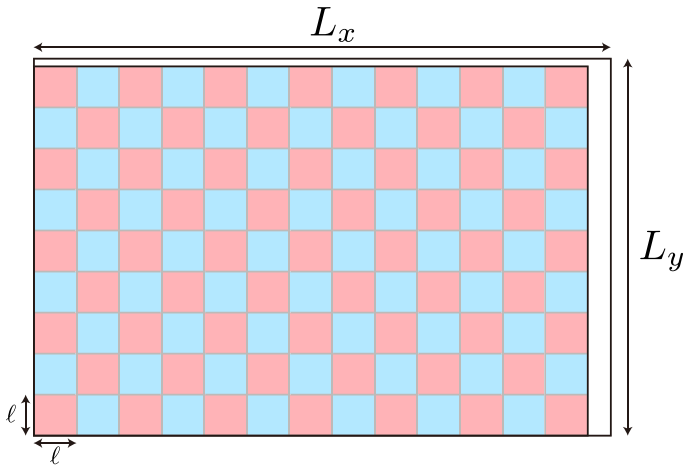


Fig. 10.3: A checkerboard decomposition of the system. Each block consists of $\ell \times \ell$ spins.

results are obtained unless they give a symmetric point as a position for a skyrmion at zero temperature that has a completely symmetric shape.

## 10.8 Physical quantities

In this section, we introduce three important order parameters to study phase transitions in the two-dimensional chiral magnet. The orientational and the positional orders are used for skyrmions with the interpretation as point particles. These parameters are traditionally studied for particle systems to find phase transitions. The other one, the directional order, is relevant for helical states. That detects a helical ordering in any direction.

### 10.8.1 Orientational order

The local orientational order parameter, explicitly introduced in Ref. [167], is a complex number that characterizes an orientation of a local lattice structure. A triangular lattice structure is invariant under a rotation of the whole system with an angle $\pm\pi/3$. The local orientation order of particle $j$ is defined so that the $\pm\pi/3$ rotation gives the same value as

$$\psi_j = \frac{1}{|\partial j|} \sum_{k \in \partial j} \exp\left(6i\theta_{jk}\right), \tag{10.7}$$

where $\partial j$ is a set of neighboring particles of $j$, and $\theta_{jk}$ is an angle of $\boldsymbol{r}_{jk} = \boldsymbol{r}_k - \boldsymbol{r}_j$ measured by a fixed axis, Fig. 10.4. The global orientational order $\Psi_6$ is simply defined as the average of $\psi_j$ over all particles. For a complete triangular-lattice configuration of particles, the global orientational order gives $|\Psi_6| = 1$. The local orientation order $\psi_j$ is a quantity like an $XY$ spin, but its length is changed depending on neighboring particles' configuration.

While the orientational order can be easily calculated once neighboring particles are identified, it is unclear what an appropriate definition of neighboring particles is. Indeed, the value of the orientational order itself and its behavior strongly depends on the choice of the definition [168]. Here, we use a definition based on the Delaunay triangulation, the dual of the Voronoi tessellation, to find neighboring pairs of particles. Note that many works (for example, see [26, 167, 169–173]) have adopted a definition based on the distance between particles; each pair of particles at distance shorter than a fixed threshold

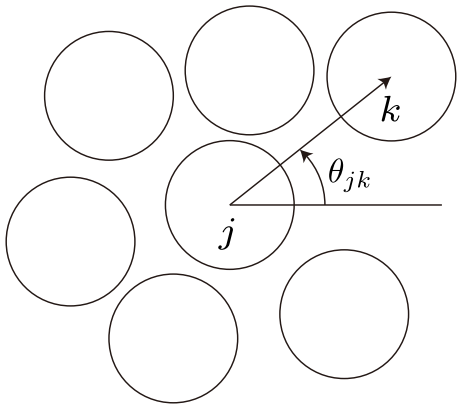


Fig. 10.4: An angle $\theta_{jk}$ of a bond $\boldsymbol{r}_{jk} = \boldsymbol{r}_k - \boldsymbol{r}_j$ between two particles $j$ and $k$.

is regarded as neighboring particles. This definition reduces a computational time to find neighboring particles, but a result is expected to depend on the threshold, and we do not know a priori how to find an "appropriate" threshold.

We define the correlation function of the local orientational order

$$g_6(r) = \left\langle \frac{1}{N_\mathrm{s}} \sum_{j,k} \psi_j^* \psi_k \delta\left(r - |\boldsymbol{r}_k - \boldsymbol{r}_j|\right) \right\rangle \tag{10.8}$$

to find a phase transition involved in the orientational order. In the solid or crystalline phase, the correlation function of an infinite system remained finite even in the limit $r \to \infty$. On the other hand, it decays to zero algebraically in the hexatic phase and exponentially in the liquid phase. The correlation function is computed as a histogram of the distance between two skyrmions with weight $\psi_j^* \psi_k$. The size of each bin of the histogram is $1/5a_0$, where $a_0$ is the lattice spacing of spins.

### 10.8.2 Positional order

The positional order of $N$ particles is characterized by the structure factor

$$S(\boldsymbol{q}) = \left\langle \frac{1}{N} \sum_{j,k} \exp\left(i\boldsymbol{q} \cdot (\boldsymbol{r}_j - \boldsymbol{r}_k)\right) \right\rangle, \tag{10.9}$$

where $\boldsymbol{q}$ is a two-dimensional vector, and $\boldsymbol{r}_j$ is a position of particle $j$. By using a wave vector $\boldsymbol{q}_0$ where the structure factor $S(\boldsymbol{q})$ has the largest peak, the positional order parameter is defined as

$$v = \frac{1}{N} \sum_j \exp\left(-i\boldsymbol{q}_0 \cdot \boldsymbol{r}_j\right). \tag{10.10}$$

The positional correlation function is defined using $v$ as

$$g_{\boldsymbol{q}_0}(r) = \left\langle \frac{1}{N} \sum_{j,k} \exp\left(i\boldsymbol{q}_0 \cdot (\boldsymbol{r}_j - \boldsymbol{r}_k)\right) \right\rangle. \tag{10.11}$$

However, for off-lattice particles as well as skyrmions in our model with the interpretation, unlike spin models on a finite regular lattice, the wave vector $\boldsymbol{q}_0$ can have real-valued components, and to find the wave vector $\boldsymbol{q}_0$ is a computationally time-consuming task with the Fourier transform and an interpolation. We therefore focus on the two-dimensional positional correlation function

$$g(\boldsymbol{\Delta r}) = \left\langle \frac{1}{N} \sum_{i,j} \delta\left(\boldsymbol{\Delta r} - (\boldsymbol{r}_j - \boldsymbol{r}_i)\right) \right\rangle, \tag{10.12}$$

that can be obtained without knowing $\boldsymbol{q}_0$ [69]. In the computation of $g(\boldsymbol{r})$, each configuration is rotated by $-\arg(\Psi_6/6)$ so that the resultant $\Psi_6$ is approximately parallel to the $x$ axis [69]. Note that while in the liquid and hexatic phase $g(\boldsymbol{r})$ decays to 1 exponentially, it decays to 1 algebraically in the solid phase. If the correlation function decays to a value larger than 1, that means long-range positional order exists and the system is in the crystal phase. We compute the two-dimensional positional correlation function as a histogram of the displacement vectors between two skyrmions. The area of each two-dimensional bin is $a_0/5 \times a_0/5$.

### 10.8.3 Directional order

Helical orders have been studied by using the spin structure factor

$$S_{\text{spin}}(\boldsymbol{q}) = \left\langle \frac{1}{N} \sum_{j,k} \boldsymbol{S}_j \cdot \boldsymbol{S}_k \exp\left(i\boldsymbol{q} \cdot (\boldsymbol{r}_j - \boldsymbol{r}_k)\right) \right\rangle. \tag{10.13}$$

When the structure factor has the two largest peaks at non-zero vector $\pm\boldsymbol{q}_0$, the system has a helical order, and the wave-vector-dependent magnetization $\boldsymbol{m}(\boldsymbol{q}_0)$ (see Eq. (6.5)) may be regarded as an order parameter. In our system, two helical structures with $+\pi/4$ and $-\pi/4$ directions have the same statistical weight because of the symmetry Eq. (10.3) in the Hamiltonian. Two wave vectors $\boldsymbol{q}_0^{(1)}$ and $\boldsymbol{q}_0^{(2)}$ ($\boldsymbol{q}_0^{(1)} \perp \boldsymbol{q}_0^{(2)}$) characterize the order of the system, and one of the two helical structures appears over the whole system in the ground state. Therefore, we expect a spontaneous symmetry breaking associated with the direction of the helical structure occurs with a phase transition. However, the wave vectors are not known a priori, and, as discussed in the previous chapter, they depend not only on system sizes but also on temperature and the magnetic field.

We instead introduce another order parameter (the directional order parameter) that detects a direction of the helical structure over the system

$$\boldsymbol{\Phi} = \frac{1}{N} \sum_i \boldsymbol{\varphi}_i, \tag{10.14}$$

$$\boldsymbol{\varphi}_i = \boldsymbol{S}_i \times \boldsymbol{S}_{i+\boldsymbol{e}_x} + R_{\boldsymbol{e}_z}(-\pi/4)\, \boldsymbol{S}_i \times \boldsymbol{S}_{i+\boldsymbol{e}_y}, \tag{10.15}$$

where $R_{\boldsymbol{e}_z}(\theta)$ is a rotation matrix with an rotation axis $\boldsymbol{e}_z$ and an angle $\theta$. If a system has a homogeneous helical structure with an axis $\pm\boldsymbol{e}_x$, the order parameter $\boldsymbol{\Phi} \parallel +\boldsymbol{e}_x$, and $\boldsymbol{\Phi} \parallel -\boldsymbol{e}_x$ with an axis $\pm\boldsymbol{e}_y$. With our choice of the parameters $|\boldsymbol{D}_x| = |\boldsymbol{D}_y|$ in the Hamiltonian, only two helical structures that give $\boldsymbol{\Phi} \parallel \pm\boldsymbol{e}_y$ are dominant in the system. We thus focus on the $y$ component of $\boldsymbol{\Phi}$, and use the Binder parameter

$$U = \frac{1}{2}\left(3 - \frac{\left\langle \Phi_y^4 \right\rangle}{\left\langle \Phi_y^2 \right\rangle^2}\right). \tag{10.16}$$

to find a phase transition. Note that $\left\langle \Phi_y^n \right\rangle = 0$ ($n = 1, 3, \cdots$) because of the symmetry Eq. (10.3).

# 11

# Melting of skyrmions in two spatial dimensions

In this chapter, we present the results obtained by our Monte Carlo simulations of the system. We first discuss the zero-temperature phase diagram obtained by extensive simulated annealing simulations at zero temperature. Skyrmions are stabilized by each other, and the skyrmion crystal phase indeed exists in a finite region of the magnetic field. At finite temperature, by large-scale Monte Carlo simulations with massive parallelization discussed in Section 10.6, we show that the skyrmions form a typical two-dimensional solid without a long-range positional order rather than a crystal. The skyrmion solid state melts into the skyrmion liquid state in one stage without an intermediate hexatic phase, unlike two-dimensional particle models [*1]. We also discuss a phase transition between the paramagnetic and the helical phase, and the magnetic phase diagram.

## 11.1 Zero-temperature phase diagram

At zero temperature, the energy and the stability of a single skyrmion are studied by using the zero-temperature heat-bath algorithm. As the skyrmion is a local topological excitation, an energy difference between one single skyrmion and the paramagnetic spin

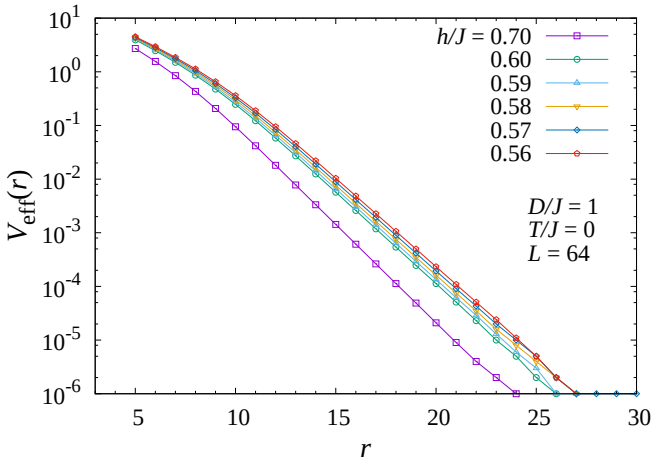


Fig. 11.1: An effective potential $V_{\rm eff}\,(r)$ between two skyrmions as a function of the distance $r$. The potential decreases exponentially with $r$.

[*1] Technically speaking, the high-temperature state of repulsive particles should be mentioned as a gas state. Nevertheless, here we refer to it as a liquid phase according to the previous studies in particle models.

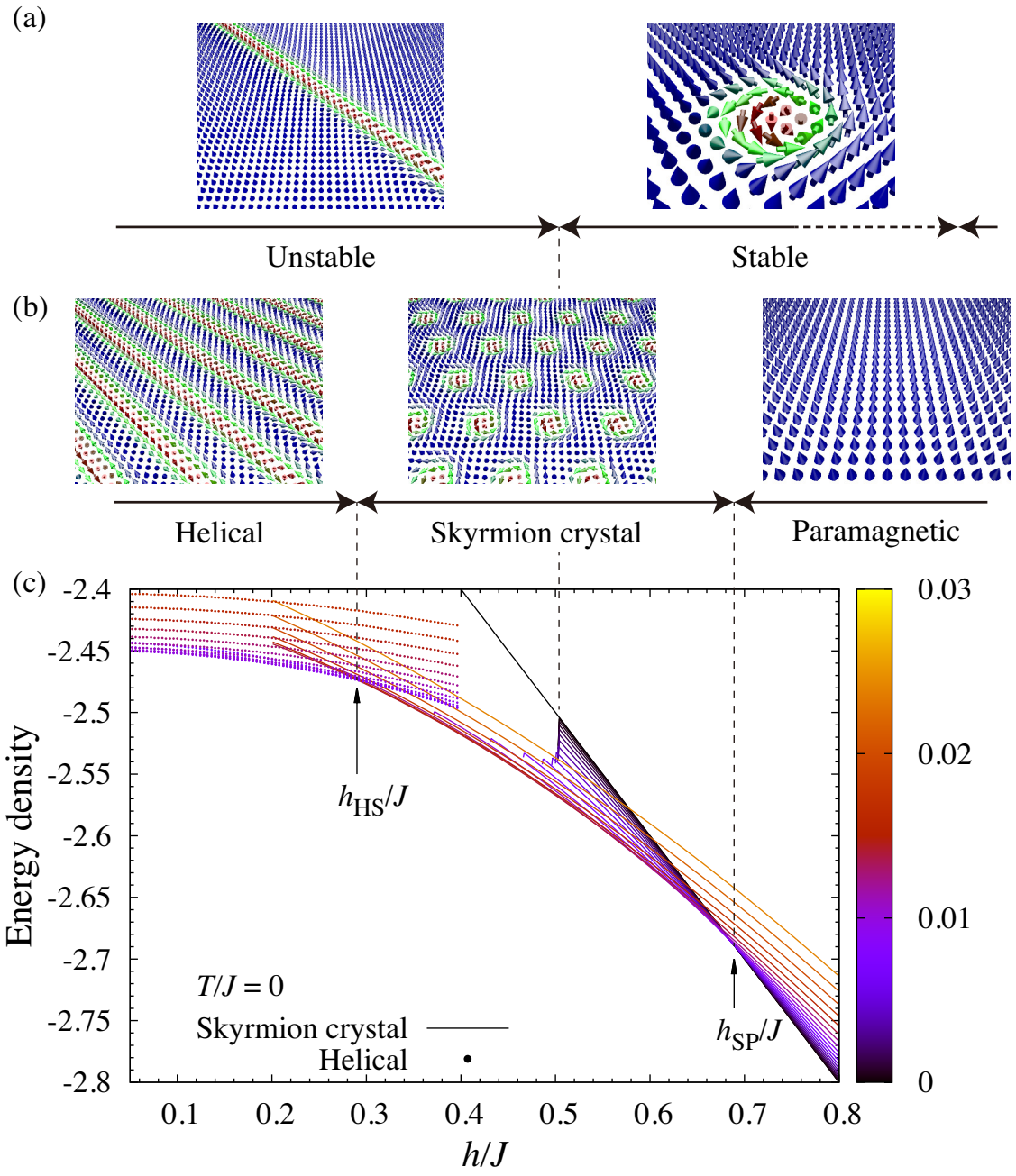


Fig. 11.2: (a) Phase diagram of a single skyrmion at zero temperature. For $h/J \lesssim 0.50$, a single skyrmion is unstable toward a tube-like object, and at high $h/J \gtrsim 1.10$ toward the paramagnetic state. (b) Phase diagram of the system at zero temperature, with helical, triangular skyrmion crystal, and paramagnetic state ($h_{\rm HS}/J \simeq 0.29$ and $h_{\rm SP}/J \simeq 0.69$, below which a single skyrmion gains an energy). (c) Energy densities of triangular skyrmion crystal states (with various densities) and helical states (with various winding numbers). The color represents the skyrmion densities for skyrmion crystal states, and the square of winding densities for helical states, respectively. Square skyrmion crystals always have higher energies than the triangular skyrmion crystal state of the lowest energy. The skyrmion crystal states with low densities are unstable below $h/J \simeq 0.50$, where a single skyrmion instability emerges.

configuration, where all of the spins are parallel to the magnetic field, is always $O(1)$, independent of the system size. While a skyrmion costs an energy when $h/J \gtrsim 0.69$, it is locally stable up to $h/J \simeq 1.10$, see Fig. 11.2 (a). Below $h/J \simeq 0.69$, to put a single skyrmion gains an energy compared to the paramagnetic state, and it is stable down to $h/J \simeq 0.50$ below which the skyrmion is transformed into a tube-like object (Fig. 11.2 (a)).

As a skyrmion is a stable vortex and two skyrmions do not annihilate each other, we can consider skyrmions as particles interacting through an effective interaction. We calculate an effective interaction $V_{\rm eff}(r)$ between two skyrmions as an extra energy to put them at distance $r$. The energy is minimized by using the zero-temperature heat-bath algorithm with two fixed spins at a center of each skyrmion. Two skyrmions interact with each other through purely repulsive, and exponentially decaying small interaction, see Fig. 11.1. An effective radius of each skyrmion estimated by exponential fitting of the interaction decreases with increasing the magnetic field. By comparing the energy gain below $h_{\rm SP}/J$ of a single skyrmion and the effective interaction of two skyrmions, the skyrmion density increases with decreasing the magnetic field.

Below $h/J \simeq 0.69$, referred to as $h_{\rm SP}/J$ in the following, the triangular skyrmion crystal states have lower energies than the paramagnetic state. The point below which a single skyrmion gains an energy corresponds to the transition magnetic field between the skyrmion crystal and the paramagnetic phase, see Fig. 11.2 (b). The density of the skyrmion crystal state with the lowest energy gets higher with decreasing $h/J$ predicted by the above discussion of the effective interaction. Skyrmions are stabilized by the mutual repulsive interaction. Indeed, while crystal states with low skyrmion density gets unstable below $h/J \simeq 0.5$, where a single skyrmion becomes unstable, high-density skyrmion crystal states are stable down to very low magnetic field. Between $h_{\rm HS}/J \simeq 0.29$ and $h_{\rm SP}/J$, the triangular skyrmion crystal states thus has the lowest energy, and below $h_{\rm HS}/J$ the helical state is the ground state, see Fig. 11.2 (b).

Due to the underlying square spin lattice, a weak coupling exists between a position of each skyrmion and the underlying spin lattice (we detail in the next section). By interpreting skyrmions in our system as interacting particles in a square periodic substrate, skyrmions in our system may have a square-lattice structure commensurate to the underlying lattice in the low density region just below $h_{\rm SP}/J$ [157, 159]. However, square-lattice skyrmion crystals always have higher energy than triangular lattice crystals. The size of skyrmion is $\sim 8$ times larger than the lattice spacing of spins, and thus a triangular lattice structure can adjust to the substrate potential with a minimal distortion and a small energy cost. Therefore, the triangular skyrmion crystal states, which is the closest packing structure for isotropic particles, are the ground state even near $h_{\rm SP}/J$.

## 11.2 Magnetic Phase diagram at finite temperature

Our model, at finite temperature, has three phases at finite temperature (Fig. 11.3); the paramagnetic phase with all short-range correlations; the skyrmion solid phase with a long-range orientational and a quasi-long-range positional correlations; the helical phase with a long-range directional correlation. We should notice in the phase diagram that the skyrmion crystal phase, which has a long-range positional correlation, does not exist at finite temperature. Also, with our interpretations of skyrmions as particles, the phase boundaries are largely changed from the conventional phase diagram of the two-dimensional chiral magnet, see, for example, [134, 140, 149, 150]: Phase transition temperature between the paramagnetic and skyrmion solid phases are reduced, and the phase boundary between them has an anomalous positive slope in a small region of the phase

boundary, see Fig. 11.3. We will show and discuss our Monte Carlo results in the next section.

### 11.2.1 Paramagnetic–Helical phase transition

Before proceeding with the skyrmions at finite temperature, we discuss a phase transition between the paramagnetic and helical phases. In the helical phase, the helical structure with one of two directions $\pm\pi/4$ is dominant over the system while both directions appear with the same probability. With increasing temperature, two helical structures are mixed in the system. At $h/J = 0.1$, the Binder parameter of the directional order $U_L$

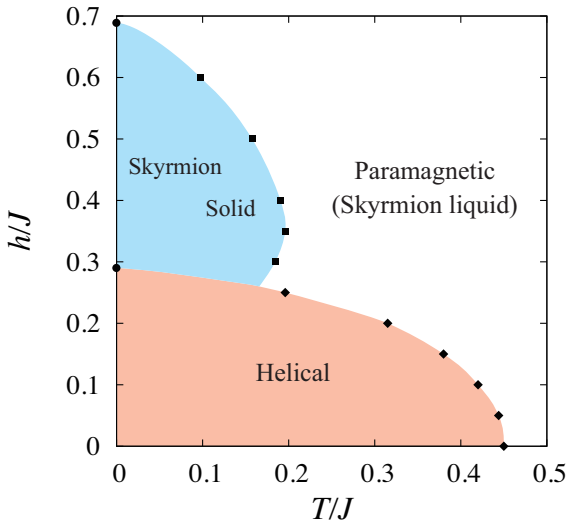


Fig. 11.3: Magnetic phase diagram of the two-dimensional chiral magnet. The circles are obtained by the zero-temperature energy minimizations. The squares are obtained by decays of correlation functions, and the diamonds denote peak locations of the specific heat obtained by finite-temperature Monte Carlo simulations at each magnetic field.

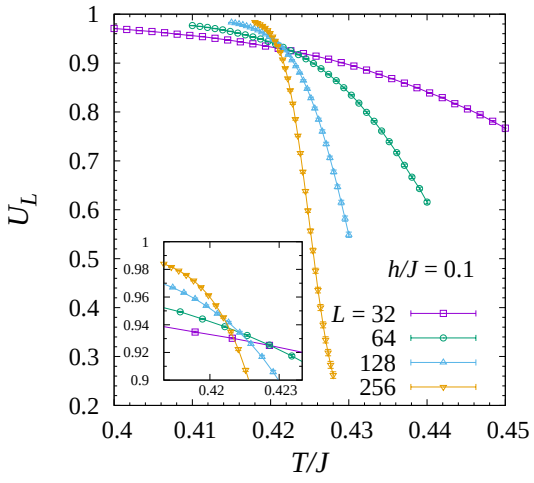


Fig. 11.4: The Binder parameter $U_L$ of the directional order parameter for various system sizes $L = 32, 64, 128$ and 256. The magnetic field $h/J = 0.1$. Inset shows a detailed view around the intersection.

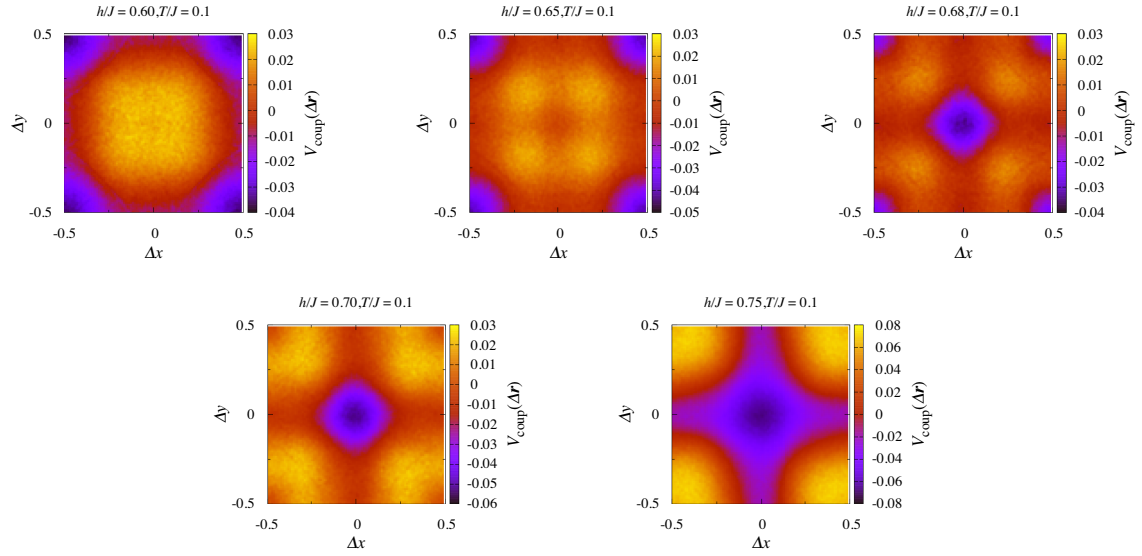


Fig. 11.5: Effective coupling potential $V_{\mathrm{coup}}(\Delta \boldsymbol{r})$ characterizing the coupling between skyrmion positions and lattice sites. For $h/J \gtrsim 0.68$, the potential minimum coincides with the lattice sites ($\Delta x = \Delta y = 0$), but at smaller magnetic field, the minimum lies between the lattice spins, at $\Delta x = \Delta y = 0.5$.

has an intersection at temperature $T/J \simeq 0.42$, see Fig. 11.4. A finite-size scaling analysis with the form

$$U_L = F\left[\left(\frac{T - T_{\mathrm{c}}}{J}\right) L^{1/\nu}\right] \tag{11.1}$$

yields $T_{\mathrm{c}}/J = 0.42043(6)$ and $\nu = 1.06(2)$. The critical exponent of the correlation length $\nu$ is marginally consistent with the two-dimensional ferromagnetic Ising universality class. We obtain at $h/J = 0$ with the same scaling form $T_{\mathrm{c}}/J = 0.44797(7)$ and $\nu = 1.06(2)$, and thus the phase transition between the paramagnetic and the helical phases belongs to the same universality class independent of $h/J$.

## 11.3 Skyrmions at finite temperature

### 11.3.1 Coupling potential between skyrmions and lattice sites

As mentioned in the previous section, skyrmions have a weak but finite coupling to the spin lattice. We compute the coupling potential between skyrmion positions and spin lattice sites using the skyrmion locator of Eq. (10.6). We simulate one single skyrmion in the system with $16 \times 16$ spins at $T/J = 0.1$ to obtain a histogram of the skyrmion locations

$$P(\Delta \boldsymbol{r}) = \left\langle \delta\left(\Delta \boldsymbol{r} - \min_k \left(\boldsymbol{R}_{\mathrm{sk}} - \boldsymbol{\ell}_k\right)\right)\right\rangle,$$

where the bracket $\langle \cdots \rangle$ represents average over configurations with only one skyrmion, and $\boldsymbol{\ell}_k$ represents the location of $k$-th lattice site. We checked that the coupling potential is independent of the system size. The coupling potential is estimated as a free-energy ratio $V_{\mathrm{coup}}(\Delta \boldsymbol{r}) = -\log\left(P(\Delta \boldsymbol{r})\right)/\beta$. Fig. 11.5 shows $V_{\mathrm{coup}}(\Delta \boldsymbol{r})$ at various magnetic fields. The potential is clearly finite, and the potential minimum depends on the magnetic field (see Fig. 11.5). The coupling potential and the effective interaction between skyrmions

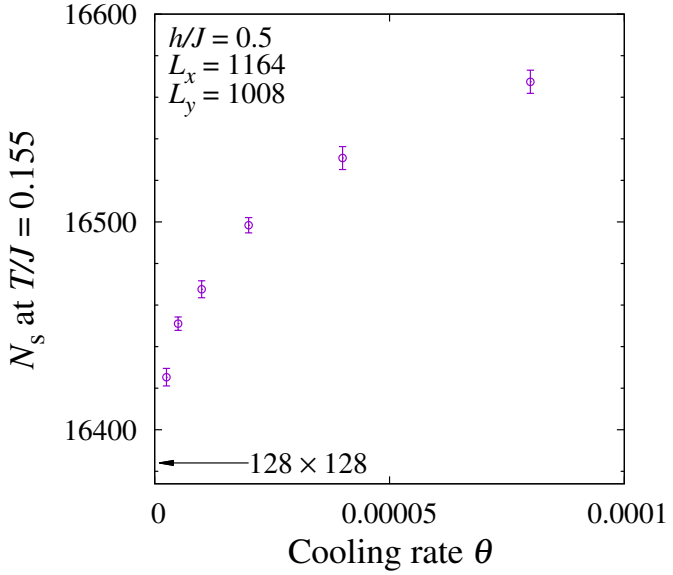


Fig. 11.6: Cooling-rate dependence of the number of skyrmions in configurations at $T/J = 0.155$ obtained by simulated annealing simulations from a high temperature. The magnetic field $h/J = 0.5$. The leftmost point $\theta = 0$ corresponds to the equilibrium limit.

(Fig. 11.1) clearly shows that the correct interpretation of skyrmions in our system is particles in a square periodic substrate with a short-range repulsive interaction.

### 11.3.2 Thermodynamic dominant number of skyrmions

At $h/J = 0.5$, the number of skyrmions $N_\mathrm{s}$ at $T/J = 0.155$ decreases with decreasing the cooling rate of the simulated annealing runs discussed in Section 10.5. For the system with $L_x = 1164 = 97 \times 12$ and $L_y = 1008 = 84 \times 12$, the number $N_\mathrm{s}$ approaches $128 \times 128$ in the limit $\theta \to 0$, see Fig. 11.6. We thus estimate the thermodynamic dominant number of skyrmions as $N_\mathrm{s} = 128 \times 128$ in the system. The same limiting density of skyrmions is also obtained for smaller systems with $(L_x, L_y) = (582, 504)$ and $(291, 252)$. We note that, at $h/J = 0.5$, the obtained limiting density corresponds to the skyrmion density in the ground state.

### 11.3.3 Low-temperature phase

In our production simulations to compute physical quantities, we keep the number of skyrmions to the estimated value with a specialized Monte Carlo algorithm implemented on GPU (see Section 10.5 and 10.6). At $T/J = 0.155$, scatter plot of the global orientation order parameter $\Psi_6$ has some "lobes". Each lobe corresponds to slight rearrangements of the skyrmions with respect to the periodic simulation box: Each row of skyrmions in configurations in the lobe at $\mathrm{Im}\Psi_6 \simeq 0$ goes back to itself with the periodic boundary, and that in the other lobes goes to another row. Those lobes imply a long-range correlation in the orientational order parameter. Indeed, the correlation function of the orientational order $g_6(r)$ at $T/J = 0.155$ decays to a finite value, which means a long-range ordering of $\Psi_6$, see Fig. 11.7. At this temperature, the two-dimensional correlation function $g(\boldsymbol{\Delta r})$ averaged over the configurations independent of the value of $\Psi_6$ has a triangular lattice structure at short distance, which derives from the long-range correlation of $\Psi_6$. How-

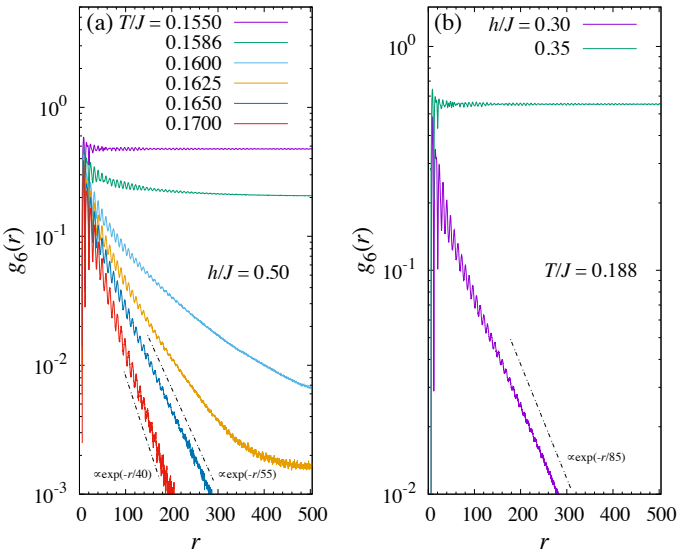


Fig. 11.7: Correlation function of the orientational order $g_6(r)$ of the system with $L_x = 1164$ and $L_y = 1008$ at various temperatures. The magnetic field is (a) $h/J = 0.5$, and (b) $h/J = 0.30$ and 0.35.

ever, a one-dimensional cut of the two-dimensional correlation function $g(x,0) - 1$ decays slightly faster than an algebraic decay, that suggests an exponential decay with a long but finite correlation length.

The long-range correlation in the orientational order and the short-range correlation in the positional order contradict each other at first sight. We thus analyze the positional correlation function for each lobe. In the center lobe at $|\mathrm{Im}\Psi_6| \simeq 0$, the one-dimensional cut of the two-dimensional positional correlation $g(x,0) - 1$ clearly decays algebraically with an exponent $\simeq 0.5$, see Fig. 11.8 (e). On the other hand, in the other lobes, the positional correlation function $g(x,0) - 1$ appears to decay faster than an algebraic decay, which can be seen markedly in the lobe that has $|\mathrm{Im}\Psi_6| \gtrsim 0.1$, see Fig. 11.8 (c). However, this is an artifact due to the slight distortion of the correlation peaks near the $x$ axis that do not lie on the $x$ axis unlike the center lobe, see inset of Fig. 11.8 (b)–(d). This is caused by the mismatch between the locally triangular structure with large $|\mathrm{Im}\Psi_6|$ and the simulation box, i.e. the underlying spin lattice. When the peaks are not located on the $x$ axis, the naive one-dimensional cut of the two-dimensional positional correlation $g(x,0) - 1$ does not give the correct correlation. The correct positional correlation function, the maximum values for all peaks near the $x$ axis, determined individually, indeed decay algebraically for all the lobes (see black open symbols in Fig. 11.8 (b)–(d)). Therefore we conclude that the positional correlation function at $T/J = 0.155$ decays algebraically with an exponent 0.5. Note that the exponent 0.5 is larger than the stability limit 1/3 of a two-dimensional solid predicted by the KTHNY theory [157, 159]. Their theory relies on the continuous symmetry of particle models. On the other hand, our system has no continuous symmetry, and each position of skyrmions has small but finite coupling to the lattice sites as discussed in Section 11.3.1. This coupling can be considered as an effective periodic potential incommensurate to the skyrmion solid that stabilizes the solid phase with a larger exponent than that observed in particle systems. A larger exponent was also reported in an experimental work on a melting transition of atoms on a two-dimensional periodic substrate [174].

The conventional understanding of the low temperature phase of two-dimensional chiral

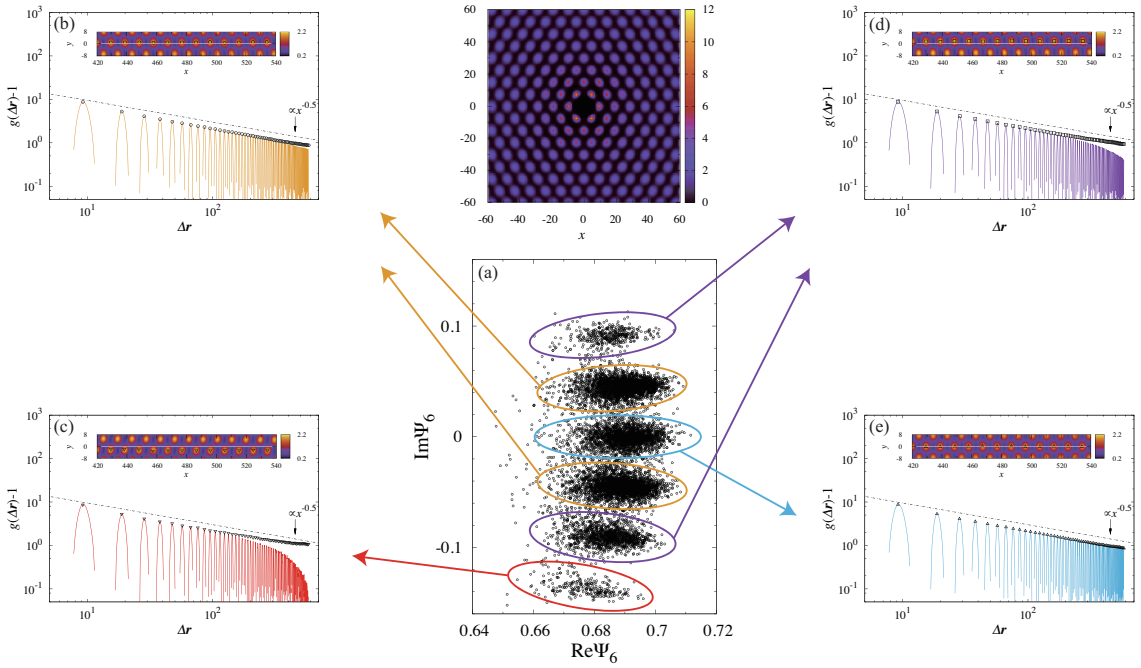


Fig. 11.8: (a) Scatter plot of the global orientational order parameter $\Psi_6$, and the two-dimensional pair correlation function at short distance. (b)–(e) Positional correlation function $g(\boldsymbol{\Delta r}) - 1$ for each lobe of the scatter plot. Solid lines represent $g(x, 0) - 1$ and black open symbols (circles in (b), inverted triangles in (c), etc.) represent the maximum value of each peak in the two-dimensional correlation function $g(x, y)$. Insets in (b)–(e) show the two-dimensional correlation function $g(x, y)$ near the $x$ axis (compare with (a)). The white line is the $x$ axis along which $g(x, 0) - 1$ is plotted. Black open symbols again represent local maxima. The system is $L_x = 1164$ and $L_y = 1008$ at $T/J = 0.155$ and $h/J = 0.5$.

magnets has stated that skyrmions form a crystal. However, our results clearly show that skyrmions in the two-dimensional chiral magnet form a two-dimensional solid, which has a long-range orientational correlation and a quasi-long-range positional correlation, rather than a crystal. With the interpretation of skyrmions as point particles, our results are consistent with the KTHNY theory for particle models on a weak incommensurate periodic substrate [157, 159].

### 11.3.4 Melting of skyrmions

With increasing temperature, the skyrmion solid state melts into the skyrmion liquid state. The liquid phase, as discussed in Section 9.2.1, has short-range correlations in both the orientational and the positional orders. The skyrmion solid and liquid phases can be directly visualized using a color representation of a phase of the local orientational order, see Fig. 11.9. Towards the transition temperature from below, we observe a decrease of the asymptotic correlation of the orientational order. From the opposite side, i.e. from the liquid phase, a very rapid increase of the orientational correlation length towards a value comparable to the system size $L$ (for example at $h/J = 0.5$, see Fig. 11.7(a), where the transition temperature is estimated as $T/J \simeq 0.16$). Analogous behavior is found for all other values of $h/J$ with a solid–liquid transition. Unlike for the two-dimensional particle models, but in agreement with theoretical predictions [157, 159], we find no evidence of

an intermediate hexatic phase. This is also consistent with the experimental work [174] that reports a direct melting transition from the solid to the liquid.

With increasing the magnetic field, which lowers the entropy, systems usually enters the paramagnetic phase. This also holds in our system if the magnetic field $h/J \gtrsim 0.35$. However, in a small region of the phase diagram, skyrmions freeze solid with increasing the magnetic field (see Fig. 11.3). This is remarkably observed in the orientational correlation functions at a certain finite temperature, which is long ranged at higher $h/J$ while it decays exponentially at lower $h/J$ (see Fig. 11.7(b)).

Our results show that the solid–liquid transition of skyrmions is of one-step, and is a continuous transition with a growing correlation length. However, a continuous solid–liquid transition has not been known in two-dimensional particle models while a first-order one and a continuous two-step transition are observed in some models. One of the possible explanations of the temperature dependence of the correlation function of the orientational order is an existence of an intermediate hexatic phase between the solid and the liquid phases with an extremely narrow temperature range. If so, our system size is clearly not enough to observe the hexatic phase. Another possible explanation is an intermediate phase that has a finite orientational order parameter but is not solid predicted by Halperin and Nelson [157, 159]. According to their theory, the orientational order vanishes at higher transition temperature with the two-dimensional Ising anomalies. Anyway, in our system, a possible intermediate phase, if it exists, lies in a very narrow temperature range, between $T/J \simeq 0.155$ and $T/J \simeq 0.165$. A simulation of the system with an extremely large size would change our present understanding of the phase transition, but we conclude here within our Monte Carlo simulations of the model with $10^6$ Heisenberg spins that the skyrmions solid state melts into the liquid state in one step.

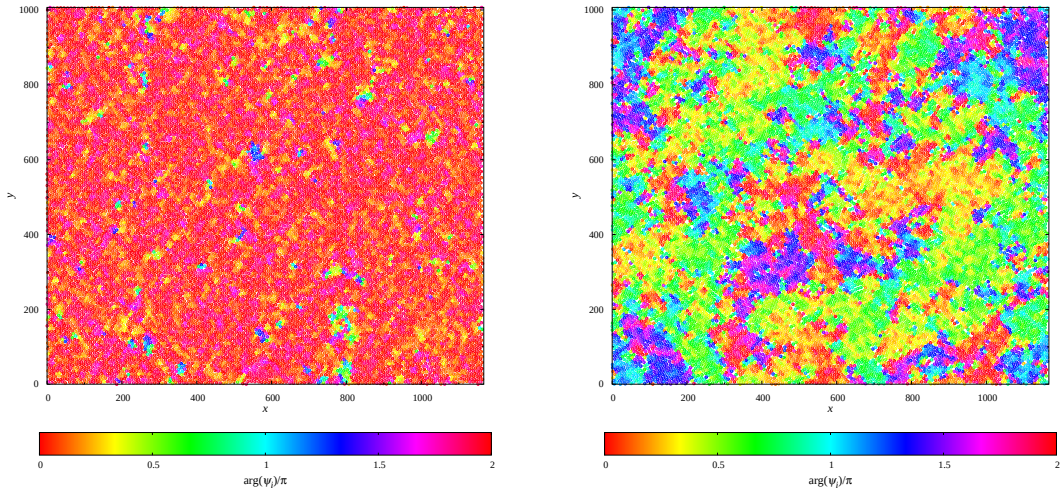


Fig. 11.9: A color representation of the argument of the local orientational order parameter $\psi_i$ of each skyrmion. The system is in the solid phase (left) and the liquid phase (right).

# 12
# Conclusion of Part III

In Part. III, we investigated a classical Heisenberg spin model of a two-dimensional chiral magnet and discussed its phase transitions. Competition between the bi-axial Dzyaloshinskii–Moriya interaction and the magnetic field induces skyrmions, thermodynamically stable vortices composed of tens of spins, into the system. At zero temperature, the system has three different phases depending on the magnetic field: The helical phase, the skyrmion crystal phase with a triangular lattice structure, and the paramagnetic phase. The helical phase and, of course, the paramagnetic phase survive at finite temperature. We proposed an order parameter, the directional order, to detect a phase transition into the helical phase, and found that the phase transition belongs to the two-dimensional ferromagnetic Ising universality class. On the other hand, the skyrmion crystal state does not exist at finite temperature, contrary to the conventional belief in the two-dimensional chiral magnet. We interpreted skyrmions as point particles, and focused on the positional and the orientational orders, which are two important order parameters in particle models. By use of a specialized Monte Carlo algorithm that preserves the number of skyrmions, and massive parallelization implemented on GPUs, we revealed with the interpretation that two-dimensional skyrmions at finite temperature form a typical two-dimensional solid without a long-range positional correlation. This skyrmion solid state melts in one step into the skyrmion liquid (which is equivalent to the paramagnetic phase) without an intermediate hexatic phase, which has been numerically proved to exist in particle models on a smooth substrate.

We showed that skyrmions can be naturally considered as particles in a periodic substrate. The typical size of each skyrmion is $\sim 8$ times larger than the underlying spin lattice, which produces the effective periodic potential. The KTHNY theory for particles in a fine mesh potential with a square-lattice shape, which are similar to skyrmions in our system, predicts the absence of the intermediate hexatic phase. While our results are consistent with the theory, the applicability of the KTHNY theory to our case is not trivial. In the two-dimensional hard disk model, the hexatic–liquid Kosterlitz–Thouless phase transition predicted by the theory is preempted by a first-order phase transition [69]. This first-order phase transition may survive in a perturbative periodic substrate as the $q$-state ferromagnetic Potts model in a weak magnetic field (with sufficiently large $q$). The KTHNY theory for a particle model in a periodic substrate is expected to hold when the model without the periodic substrate exhibits the Kosterlitz–Thouless phase transitions as predicted by the theory. Skyrmions in our model of two-dimensional chiral magnets have a very soft repulsive interaction. The scenario of the melting transitions depends on the softness of the interaction between particles [153], and thus, we can confirm our results through the effective interaction between skyrmions. For smaller but finite $D/J$, the average size of skyrmions gets larger, and the effective interaction between skyrmions becomes softer. The periodic potential emerging from the spin lattice

becomes weaker. Therefore, the situation for skyrmions in the system with smaller $D/J$ approaches to that of the KTHNY theory, and our results qualitatively hold in that case. In the limit $D/J \to 0$, however, the underlying spin lattice disappears. Skyrmions in this case should be interpreted as point particles on a smooth substrate. The two-dimensional melting scenario in a smooth substrate thus holds and the intermediate hexatic phase exists. The finite-temperature phase diagram of two-dimensional chiral magnets with finite $D/J$ differs from that of the continuum model of chiral magnets.

The KTHNY theory also predicts another phase transition at higher temperature that belongs to the two-dimensional Ising universality class for particles models on an incommensurate periodic substrate. However, we did not find any clear evidence of such a phase transition in our simulations, and the orientational correlation function decays exponentially slightly above a temperature where the system is in the skyrmion solid phase. One of the possible interpretations of our results is that the temperature range between two phase transitions is very narrow, like $\Delta T/J \sim 0.01$. To identify two phase transitions separated by such a narrow temperature range is extremely difficult for Monte Carlo simulations of the system with $\sim 10^4$ skyrmions. We expect that an effective particle model that disguises skyrmions in the two-dimensional chiral magnet allows us to see melting of skyrmions more clearly, and make our results comprehensible.

The phase diagram of the system has two ordered phases at finite temperature; the skyrmion solid phase and the helical phase. In the skyrmion solid phase, the orientational order has a long-range correlation while the directional order has a long-range correlation in the helical phase. These two order parameters characterize different symmetry of the system, and thus, the phase boundary between the two phases should be of first order. However, to confirm the expected first-order phase transition by Monte Carlo simulations is very difficult due to slow dynamics in ordered phases [*1]. A multicanonical Monte Carlo simulation [41, 42] is one of the possible methods for a direct observation of the first-order phase transition.

As discussed in Section 11.3.4, a reentrant region exists in the phase diagram with a positive slope of the phase boundary of the skyrmion solid phase. This anomalous behavior is explained in terms of the dominant number of skyrmions. With decreasing the magnetic field, the size of each skyrmions increases. Moreover, a larger number of skyrmions is favored at lower magnetic field as more skyrmions gain more entropy. These two changes with decreasing magnetic field compete, and the number of skyrmions is maximized at $h/J \simeq 0.35$. At lower magnetic field $h/J \simeq 0.30$, the size of each skyrmion becomes larger than that at $h/J \simeq 0.35$, and hence the effective interaction between skyrmions becomes softer. As softer particles with a smaller number have a lower freezing temperature than that of harder particles with a larger number, we obtain the anomalous positive slope in the phase diagram.

In our Monte Carlo simulations, the number of skyrmions is rigorously fixed by a specialized algorithm to avoid the difficulty discussed above. This strategy is invalid if the number of skyrmions strongly fluctuates at a target temperature. Fortunately, during our simulations, the fluctuation of the number is very small, and the number rarely changes. Furthermore, towards the thermodynamic limit, fluctuations in the number density will be suppressed unless temperature is exactly a first-order phase transition point. We thus expect that our strategy is valid in the sense that it gives the asymptotically correct results towards the thermodynamic limit. The difficulty to change the number of skyrmions in numerical simulations at low temperature prevents us to access high-precision data of the

[*1] In Ref. [150], they show that a first-order phase transition occurs between the ordered phases by Monte Carlo simulations of a small system with $128 \times 128$ spins while their model is slightly different from ours.

system with a large system size. Our strategy is necessary for Monte Carlo simulations of the system with more than $10^6$ spins, and obtain our results unless an efficient cluster algorithm is developed for the system.

We have considered in this work phase transitions driven by objects composed of Heisenberg spins, elementary degrees of freedom in the Hamiltonian. Collective configurations of spins determine their positions and orders, and an effective particle model emerges with the interpretation. We found in the skyrmion solid phase a quasi-long-range correlation in the positional order and a long-range correlation in the orientational order. To our knowledge, few studies have been known which reports collective objects showing a different order from that characterized by elementary degrees of the Hamiltonian. If we focus only on the spin-spin correlation function, we cannot find two distinct correlations in two different orders. In that sense, the interpretation of skyrmions as particles is essential to characterize the orders in the system and construct the phase diagram. Furthermore, the interpretation can be directly applied to experimental data. We hope our results of the two correlations in the skyrmion solid phase are testified through experiments of thin films of chiral magnets, and contribute to understanding macroscopic properties such as elastic stiffness of skyrmions [175] in thin films and their collective dynamics.

# 13 Concluding Remarks

In this thesis, we discussed Monte Carlo algorithms, implementations, and their application to two models of chiral magnets. In Part I, the event-chain algorithm is introduced. The event-chain Monte Carlo algorithm is a lifting Monte Carlo algorithm, where, by introducing an extra variable called the lifting variable, the detailed balance condition is violated yet the global balance condition is satisfied. This algorithm was originally developed in the hard sphere models, but turned out to be efficient also in continuous spin systems. In particular, for three-dimensional ferromagnetic Heisenberg model, reduction of the dynamical critical exponent is realized by the algorithm; while the exponent $z \simeq 2$ in conventional algorithms with detailed balance, $z \simeq 1$ in the event-chain algorithm. The event-chain algorithm shows us that breaking detailed balance can significantly change the dynamics at a critical point. The algorithm is numerically shown to be efficient also in a frustrated magnet. This is in contrast to the cluster algorithms: While cluster algorithms reduce the dynamical critical exponent more than the event-chain algorithm, they are useless in frustrated systems due to the discrepancy of the percolation threshold of the cluster size and the actual phase transition point. However, the event-chain algorithm does not work well for a three-dimensional Heisenberg spin glass model.

The speedup obtained by the event-chain algorithm relies on an introduction of the lifting variables. In previous works [61, 63, 176], the lifting variable that takes an $O(1)$ value has been introduced just to double the configuration space. On the other hand, in the event-chain algorithm, the lifting variable specifies a degree of freedom which will be updated, and thus takes an $O(N)$ value. This is the key ingredient to realize the collective update and maximal breaking of detailed balance in the construction of the algorithm. It would be one of guiding principles to design a lifting algorithm that induces a collective update. Breaking detailed balance will be one of the useful strategies to develop efficient Monte Carlo algorithms in the future. In particular, the lifting framework should have a large potential for the systematic design of irreversible algorithms. A possible direction for further research on Monte Carlo algorithms is to design an irreversible algorithm that realizes a collective update for models with discrete degrees of freedom. Some irreversible algorithms have been proposed for such models [63, 65, 176, 177], but none of them change the dynamics qualitatively, or reduce the dynamical critical exponent of models in finite dimensions with a phase transition at finite temperature. In these algorithms, irreversibility affects only locally, and no collective update is realized in their dynamics for the models. Irreversibility should be introduced so that a cooperative dynamics is induced to the models.

In Part. II, the three-dimensional uni-axial chiral magnet with a magnetic field considered is studied by using the event-chain Monte Carlo algorithm. Fortunately, the algorithm works quite well in the model of the three-dimensional uni-axial chiral magnet, and it allows us to equilibrate the system with more than $10^6$ spins. We found that a

phase transition belonging to the three-dimensional ferromagnetic $XY$ model occurs at weak finite magnetic field although the magnetic field breaks the continuous symmetry of the system. Another type of phase transition is found in the system with the larger magnetic field. This phase transition accompanies strong divergences of the specific heat and the uniform magnetic susceptibility. Although the system size dependences of the peak values of the specific heat and the uniform magnetic susceptibility are marginally consistent with $\sim L^3$, no double-peak structure is found in the energy density. This suggests that $L^3$ divergences derive from a different mechanism from a double-peak structure. We pointed out the similarity between the Dzyaloshinskii's theory and our results. On the other hand, mean-field studies [107–110] show that a first-order phase transition can occur with a finite magnetic field. Our results on this phase transition and the phase diagram are not decisive. Further theoretical studies, such as finite-size scaling theory of nucleation-type continuous transition, would help us to comprehend our results.

In Part III, we study the two-dimensional chiral magnet with bi-axial DM interaction by massively parallelized Monte Carlo simulations implemented on GPUs. Skyrmions emerge in the model with a magnetic field at low temperature as stable vortices composed of many spins. The zero-temperature phase diagram is identified by energy minimization of various skyrmion crystals and helical states. As a result, a triangular skyrmion crystal state with a long-range positional correlation is the ground state in a finite region of the magnetic field. At finite temperature, we interpret skyrmions as point particles. With this interpretation, the system can be regarded as repulsive particle models with a square-lattice periodic substrate. We simulate a large system with $10^6$ spins and $10^4$ skyrmions, and compute the correlation functions of the orientational and the positional orders. At low temperature, skyrmions form a two-dimensional solid with an algebraically decaying positional correlation and long-range correlation in the orientational order. The triangular skyrmion crystal state at zero temperature is not stable at finite temperature. We also find the solid state melts into a liquid phase, equivalent to the paramagnetic phase, in one step. This is consistent with the Kosterlitz–Thouless–Halperin–Nelson–Young (KTHNY) theory for particles in a weak incommensurate periodic potential. Nevertheless, the KTHNY prediction is not completely applied to our model just above the melting temperature. A possible reason of the difference is the softness of skyrmions: As each skyrmion consists of many spins, skyrmions might be considered as a particle with internal degrees of freedom. Another reason is the fineness of the underlying lattice compared to the size of each skyrmion. The detailed analysis of the theory and our results may be comprehensible from these points of view.

The concept of the universality, which has been one of the celebrated achievements in modern physics for decades, is essential to understand continuous phase transitions. However, the universality of phase transitions in systems with low symmetry has been still less understood. In both of our models of chiral magnets, the Hamiltonians have no symmetry in the spin space, and only discrete symmetry coupled with the transformation of the spin lattice exists. Therefore, we cannot estimate what kind of phase transition is possible in the systems a priori. As demonstrated in Part II and III, both systems indeed show extremely nontrivial phase transitions, which are not expected to occur by the symmetry of their Hamiltonians. The Landau theory based on the concept of spontaneous symmetry breaking cannot be directly applied to systems with very low symmetry. We thus expect a phase transition beyond the Landau theory is possible in such systems.

Through this thesis, we have used an appropriate Monte Carlo strategy for each situation. While the event-chain algorithm worked efficiently in the model of uni-axial chiral magnets (Part II), it is not efficient for the model of bi-axial chiral magnets (Part III). Massive parallelization of a local Monte Carlo algorithm greatly helps equilibration in a short time measured in the wall clock time in the latter model. We have to design an ap-

propriate approach for each system we are interested in to minimize a real time to obtain the correct results. Numerical simulations are dangerous in the sense we obtain wrong results unless we are extremely careful. What we have to do in numerical simulations is to try to understand each system profoundly rather than simulate it naively using general algorithms. A deep understanding of each system may provide us a new numerical approach to each system, and, a new numerical approach provides us a new insight into the system. I believe that "good" algorithm and implementation can change our conventional understandings of physics.

# References


[1] N. Metropolis, A. W. Rosenbluth, M. N. Rosenbluth, A. H. Teller, and E. Teller, "Equation of State Calculations by Fast Computing Machines", J. Chem. Phys. **21**, 1087 (1953).

[2] B. J. Alder and T. E. Wainwright, "Phase Transition for a Hard Sphere System", J. Chem. Phys. **27**, 1208 (1957).

[3] L. Onsager, "Crystal Statistics. I. A Two-Dimensional Model with an Order-Disorder Transition", Phys. Rev. **65**, 117 (1944).

[4] Y. Nishikawa, M. Michel, W. Krauth, and K. Hukushima, "Event-chain algorithm for the Heisenberg model: Evidence for z$\simeq$1 dynamic scaling", Phys. Rev. E **92**, 063306 (2015).

[5] Y. Nishikawa and K. Hukushima, "Event-chain Monte Carlo algorithm for continuous spin systems and its application", J. Phys. Conf. Ser. **750**, 012014 (2016).

[6] Y. Nishikawa and K. Hukushima, "Phase transitions and ordering structures of a model of a chiral helimagnet in three dimensions", Phys. Rev. B **94**, 064428 (2016).

[7] Y. Nishikawa, K. Hukushima, and W. Krauth, "Solid–liquid transition of skyrmions in a two-dimensional chiral magnet", arXiv:1710.11095 (2017).

[8] D. Levin, Y. Peres, and E. L. Wilmer, *Markov chains and mixing times* (American Mathematical Society, Providence, 2009).

[9] M. Michel, "Irreversible Markov chains by the factorized Metropolis filter: Algorithms and applications in particle systems and spin models", Thèses (Ecole Normale Supérieure de Paris - ENS Paris, Oct. 2016).

[10] A. Sokal, "Monte carlo methods in statistical mechanics: foundations and new algorithms", in *Functional integration: basics and applications*, edited by C. DeWitt-Morette, P. Cartier, and A. Folacci (Springer US, Boston, MA, 1997), pp. 131–192.

[11] M. Dyer, A. Sinclair, E. Vigoda, and D. Weitz, "Mixing in time and space for lattice spin systems: A combinatorial view", Rand. Struct. Algor. **24**, 461 (2004).

[12] E. Lubetzky and A. Sly, "Critical Ising on the Square Lattice Mixes in Polynomial Time", Commun. Math. Phys. **313**, 815 (2012).

[13] P. Peczak and D. P. Landau, "Dynamical critical behavior of the three-dimensional Heisenberg model", Phys. Rev. B **47**, 14260 (1993).

[14] L. M. Jensen, B. J. Kim, and P. Minnhagen, "Dynamic critical exponent of two-, three-, and four-dimensional XY models with relaxational and resistively shunted junction dynamics", Phys. Rev. B **61**, 15412 (2000).

[15] J. Liu and E. Luijten, "Rejection-Free Geometric Cluster Algorithm for Complex Fluids", Phys. Rev. Lett. **92**, 035504 (2004).

[16] M. Matsumoto, K. Hukushima, and H. Takayama, "Dynamical critical phenomena in three-dimensional Heisenberg spin glasses", Phys. Rev. B **66**, 104404 (2002).

[17] B. I. Halperin, "Rigorous Inequalities for the Spin-Relaxation Function in the Kinetic Ising Model", Phys. Rev. B **8**, 4437 (1973).

[18] K. Kawasaki, "Diffusion Constants near the Critical Point for Time-Dependent Ising Models. II", Phys. Rev. **148**, 375 (1966).

[19] X.-J. Li and A. D. Sokal, "Rigorous lower bound on the dynamic critical exponents of the Swendsen-Wang algorithm", Phys. Rev. Lett. **63**, 827 (1989).
[20] X.-J. Li and A. D. Sokal, "Rigorous lower bound on the dynamic critical exponent of some multilevel Swendsen-Wang algorithms", Phys. Rev. Lett. **67**, 1482 (1991).
[21] W. Janke, "Introduction to simulation techniques", in *Ageing and the glass transition*, edited by M. Henkel, M. Pleimling, and R. Sanctuary (Springer Berlin Heidelberg, Berlin, Heidelberg, 2007), pp. 207–260.
[22] M. Weigel, "Simulating spin models on GPU", Comput. Phys. Commun. **182**, 1833 (2011).
[23] M. Weigel, "Performance potential for simulating spin models on GPU", J. Comput. Phys. **231**, 3064 (2012).
[24] M. Engel, J. A. Anderson, S. C. Glotzer, M. Isobe, E. P. Bernard, and W. Krauth, "Hard-disk equation of state: First-order liquid-hexatic transition in two dimensions with three simulation methods", Phys. Rev. E **87**, 042134 (2013).
[25] J. A. Anderson, E. Jankowski, T. L. Grubb, M. Engel, and S. C. Glotzer, "Massively parallel monte carlo for many-particle simulations on GPUs", J. Comput. Phys. **254**, 27 (2013).
[26] J. A. Anderson, J. Antonaglia, J. A. Millan, M. Engel, and S. C. Glotzer, "Shape and Symmetry Determine Two-Dimensional Melting Transitions of Hard Regular Polygons", Phys. Rev. X **7**, 021001 (2017).
[27] W. K. Hastings, "Monte Carlo Sampling Methods Using Markov Chains and Their Applications", Biometrika **57**, 97 (1970).
[28] R. H. Swendsen and J.-S. Wang, "Nonuniversal Critical Dynamics in Monte Carlo Simulations", Phys. Rev. Lett. **58**, 86 (1987).
[29] U. Wolff, "Collective Monte Carlo Updating for Spin Systems", Phys. Rev. Lett. **62**, 361 (1989).
[30] U. Wolff, "Comparison between cluster Monte Carlo algorithms in the Ising model", Phys. Lett. B **228**, 379 (1989).
[31] C. Fortuin and P. Kasteleyn, "On the random-cluster model I. Introduction and relation to other models", Physica **57**, 536 (1972).
[32] C. Fortuin, "On the random-cluster model II. The percolation model", Physica **58**, 393 (1972).
[33] C. Fortuin, "On the random-cluster model III. The simple random-cluster model", Physica **59**, 545 (1972).
[34] C. Dress and W. Krauth, "Cluster algorithm for hard spheres and related systems", J. Phys. A **28**, L597 (1995).
[35] A. Buhot and W. Krauth, "Numerical Solution of Hard-Core Mixtures", Phys. Rev. Lett. **80**, 4 (1998).
[36] L. Santen and W. Krauth, "Absence of Thermodynamic Phase Transition in a Model Glass Former", Nature **405**, 550 (1999).
[37] A. Jaster, "An improved Metropolis algorithm for hard core systems", Physica A **264**, 134 (1999).
[38] H. Kawamura, A. Yamamoto, and T. Okubo, "$Z_2$-vortex ordering of the triangular-lattice Heisenberg antiferromagnet", J. Phys. Soc. Jpn. **79**, 28 (2010).
[39] L. Wang, "Exploring cluster Monte Carlo updates with Boltzmann machines", Phys. Rev. E **96**, 051301 (2017).
[40] C. Holm and W. Janke, "Critical exponents of the classical three-dimensional Heisenberg model: A single-cluster Monte Carlo study", Phys. Rev. B **48**, 936 (1993).
[41] B. A. Berg and T. Neuhaus, "Multicanonical algorithms for first order phase transitions", Phys. Lett. B **267**, 249 (1991).

[42] B. A. Berg and T. Neuhaus, "Multicanonical ensemble: A new approach to simulate first-order phase transitions", Phys. Rev. Lett. **68**, 9 (1992).
[43] Y. Iba, "Extended Ensemble Monte Carlo", Int. J. Mod. Phys. C **12**, 623 (2001).
[44] F. Wang and D. P. Landau, "Determining the density of states for classical statistical models: A random walk algorithm to produce a flat histogram", Phys. Rev. E **64**, 056101 (2001).
[45] F. Wang and D. P. Landau, "Efficient, Multiple-Range Random Walk Algorithm to Calculate the Density of States", Phys. Rev. Lett. **86**, 2050 (2001).
[46] C. Geyer, "Markov chain monte carlo maximum likelihood", in Computing science and statistics: proceedings of the 23rd symposium on the interface, edited by E. M. Keramidas (1991), p. 156.
[47] C. J. Geyer and E. A. Thompson, "Annealing markov chain monte carlo with applications to ancestral inference", J. Am. Stat. Assoc. **90**, 909 (1995).
[48] K. Hukushima and K. Nemoto, "Exchange Monte Carlo method and application to spin glass simulations", J. Phys. Soc. Jpn. **65**, 1604 (1996).
[49] Y. Sugita and Y. Okamoto, "Replica-exchange molecular dynamics method for protein folding", Chem. Phys. Lett. **314**, 141 (1999).
[50] K. Hukushima, "Domain-wall free energy of spin-glass models: Numerical method and boundary conditions", Phys. Rev. E **60**, 3606 (1999).
[51] K. Hukushima and H. Kawamura, "Chiral-glass transition and replica symmetry breaking of a three-dimensional Heisenberg spin glass", Phys. Rev. E **61**, R1008 (2000).
[52] R. Yamamoto and W. Kob, "Replica-exchange molecular dynamics simulation for supercooled liquids", Phys. Rev. E **61**, 5473 (2000).
[53] L. W. Lee and A. P. Young, "Single spin and chiral glass transition in vector spin glasses in three dimensions.", Phys. Rev. Lett. **90**, 227203 (2003).
[54] L. W. Lee and A. P. Young, "Large-scale Monte Carlo simulations of the isotropic three-dimensional Heisenberg spin glass", Phys. Rev. B **76**, 1 (2007).
[55] D. Larson, H. G. Katzgraber, M. A. Moore, and A. P. Young, "Numerical studies of a one-dimensional three-spin spin-glass model with long-range interactions", Phys. Rev. B **81**, 064415 (2010).
[56] M. Ozawa, W. Kob, A. Ikeda, and K. Miyazaki, "Equilibrium phase diagram of a randomly pinned glass-former", Proc. Natl. Acad. Sci. USA **112**, 6914 (2015).
[57] R. H. Swendsen and J.-S. Wang, "Replica Monte Carlo Simulation of Spin-Glasses", Phys. Rev. Lett. **57**, 2607 (1986).
[58] J.-S. Wang and R. H. Swendsen, "Replica Monte Carlo Simulation (Revisited)", Prog. Theor. Phys. Supp. **157**, 317 (2005).
[59] V. I. Manousiouthakis and M. W. Deem, "Strict detailed balance is unnecessary in Monte Carlo simulation", J. Chem. Phys. **110**, 2753 (1999).
[60] P. Diaconis, S. Holmes, and R. M. Neal, "Analysis of a nonreversible Markov chain sampler", Ann. Appl. Probab. **10**, 726 (2000).
[61] F. Chen, L. Lovász, and I. Pak, "Lifting Markov chains to speed up mixing", in Proceedings of the thirty-first annual ACM symposium on Theory of computing - STOC '99 (1999), pp. 275–281.
[62] K. Ramanan and A. Smith, "Bounds on Lifting Continuous-State Markov Chains to Speed Up Mixing", J. Theor. Prob., 1 (2017).
[63] K. S. Turitsyn, M. Chertkov, and M. Vucelja, "Irreversible Monte Carlo algorithms for efficient sampling", Physica D **240**, 410 (2011).
[64] K. Hukushima and Y. Sakai, "An irreversible Markov-chain Monte Carlo method with skew detailed balance conditions", J. Phys. Conf. Ser. **473**, 012012 (2013).

[65] H. Suwa and S. Todo, "Markov Chain Monte Carlo Method without Detailed Balance", Phys. Rev. Lett. **105**, 120603 (2010).
[66] S. Todo and H. Suwa, "Geometric allocation approaches in Markov chain Monte Carlo", J. Phys. Conf. Ser. **473**, 012013 (2013).
[67] E. P. Bernard, W. Krauth, and D. Wilson, "Event-chain Monte Carlo algorithms for hard-sphere systems", Phys. Rev. E **80**, 056704 (2009).
[68] M. Isobe and W. Krauth, "Hard-sphere melting and crystallization with event-chain Monte Carlo", J. Chem. Phys. **143** (2015).
[69] E. P. Bernard and W. Krauth, "Two-Step Melting in Two Dimensions: First-Order Liquid-Hexatic Transition", Phys. Rev. Lett. **107**, 155704 (2011).
[70] E. P. Bernard and W. Krauth, "Addendum to "Event-chain Monte Carlo algorithms for hard-sphere systems"", Phys. Rev. E **86**, 017701 (2012).
[71] E. A. J. F. Peters and G. de With, "Rejection-free Monte Carlo sampling for general potentials", Phys. Rev. E **85**, 026703 (2012).
[72] M. Michel, S. C. Kapfer, and W. Krauth, "Generalized event-chain Monte Carlo: constructing rejection-free global-balance algorithms from infinitesimal steps", J. Chem. Phys. **140**, 054116 (2014).
[73] A. Bortz, M. Kalos, and J. Lebowitz, "A new algorithm for Monte Carlo simulation of Ising spin systems", J. Comput. Phys. **17**, 10 (1975).
[74] H. Kawamura and S. Miyashita, "Phase Transition of the Two-Dimensional Heisenberg Antiferromagnet on the Triangular Lattice", J. Phys. Soc. Jpn. **53**, 4138 (1984).
[75] Z. Lei and W. Krauth, "Irreversible Markov chains in spin models: Topological excitations", arXiv:1711.08375 (2017).
[76] K. Hukushima and H. Kawamura, "Monte Carlo simulations of the phase transition of the three-dimensional isotropic Heisenberg spin glass", Phys. Rev. B **72**, 144416 (2005).
[77] H. Kawamura, "Monte Carlo Study of Chiral-Glass Ordering in Three-Dimensional Heisenberg Spin Glass", J. Phys. Soc. Jpn. **64**, 26 (1995).
[78] D. X. Viet and H. Kawamura, "Monte Carlo studies of chiral and spin ordering of the three-dimensional Heisenberg spin glass", Phys. Rev. B **80**, 064418 (2009).
[79] D. X. Viet and H. Kawamura, "Spin-Chirality Decoupling in the One-Dimensional Heisenberg Spin Glass with Long-Range Power-Law Interactions", Phys. Rev. Lett. **105**, 097206 (2010).
[80] L. A. Fernandez, V. Martin-Mayor, S. Perez-Gaviro, A. Tarancon, and A. P. Young, "Phase transition in the three dimensional Heisenberg spin glass: Finite-size scaling analysis", Phys. Rev. B **80**, 024422 (2009).
[81] M. Michel, J. Mayer, and W. Krauth, "Event-chain Monte Carlo for classical continuous spin models", Europhys. Lett. **112**, 20003 (2015).
[82] E. Domany, M. Schick, and R. H. Swendsen, "First-Order Transition in an $xy$ Model with Nearest-Neighbor Interactions", Phys. Rev. Lett. **52**, 1535 (1984).
[83] H. W. J. Blöte, W. Guo, and H. J. Hilhorst, "Phase Transition in a Two-Dimensional Heisenberg Model", Phys. Rev. Lett. **88**, 047203 (2002).
[84] K. Aoyama and H. Kawamura, "Spin-lattice-coupled order in heisenberg antiferromagnets on the pyrochlore lattice", Phys. Rev. Lett. **116**, 257201 (2016).
[85] H. Yoshino, "Rotational glass transitions and jamming without quenched disorder in a large dimensional limit", arXiv:1704.01216 (2017).
[86] L. Berthier, G. Biroli, J.-P. Bouchaud, L. Cipelletti, and W. van Saarloos, eds., *Dynamical Heterogeneities in Glasses, Colloids, and Granular Media* (Oxford University Press, 2011).

[87] L. Berthier and G. Biroli, "Theoretical perspective on the glass transition and amorphous materials", Rev. Mod. Phys. **83**, 587 (2011).

[88] S. C. Kapfer and W. Krauth, "Sampling from a polytope and hard-disk Monte Carlo", J. Phys. Conf. Ser. **454**, 012031 (2013).

[89] T. A. Kampmann, H.-H. Boltz, and J. Kierfeld, "Parallelized event chain algorithm for dense hard sphere and polymer systems", J. Comput. Phys. **281**, 864 (2015).

[90] I. E. Dzyaloshinskii, "Theory of Helicoidal Structures in Antiferromagnets. I. Nonmetals", Sov. Phys. JETP **19**, 960 (1964).

[91] I. E. Dzyaloshinskii, "Theory of Helicoidal Structures in Antiferromagnets. II. Metals", Sov. Phys. JETP **20**, 223 (1964).

[92] I. E. Dzyaloshinskii, "Theory of Helicoidal Structures in Antiferromagnets. III.", Sov. Phys. JETP **20**, 665 (1965).

[93] T. Moriya, "New Mechanism of Anisotropic Superexchange Interaction", Phys. Rev. Lett. **4**, 228 (1960).

[94] T. Moriya, "Anisotropic Superexchange Interaction and Weak Ferromagnetism", Phys. Rev. **120**, 91 (1960).

[95] T. Moriya and T. Miyadai, "Evidence for the helical spin structure due to antisymmetric exchange interaction in $Cr_{1/3}NbS_2$", Solid State Commun. **42**, 209 (1982).

[96] T. Miyadai, K. Kikuchi, H. Kondo, S. Sakka, M. Arai, and Y. Ishikawa, "Magnetic Properties of $Cr_{1/3}$ $NbS_2$", J. Phys. Soc. Jpn. **52**, 1394 (1983).

[97] J. Kishine, K. Inoue, and Y. Yoshida, "Synthesis, Structure and Magnetic Properties of Chiral Molecule-Based Magnets", Prog. Theor. Phys. Supp. **159**, 82 (2005).

[98] Y. Togawa, T. Koyama, K. Takayanagi, S. Mori, Y. Kousaka, J. Akimitsu, S. Nishihara, K. Inoue, A. S. Ovchinnikov, and J. Kishine, "Chiral Magnetic Soliton Lattice on a Chiral Helimagnet", Phys. Rev. Lett. **108**, 107202 (2012).

[99] Y. Togawa, Y. Kousaka, S. Nishihara, K. Inoue, J. Akimitsu, A. S. Ovchinnikov, and J. Kishine, "Interlayer Magnetoresistance due to Chiral Soliton Lattice Formation in Hexagonal Chiral Magnet", Phys. Rev. Lett. **111**, 197204 (2013).

[100] N. J. Ghimire, M. A. McGuire, D. S. Parker, B. Sipos, S. Tang, J.-Q. Yan, B. C. Sales, and D. Mandrus, "Magnetic phase transition in single crystals of the chiral helimagnet $Cr_{1/3}NbS_2$ ", Phys. Rev. B **87**, 104403 (2013).

[101] L. Zhang, D. Menzel, C. Jin, H. Du, M. Ge, C. Zhang, L. Pi, M. Tian, and Y. Zhang, "Critical behavior of the single-crystal helimagnet MnSi", Phys. Rev. B **91**, 024403 (2015).

[102] K. Tsuruta, M. Mito, H. Deguchi, J. Kishine, Y. Kousaka, J. Akimitsu, and K. Inoue, "Phase diagram of the chiral magnet $Cr_{1/3}NbS_2$ in a magnetic field", Phys. Rev. B **93**, 104402 (2016).

[103] Y. Togawa, Y. Kousaka, K. Inoue, and J. Kishine, "Symmetry, Structure, and Dynamics of Monoaxial Chiral Magnets", J. Phys. Soc. Jpn. **85**, 112001 (2016).

[104] E. M. Clements, R. Das, L. Li, P. J. Lampen-Kelley, M.-H. Phan, V. Keppens, D. Mandrus, and H. Srikanth, "Critical Behavior and Macroscopic Phase Diagram of the Monoaxial Chiral Helimagnet $Cr_{1/3}NbS_2$", Sci. Rep. **7**, 6545 (2017).

[105] J. Kishine, I. G. Bostrem, a. S. Ovchinnikov, and V. E. Sinitsyn, "Topological magnetization jumps in a confined chiral soliton lattice", Phys. Rev. B **89**, 1 (2014).

[106] B. Schaub and D. Mukamel, "Phase diagrams of systems exhibiting incommensurate structures", Phys. Rev. B **32**, 6385 (1985).

[107] V. Laliena, J. Campo, and Y. Kousaka, "Understanding the $H-T$ phase diagram of the monoaxial helimagnet", Phys. Rev. B **94**, 094439 (2016).

[108] M. Shinozaki, S. Hoshino, Y. Masaki, J. Kishine, and Y. Kato, "Finite-temperature properties of three-dimensional chiral helimagnets", J. Phys. Soc. Jpn. **85**, 074710 (2016).
[109] V. Laliena, J. Campo, and Y. Kousaka, "Nucleation, instability, and discontinuous phase transitions in monoaxial helimagnets with oblique fields", Phys. Rev. B **95**, 224410 (2017).
[110] M. Shinozaki, S. Hoshino, Y. Masaki, A. N. Bogdanov, A. O. Leonov, J. Kishine, and Y. Kato, "Fan-type spin structure in uni-axial chiral magnets", arXiv:1705.07778 (2017).
[111] P. de Gennes, *Fluctuations, Instabilities, and Phase Transitions*, edited by T. Riste (Springer US, Boston, MA, 1975).
[112] L. Klein and A. Aharony, "Crossover and multicriticality due to the Dzyaloshinsky-Moriya interaction", Phys. Rev. B **44**, 856 (1991).
[113] L. L. Liu, "Effect of Antisymmetric Interactions on Critical Phenomena: A System with Helical Ground State", Phys. Rev. Lett. **31**, 459 (1973).
[114] M. Calvo, "Exact equivalence of the Dzialoshinski-Moriya exchange interaction and quadratic spin anisotropies", J. Phys. C **14**, L733 (1981).
[115] J. Perk and H. Capel, "Antisymmetric exchange, canting and spiral structure", Phys. Lett. A **58**, 115 (1976).
[116] M. Shinozaki, "カイラルらせん磁性体の平衡状態とヒステリシスの理論 (Theory of thermodynamic states and hysteresis of chiral helimagnets)", PhD thesis (The University of Tokyo, 2018).
[117] F. Cooper, B. Freedman, and D. Preston, "Solving $\phi$1,24 field theory with Monte Carlo", Nucl. Phys. B **210**, 210 (1982).
[118] M. E. Fisher and A. Berker, "Scaling for first-order phase transitions in thermodynamic and finite systems", Phys. Rev. B **26**, 2507 (1982).
[119] K. Harada, "Bayesian inference in the scaling analysis of critical phenomena", Phys. Rev. E **84**, 056704 (2011).
[120] K. Harada, "Kernel method for corrections to scaling", Phys. Rev. E **92**, 012106 (2015).
[121] M. Campostrini, M. Hasenbusch, A. Pelissetto, P. Rossi, and E. Vicari, "Critical behavior of the three-dimensional XY universality class", Phys. Rev. B **63**, 214503 (2001).
[122] N. Schultka and E. Manousakis, "Specific heat of superfluids near the transition temperature", Phys. Rev. B **52**, 7528 (1995).
[123] K. Binder and A. P. Young, "Spin glasses: Experimental facts, theoretical concepts, and open questions", Rev. Mod. Phys. **58**, 801 (1986).
[124] A. M. Ferrenberg and R. H. Swendsen, "Optimized Monte Carlo data analysis", Phys. Rev. Lett. **63**, 1195 (1989).
[125] N. Goldenfeld, *Lectures on phase transitions and the renormalization group* (Addison-Wesley, Advanced Book Program, Reading, Mass., 1992).
[126] F. Y. Wu, "The Potts model", Rev. Mod. Phys. **54**, 235 (1982).
[127] T. Okubo, K. Oshikawa, H. Watanabe, and N. Kawashima, "Scaling relation for dangerously irrelevant symmetry-breaking fields", Phys. Rev. B **91**, 174417 (2015).
[128] F. Léonard and B. Delamotte, "Critical Exponents Can Be Different on the Two Sides of a Transition: A Generic Mechanism", Phys. Rev. Lett. **115**, 200601 (2015).
[129] H. Shinaoka, Y. Tomita, and Y. Motome, "Spin-Glass Transition in Bond-Disordered Heisenberg Antiferromagnets Coupled with Local Lattice Distortions on a Pyrochlore Lattice", Phys. Rev. Lett. **107**, 047204 (2011).

[130] H. Shinaoka, Y. Tomita, and Y. Motome, "Effect of magnetoelastic coupling on spin-glass behavior in Heisenberg pyrochlore antiferromagnets with bond disorder", Phys. Rev. B **90**, 165119 (2014).

[131] T. H. R. Skyrme, "A unified field theory of mesons and baryons", Nucl. Phys. **31**, 556 (1962).

[132] A. Bogdanov and D. A. Yablonskii, "Thermodynamically stable "vortices" in magnetically ordered crystals. The mixed state of magnets", Sov. Phys. JETP **68**, 101 (1989).

[133] A. Bogdanov and A. Hubert, "Thermodynamically stable magnetic vortex states in magnetic crystals", J. Magn. Magn. Mater. **138**, 255 (1994).

[134] N. Nagaosa and Y. Tokura, "Topological properties and dynamics of magnetic skyrmions", Nat. Nanotechnol. **8**, 899 (2013).

[135] T. Okubo, S. Chung, and H. Kawamura, "Multiple-$q$ States and the Skyrmion Lattice of the Triangular-Lattice Heisenberg Antiferromagnet under Magnetic Fields", Phys. Rev. Lett. **108**, 017206 (2012).

[136] Y. S. Lin, P. J. Grundy, and E. A. Giess, "Bubble domains in magnetostatically coupled garnet films", Appl. Phys. Lett. **23**, 485 (1973).

[137] R. Ozawa, S. Hayami, and Y. Motome, "Zero-field skyrmions with a high topological number in itinerant magnets", Phys. Rev. Lett. **118**, 147205 (2017).

[138] K. Kadowaki, K. Okuda, and M. Date, "Magnetization and Magnetoresistance of MnSi. I", J. Phys. Soc. Jpn. **51**, 2433 (1982).

[139] S. Mühlbauer, B. Binz, F. Jonietz, C Pfleiderer, A Rosch, A Neubauer, R. Georgii, and P. Boni, "Skyrmion Lattice in a Chiral Magnet", Science **323**, 915 (2009).

[140] X. Z. Yu, Y. Onose, N. Kanazawa, J. H. Park, J. H. Han, Y. Matsui, N. Nagaosa, and Y. Tokura, "Real-space observation of a two-dimensional skyrmion crystal", Nature **465**, 901 (2010).

[141] X. Z. Yu, N. Kanazawa, Y. Onose, K. Kimoto, W. Z. Zhang, S. Ishiwata, Y. Matsui, and Y. Tokura, "Near room-temperature formation of a skyrmion crystal in thin-films of the helimagnet FeGe", Nat. Mater. **10**, 106 (2011).

[142] S. Seki, X. Z. Yu, S. Ishiwata, and Y. Tokura, "Observation of Skyrmions in a Multiferroic Material", Science **336**, 198 (2012).

[143] J. Rajeswari, P. Huang, G. F. Mancini, Y. Murooka, T. Latychevskaia, D. McGrouther, M. Cantoni, E. Baldini, J. S. White, A. Magrez, T. Giamarchi, H. M. Rønnow, and F. Carbone, "Filming the formation and fluctuation of skyrmion domains by cryo-Lorentz transmission electron microscopy", Proc. Natl. Acad. Sci. USA **112**, 14212 (2015).

[144] I. Kézsmárki, S. Bordács, P. Milde, E. Neuber, L. M. Eng, J. S. White, H. M. Rønnow, C. D. Dewhurst, M. Mochizuki, K. Yanai, H. Nakamura, D. Ehlers, V. Tsurkan, and A. Loidl, "Néel-type skyrmion lattice with confined orientation in the polar magnetic semiconductor $GaV_4S_8$", Nat. Mater. **14**, 1116 (2015).

[145] A. Tonomura, X. Z. Yu, K. Yanagisawa, T. Matsuda, Y. Onose, N. Kanazawa, H. S. Park, and Y. Tokura, "Real-Space Observation of Skyrmion Lattice in Helimagnet MnSi Thin Samples", Nano Lett. **12**, 1673 (2012).

[146] S. Buhrandt and L. Fritz, "Skyrmion lattice phase in three-dimensional chiral magnets from Monte Carlo simulations", Phys. Rev. B **88**, 195137 (2013).

[147] J. H. Han, J. Zang, Z. Yang, J.-H. Park, and N. Nagaosa, "Skyrmion lattice in a two-dimensional chiral magnet", Phys. Rev. B **82**, 094429 (2010).

[148] J. Iwasaki, M. Mochizuki, and N. Nagaosa, "Universal current-velocity relation of skyrmion motion in chiral magnets", Nat. Commun. **4**, 1463 (2013).

[149] L. Kong and J. Zang, "Dynamics of an Insulating Skyrmion under a Temperature Gradient", Phys. Rev. Lett. **111**, 067203 (2013).

[150] A. K. Nandy, N. S. Kiselev, and S. Blügel, "Interlayer Exchange Coupling: A General Scheme Turning Chiral Magnets into Magnetic Multilayers Carrying Atomic-Scale Skyrmions", Phys. Rev. Lett. **116**, 177202 (2016).
[151] N. D. Mermin and H. Wagner, "Absence of Ferromagnetism or Antiferromagnetism in One- or Two-Dimensional Isotropic Heisenberg Models", Phys. Rev. Lett. **17**, 1133 (1966).
[152] N. D. Mermin, "Crystalline Order in Two Dimensions", Phys. Rev. **176**, 250 (1968).
[153] S. C. Kapfer and W. Krauth, "Two-Dimensional Melting: From Liquid-Hexatic Coexistence to Continuous Transitions", Phys. Rev. Lett. **114**, 035702 (2015).
[154] B. J. Alder and T. E. Wainwright, "Phase Transition in Elastic Disks", Phys. Rev. **127**, 359 (1962).
[155] J. M. Kosterlitz and D. J. Thouless, "Long range order and metastability in two dimensional solids and superfluids. (application of dislocation theory)", J. Phys. C **5**, L124 (1972).
[156] J. M. Kosterlitz and D. J. Thouless, "Ordering, metastability and phase transitions in two-dimensional systems", J. Phys. C **6**, 1181 (1973).
[157] B. I. Halperin and D. R. Nelson, "Theory of Two-Dimensional Melting", Phys. Rev. Lett. **41**, 121 (1978).
[158] A. P. Young, "Melting and the vector Coulomb gas in two dimensions", Phys. Rev. B **19**, 1855 (1979).
[159] D. R. Nelson and B. I. Halperin, "Dislocation-mediated melting in two dimensions", Phys. Rev. B **19**, 2457 (1979).
[160] J. M. Kosterlitz, "Kosterlitz–Thouless physics: a review of key issues", Rep. Prog. Phys. **79**, 026001 (2016).
[161] A. L. Thorneywork, J. L. Abbott, D. G. Aarts, and R. P. Dullens, "Two-Dimensional Melting of Colloidal Hard Spheres", Phys. Rev. Lett. **118**, 158001 (2017).
[162] A. Bauer and C. Pfleiderer, *Topological Structures in Ferroic Materials*, edited by J. Seidel, Vol. 228, Springer Series in Materials Science (Springer International Publishing, Cham, 2016).
[163] J. Lee and K. J. Strandburg, "First-order melting transition of the hard-disk system", Phys. Rev. B **46**, 11190 (1992).
[164] C. H. Mak, "Large-scale simulations of the two-dimensional melting of hard disks", Phys. Rev. E **73**, 065104 (2006).
[165] S. D. Yi, S. Onoda, N. Nagaosa, and J. H. Han, "Skyrmions and anomalous Hall effect in a Dzyaloshinskii-Moriya spiral magnet", Phys. Rev. B **80**, 054416 (2009).
[166] B. Berg and M. Lüscher, "Definition and statistical distributions of a topological number in the lattice O(3) $\sigma$-model", Nucl. Phys. B **190**, 412 (1981).
[167] P. J. Steinhardt, D. R. Nelson, and M. Ronchetti, "Bond-orientational order in liquids and glasses", Phys. Rev. B **28**, 784 (1983).
[168] W. Mickel, S. C. Kapfer, G. E. Schröder-Turk, and K. Mecke, "Shortcomings of the bond orientational order parameters for the analysis of disordered particulate matter", J. Chem. Phys. **138**, 044501 (2013).
[169] N. Duff and D. J. Lacks, "Shear-induced crystallization in jammed systems", Phys. Rev. E **75**, 031501 (2007).
[170] A. S. Keys and S. C. Glotzer, "How do Quasicrystals Grow?", Phys. Rev. Lett. **99**, 235503 (2007).
[171] H. Watanabe, S. Yukawa, Y. Ozeki, and N. Ito, "Nonequilibrium relaxation analysis of two-dimensional melting", Phys. Rev. E **66**, 041110 (2002).
[172] H. Watanabe, S. Yukawa, Y. Ozeki, and N. Ito, "Critical exponents of isotropic-hexatic phase transition in the hard-disk system", Phys. Rev. E **69**, 045103 (2004).

[173] H. Weber, D. Marx, and K. Binder, "Melting transition in two dimensions: A finite-size scaling analysis of bond-orientational order in hard disks", Phys. Rev. B **51**, 14636 (1995).

[174] N. N. Negulyaev, V. S. Stepanyuk, L. Niebergall, P. Bruno, M. Pivetta, M. Ternes, F. Patthey, and W.-D. Schneider, "Melting of Two-Dimensional Adatom Superlattices Stabilized by Long-Range Electronic Interactions", Phys. Rev. Lett. **102**, 246102 (2009).

[175] Y. Nii, A. Kikkawa, Y. Taguchi, Y. Tokura, and Y. Iwasa, "Elastic Stiffness of a Skyrmion Crystal", Phys. Rev. Lett. **113**, 267203 (2014).

[176] H. C. Fernandes and M. Weigel, "Non-reversible Monte Carlo simulations of spin models", Comput. Phys. Commun. **182**, 1856 (2011).

[177] J. Bierkens, "Non-reversible Metropolis-Hastings", Stat. Comput. **26**, 1213 (2016).